LUND UNIVERSITY

Three Dimensional Multiphysics Modeling of Reversible Solid Oxide Electrochemical Cells for Degradation Studies

Navasa, Maria

2016

[Link to publication](#)

Total number of authors:
1

Three Dimensional Multiphysics Modeling of Reversible Solid Oxide Electrochemical Cells for Degradation Studies

LUND
UNIVERSITY

Maria Navasa

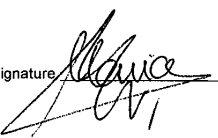| Organization LUND UNIVERSITY	Document name DOCTORAL DISSERTATION
Department of Energy Sciences Division of Heat Transfer	Date of issue 2016-11-25
Author(s) Maria Navasa	Sponsoring organization

Title and subtitle
Three Dimensional Multiphysics Modeling of Reversible Solid Oxide Electrochemical Cells for Degradation Studies

Abstract

Solid oxide electrochemical cells (SOCs) are considered a highly promising technology for providing efficient, sustainable and economic conversion between chemical energy and electrical energy. SOCs can be operated as fuel cells, where electric power is obtained from fossil or non-fossil hydrocarbon fuels depending on the origin or as electrolysis cells, whereby using electrical energy from renewable sources like wind or solar, chemical energy can be stored as fuels. However, despite its promising potential, SOCs are still not commercialized in large scales. A hard competition from well-established technologies in the electricity generation market, e.g., gas turbines, for the fuel cell operating mode, hinders its commercialization for large scale applications while electrolysis operation mode has found its way into niche markets. One of the big challenges for its success is to guarantee a long-term stability (4+ years), which is currently not attainable due to degradation issues.

Large gradients in temperature, gas composition and local overpotentials in a single cell or a stack cause degradation. Different variables lead to different degradation mechanisms. These gradients occur within the cell, making it difficult to monitor the degradation process. Physical models can be used for retrieving local quantities and thus assist in failure assessment and provide insights on how to mitigate them.

A three dimensional multiphysics model has been developed in this work to simulate the performance of SOCs under fuel cell and electrolysis mode. The main transport phenomena are included and coupled to the electrochemical reactions. This enables the calculation of the local partial gas pressures, potentials and temperature distributions through the electrodes and across the cells as function of the operating cell voltage.
The model has been validated successfully by comparison to cell test experiments with H_2/H_2O and CO/CO_2 as feedstocks at different temperatures, flows and gas compositions. The highest deviation found, with respect to the cell voltage, is 6 %.

Even though the model can operate under both fuel cell and electrolysis modes, the model has been mainly used in electrolysis mode in this work. Apart from studying the effect of the cell operating voltage on the temperature, partial pressure of steam, current density and the overpotential through the cell, the developed model has been used for analyzing one degradation phenomenon, i.e., carbon deposition in the electrolysis operating mode. A detailed analysis of this degradation phenomenon has been performed showing a good agreement between the experimental data and the modeling approach of the local crossing of the thermodynamic carbon deposition threshold. The effect of two different heat boundary conditions on carbon formation have been evaluated as well as the effect of three different structural parameters for the fuel electrode: porosity, electrode thickness and ionic conductivity with a view to seeking cell improvements that can widen the operating window where carbon deposition is avoided.

Key words
SOCs, SOECs, SOFCs, multiphysics, modeling, three dimensional, transport phenomena, electrochemical reactions, overpotentials, potentials, boundary conditions, validation, experimental data, degradation, carbon deposition, steam, hydrogen, carbon dioxide, carbon monoxide, carbon activity.

Classification system and/or index terms (if any)

Supplementary bibliographical information	Language English
ISSN and key title ISRN LUTMDN/TMHP-16/1126-SE	ISBN 978-91-7473-752-3 (Print) 978-91-7473-753-0 (Pdf)
Recipient's notes	Number of pages 205	Price
	Security classification	

I, the undersigned, being the copyright owner of the abstract of the above-mentioned dissertation, hereby grant to all reference sources permission to publish and disseminate the abstract of the above-mentioned dissertation

Signature _____ Date _____ 2016-11-25

Three Dimensional Multiphysics Modeling of Reversible Solid Oxide Electrochemical Cells for Degradation Studies

Maria Navasa

LUND
UNIVERSITY

Department of Energy Sciences
Faculty of Engineering

Thesis for the degree of Doctor of Philosophy in Engineering.

Cover: Photo by Theis Løye Skafte of a cell test rig at DTU Energy with multihpyshics simulation results, which has been artistically modified.

Division of Heat Transfer
Department of Energy Sciences
Faculty of Engineering
Lund University
Box 118
SE-221 00 LUND
SWEDEN

Abstract

Solid oxide electrochemical cells (SOCs) are considered a highly promising technology for providing efficient, sustainable and economic conversion between chemical energy and electrical energy. SOCs can be operated as fuel cells, where electric power is obtained from fossil or non-fossil hydrocarbon fuels depending on the origin or as electrolysis cells, whereby using electrical energy from renewable sources like wind or solar, chemical energy can be stored as fuels. However, despite its promising potential, SOCs are still not commercialized in large scales. A hard competition from well-established technologies in the electricity generation market, e.g., gas turbines, for the fuel cell operating mode, hinders its commercialization for large scale applications while electrolysis operation mode has found its way into niche markets. One of the big challenges for its success is to guarantee a long-term stability (4+ years), which is currently not attainable due to degradation issues.

Large gradients in temperature, gas composition and local overpotentials in a single cell or a stack cause degradation. Different variables lead to different degradation mechanisms. These gradients occur within the cell, making it difficult to monitor the degradation process. Physical models can be used for retrieving local quantities and thus assist in failure assessment and provide insights on how to mitigate them.

A three dimensional multiphysics model has been developed in this work to simulate the performance of SOCs under fuel cell and electrolysis mode. The main transport phenomena are included and coupled to the electrochemical reactions. This enables the calculation of the local partial gas pressures, potentials and temperature distributions through the electrodes and across the cells as function of the operating cell voltage.

The model has been validated successfully by comparison to cell test experiments with H_2/H_2O and CO/CO_2 as feedstocks at different temperatures, flows and gas compositions. The highest deviation found, with respect to the cell voltage, is 6 %.

Even though the model can operate under both fuel cell and electrolysis modes, the model has been mainly used in electrolysis mode in this work. Apart from studying the effect of the cell operating voltage on the temperature, partial pressure of steam, current density and the overpotential through the cell, the developed model has been used for analyzing one degradation phenomenon,

i.e., carbon deposition in the electrolysis operating mode. A detailed analysis of this degradation phenomenon has been performed showing a good agreement between the experimental data and the modeling approach of the local crossing of the thermodynamic carbon deposition threshold. The effect of two different heat boundary conditions on carbon formation have been evaluated as well as the effect of three different structural parameters for the fuel electrode: porosity, electrode thickness and ionic conductivity with a view to seeking cell improvements that can widen the operating window where carbon deposition is avoided.

Popular science summary

Solid oxide electrochemical cells are devices which can be used for two different purposes. The most common is as an electricity generating source, the so-called solid oxide fuel cell. Solid oxide fuel cells can convert the energy that fuels contain, known as chemical energy, into electricity via electrochemical reactions. Common fuels are carbon monoxide and hydrogen, but other carbon containing fuels such as methane can also be used although a previous reaction (reforming reaction) will be necessary to transform these into hydrogen or carbon monoxide. The most promising purpose of solid oxide electrochemical cells is as an energy storage device, known by the name of solid oxide electrolysis cell. Solid oxide electrolysis cells use electrical energy, e.g., surplus of renewable electricity, to drive electrochemical reactions to obtain fuels containing chemical energy like methane or diesel, which can be used in the existing fuel infrastructure. Electrolysis cells are commonly described as the reversible operation of fuel cells, where instead of using fuels to produce electricity, fuels are produced to store electricity. In a very simplified manner, electrolysis cells can be understood as batteries, where instead of storing electrical energy in metals as batteries do, they store electricity in fuels like hydrogen and carbon monoxide.

Depending on the source of the fuel, or electrical energy, solid oxide electrochemical cells can be considered as a promising technology for providing sustainable, efficient and economic conversion between electrical energy and chemical energy. Yet, to be considered a competitive technology, these devices should present a long-term stability, (4+) years, which is nowadays hindered by degradation phenomena.

In order to extend the lifetime of solid oxide electrochemical cells, reduction of these degradation phenomena is necessary. As these devices are relatively complicated, due to the high operating temperatures (800 °C) and explosive gases (H_2), while measuring the conditions inside is quite challenging and very expensive to perform regularly, modeling can be a strong tool to analyze the performance of such devices.

In this work, a three dimensional model of a solid oxide electrochemical cell has been developed to simulate the behavior of these devices. The model considers the main physical phenomena that take place in such devices and has been validated with experimental data under different operating conditions. Moreover, due to the detailed degree of the model, the local distribution of certain variables has enabled studying the behavior of the cells under different

operating conditions and finally, to elucidate degradation phenomena such as carbon deposition when operating in electrolysis mode.

Populärvetenskaplig sammanfattning

Elektrokemiska fastoxidceller kan användas för två olika syften. Den vanligaste är som en källa till elektricitet, de så kallade fastoxidbränslecellerna. Dessa bränsleceller omvandlar energin i bränsle, det som kallas för kemisk energi, till elektricitet genom en elektrokemisk reaktion. Bränslena som oftast används för att driva bränslecellerna är kolmonoxid och vätgas även om andra kolbaserade bränslen kan användas, men måste då först konverteras till kolmonoxid eller vätgas. För elektrokemiska fastoxidceller är dock det mest lovande användningsområdet som energilagringsenheter, oftast benämnda som fastoxidelektrolysceller. Fastoxidelektrolysceller använder sig av elektricitet, till exempel i form överskott vid förnybara källor, för att driva den elektrokemiska reaktionen och ladda bränslen som metan och diesel, vilka kan användas i dagens samhälle. Elektrolyscellerna är därför beskrivna som att utföra den omvända processen till den som sker i fastoxidbränsleceller, då de istället för att producera elektricitet från bränsle producerar bränsle för att lagra elektricitet. En liknelse kan göras till batterier vilka lagrar energi (elektricitet) i olika metaller, medan fastoxidelektrolysceller lagrar elektricitet i bränslen som kolmonoxid och vätgas.

Beroende på källan till bränslet, eller den elektriska energin, som driver de elektrokemiska fastoxidcellerna så kan de anses vara en lovande teknologi för en hållbar, effektiv och ekonomisk hållbar omvandling mellan elektricitet och kemisk energi. Dock så måste det tilläggas att för att det ska anses vara en konkurrenskraftig teknologi och inneha långsiktig hållbarhet (4+ år) så måste de degenererande mekanismerna so idag hindrar detta stoppas.

För att utöka livslängden hos fastoxidelektrolyscellerna så måste degraderingen minska. Komplexiteten hos dessa celler, i form av höga användningstemperaturer (800 °C) och explosiva gaser (vätgas), gör att det är både utmanande och dyrt att regelbundet mäta förhållanden inuti cellerna och modellering kan därför vara ett kraftfullt verktyg att analysera prestandan hos cellerna.

Detta arbete omfattar utvecklingen av en tredimensionell simuleringsmodell av en elektrokemisk fastoxidcell för att undersöka dess prestanda. Modellen tar fysikaliska fenomen med i beräkningen och har bekräftats av experimentell data tagen från celler under olika förhållanden. Utförligheten hos modellen har tillåtit en noggrann undersökning av vissa storheter, under ett visst spännigsintervall, men har också medfört att man kan visa hur kolavlagringar, vilket är en degraderingsmekanism, påverkat elektrolyscellerna.

Acknowledgments

First, I would like to thank my main supervisor, Prof. Bengt Sundén, for giving me the opportunity to perform my PhD studies and for his support these years.

Special and infinite thanks to Dr. Henrik Lund Frandsen and Dr. Christopher Graves for your endless patience, support, feedback, encouragement and valuable input. A word of thanks to Theis Løye Skafte, for giving sense to my simulations with all the experiments as well as your feedback; and Dr. Christodoulos Chatzichristodoulou, for bringing some coherence to our electrochemistry discussions.

I would like to express my gratitude to Dr. Anke Hagen for opening me the doors to DTU Risø as well as for your pep-talks. Likewise, Prof. Christoffer Norberg for trusting me for teaching undergraduate students Thermodynamics and Fluid Mechanics. Thank you very much Dr. Marcus Thern for all your help.

I would also like to thank all the colleagues and administrators from the Department of Energy Sciences as well as those from DTU Risø for all the nice moments shared. Special mention to the Swedish carpool, trips to Risø would definitely had not been the same without your company discussing from cars... to cars.

My time in Sweden has been filled with a bunch of unforgettable moments thanks to wonderful people that have been by my side, no matter the circumstances. Thanks so much to Emelie, Filip, Sofia and Annika for all our decompressing lunches full with laughter. Emelie, Tora and Solmaz, thank you for always being there. Tons of thanks to Gustaf, for making me believe in myself apart from your continuous support. To Tina and Oskar, for being my Swedish family.

Deserving of special attention are my parents, Miquel and Neus, and my brother, Albert, for their unconditional endless support, love and patience. For showing

me to never give up, no matter how hard it is nor how many times you fall. *Moltes gràcies per ser com sou*.

List of publications

The present thesis is based on the following papers, which will be referenced by roman numerals in the body text of the thesis. The papers are appended in the order listed below.

I **M. Navasa**, J. Yuan and B. Sundén, "Transport phenomena in solid oxide fuel cell electrodes focusing on heat transfer related to chemical reactions", *in 6th European Thermal Sciences Conference (Eurotherm 2012)* (I. Publishing, ed.), *Journal of Physics: Conference series*,vol. 395, p. 012086, 2012.

II **M. Navasa**, J. Yuan, and B. Sundén, "Computational fluid dynamics approach for performance evaluation of a solid oxide electrolysis cell for hydrogen production", *Applied Energy*, vol. 137, pp. 867–876, 2015.

III **M. Navasa**, C. Graves, C. Chatzichristodoulou, T. L. Skafte, B. Sundén and H. L. Frandsen, "A Three Dimensional Multiphysics Model of a Solid Oxide Electrochemical Cell for Degradation Studies", *to be submitted for journal publication*.

IV **M. Navasa**, H. L. Frandsen, T. L. Skafte, B. Sundén and C. Graves, "Localized Carbon Deposition in Solid Oxide Electrolysis Cells Studied by Multiphysics Modeling", *to be submitted for journal publication*.

Author contribution
For all papers, the thesis author was responsible for developing the computational model, performing simulations, validating the model against experimental data, analysis of the results and writing the papers.

List of publications not included in the thesis

Journal and conference papers

  V **M. Navasa**, J. Yuan and B. Sundén, "Effects of the Operating Voltage on a Solid Oxide Electrolysis Cell", *Proceedings of 11th European SOFC & SOE Forum*, Lucerne, Switzerland, July 1-4, 2014.

  VI M. Andersson, **M. Navasa**, J. Yuan and B. Sundén, "SOFC Modeling at the Cell Scale Including Hydrogen and Carbon Monoxide as Electrochemically Active Fuels", *Proceedings of ASME 10th International Fuel Cell Science Conference*, pp. 281-291, FuelCell2012-91112, San Diego, California, July 23-26, 2012.

  VII **M. Navasa**, J. Yuan and B. Sundén, "Review of Microstructure Modeling in Solid Oxide Fuel Cell Electrodes", Paper presented at the *International Conference on Applied Energy (ICAE 2012)*, Suzhou, China, July 5-8, 2012.

  VIII **M. Navasa**, M. Andersson, J. Yuan and B. Sundén, "The Effect of Heat Transfer in the Polarizations within an Intermediate Temperature Solid Oxide Fuel Cell", *12th International Conference on Advanced Computational Methods and Experimental Measurements in Heat Transfer and Mass Transfer,* Split, Croatia, June 27-29, 2012. Also in A*dvanced Computational Methods and Experiments in Heat Transfer XII*, pp. 3-14, WIT Press, UK, 2012.

Licentiate dissertation

  IX **M. Navasa**, *Computational Fluid Dynamics Analysis on Transport Phenomena in Solid Oxide Electrochemical Cells*, Lund: Department of Energy Sciences, Lund University, 2013.

Nomenclature

a_i	Chemical activity of species i, dimensionless
c	Molar density, $[\mathrm{mol\,m^{-3}}]$
c_p	Specific heat at constant pressure, $[\mathrm{J\,kg^{-1}\,K^{-1}}]$
D	Mass diffusion coefficient, $[\mathrm{m^2\,s^{-1}}]$
D_T	Thermal diffusion coefficient, $[\mathrm{kg\,m^{-1}\,s^{-1}}]$
d_p	Mean pore diameter, $[\mathrm{m}]$
E_a	Activation energy, $[\mathrm{kJ\,mol^{-1}}]$
F	Faraday constant, $[\mathrm{C\,mol^{-1}}]$
i	Current density, $[\mathrm{A\,m^{-2}}]$
i_0	Exchange current density, $[\mathrm{A\,m^{-2}}]$
$\mathbf{J}$	Current density flux, $[\mathrm{A\,m^{-2}}]$
j	Volumetric current density, $[\mathrm{A\,m^{-3}}]$
K_0	Permeability of the porous medium, $[\mathrm{m^2}]$
$K_{eq,B}$	Boudouard reaction equilibrium constant, $[\mathrm{atm^{-1}}]$
k	Thermal conductivity, $[\mathrm{W\,m^{-1}\,K^{-1}}]$
M_i	Molar mass of species i, $[\mathrm{kg\,mol^{-1}}]$
$\mathbf{N}$	Molar flux of gas species, $[\mathrm{mol\,m^{-2}\,s^{-1}}]$
n	Number of species i in the gas mixture, dimensionless
n_e	Number of electrons transferred per reaction, dimensionless
p	Total pressure, $[\mathrm{Pa}]$ or $[\mathrm{atm}]$
p_i	Partial pressure of species i, $[\mathrm{atm}]$
R	Ideal gas constant, $[\mathrm{J\,mol^{-1}\,K^{-1}}]$
$R_{\mathrm{act,rx.}}$	Activation polarization resistance, $[\Omega\,\mathrm{cm^2}]$
R_0	Pre-exponential factor of $R_{\mathrm{act,rx.}}$, $[\Omega\,\mathrm{cm^2}]$
S	Entropy, $[\mathrm{J\,mol^{-1}\,K^{-1}}]$
S_d	Source term for the momentum conservation equation, $[\mathrm{J\,m^{-3}\,s^{-1}}]$
S_m	Source term for the mass conservation equation, $[\mathrm{mol\,m^{-3}\,s^{-1}}]$
S_T	Source term for the energy conservation equation, $[\mathrm{J\,m^{-3}\,s^{-1}}]$
S_η	Source term for the charge transfer equation, $[\mathrm{A\,m^{-3}}]$
T	Temperature, $[\mathrm{K}]$
$\mathbf{U}$	Velocity vector, $[\mathrm{m\,s^{-1}}]$
V	Voltage, $[\mathrm{V}]$
v	Diffusion volume, $[\mathrm{m^3\,mol^{-1}}]$
Y_i	Molar fraction of species i, dimensionless
z_i	Charge number of species i, dimensionless

Greek letters

α	Reduction/oxidation transfer coefficient, dimensionless
α_C	Carbon activity, dimensionless
ε	Porosity of the electrodes, dimensionless
η	Electrochemical potential, $[\mathrm{J\,mol^{-1}}]$/ Overpotential, [V]
μ	Chemical potential, $[\mathrm{J\,mol^{-1}}]$/ Dynamic viscosity, $[\mathrm{Pa\,s^{-1}}]$
π	Electromotive or Fermi potential, [V]
ρ	Density, $[\mathrm{kg\,m^{-3}}]$
σ	Electric conductivity, $[\mathrm{S\,m^{-1}}]$
τ	Tortuosity, dimensionless
ϕ	Galvani potential, [V]
χ_i	Volume fraction of phase i in the electrode, dimensionless

Chemical species & compounds

C	Carbon
CO	Carbon monoxide
CO_2	Carbon dioxide
e^-	Electron
H_2	Hydrogen
H_2O	Water
Li	Lithium
Ni	Nickel
N_2	Nitrogen
O_2	Oxygen
O^{2-}	Oxide ion
Pb	Lead

Abbreviations

1D/2D/3D	One, two or three dimensional
3PB	Triple-phase boundary
BFM	Binary friction model
CGO	Gadolinium doped cerium oxide
CPIM	Cylindrical pore interpolation model

DGM	Dusty gas model
DTU	Technical University of Denmark
FEM	Finite element method
HTE	High-temperature electrolysis
IEA	International Energy Agency
LSC	Lanthanum strontium cobaltite
LSCF	Lanthanum strontium cobalt ferrite
LSM	Lanthanum strontium manganite
PEMFC	Proton exchange membrane fuel cell
SMM	Stefan-Maxwell model
SOC	Solid oxide electrochemical cell
SOEC	Solid oxide electrolysis cell
SOFC	Solid oxide fuel cell
STP	Standard temperature and pressure (0 °C and 1 atm)
YSZ	Yttria-stabilized zirconia

Contents

List of Figures

CHAPTER 1

Introduction

Renewable electricity generation became the second largest source of electricity world wide after coal in 2013, as reported by the International Energy Agency (IEA). It was the first time that renewable electricity overtook natural gas, by supplying 22 % of the total electricity production. Nevertheless, coal reached its highest level in the same year representing a 41.1 % of the global production of electricity [1].

Even though electricity based energy carriers are beginning to partially replace the liquid hydrocarbons commonly used in the transportation sector amongst others, considerable amounts of hydrocarbon based fuels will still be needed in the near future. Fossil fuels and biomass are the most common feedstocks for production of hydrocarbon fuels. However, by using renewable or nuclear energy, carbon dioxide and water can be recycled into sustainable hydrocarbon fuels via non-biological processes where oxygen is removed from carbon dioxide and water. Moreover, capturing carbon dioxide from the atmosphere would enable a closed-loop carbon-neutral fuel cycle. Solid oxide electrochemical cells are devices which can produce syngas (synthetic gas), a combination of carbon

monoxide and hydrogen, via electrolysis using electricity from renewable or nuclear energy and at the same time, if necessary, produce electricity when operating in reversed mode, as fuel cells.

Solid oxide electrochemical cells are very interesting devices and at the same time, extremely complicated due to the different and coupled physical phenomena that describe them. Despite still not being commercially available at large scales, considerable amount of research has been done on this technology, especially when operated as fuel cells. However, the electrolysis operation mode is gaining more and more attention as they cover a completely different and new market. To be able to mass produce solid oxide electrolysis cells, investigation should pinpoint to increasing the lifetime and stability of these devices.

Albeit most of the research on solid oxide electrochemical cells is experimentally based, the use of computational tools has opened a new door of possibilities. Apart from decreasing the experimental cost and time, numerical simulations allow the calculation of local quantities in the cells, which are currently impossible to obtain experimentally and can help understand the cell behavior under certain conditions. Nevertheless, one should bear in mind that experiments and simulations must go hand in hand for retrieving valuable information of the cell, which can be key for further development of the technology.

1.1.   Research objectives

The objectives of this work were to develop a three dimensional (3D) numerical model at macroscale to analyze the different physical phenomena occurring in a solid oxide electrochemical cell (SOC), with special emphasis on the electrolysis mode of operation, and to be able to model the effects of certain degradation phenomena that affect such devices. More precisely, the aims were:

- To develop a macroscale 3D multiphyics model for a single planar fuel electrode SOC, with focus on solid oxide electrolysis cells (SOEC), considering the main physical phenomena taking place, i.e., electrochemical reactions, transport of charged species, mass, momentum and heat transfer, with all the corresponding couplings between the different phenomena. The model should be able to operate with H_2/H_2O and CO/CO_2 as feedstocks.

- Validate the multiphysics model against reliable experimental data.

- To model one degradation phenomenon in SOEC, i.e., carbon deposition, and evaluate the effect of certain structural parameters on this phenomenon.

To this end, a 3D multiphysics model was developed and thoroughly validated with experimental data for both feedstocks. When the model operated with H_2/H_2O as reactant, the thermal modes of an SOEC as function of the operating cell voltage were evaluated as well as the overpotential distribution across the electrodes in detail. The model operating with CO/CO_2 was used to study the carbon deposition phenomenon. The effects of the porosity, thickness and ionic conductivity of the fuel electrode on this degradation phenomena were evaluated.

1.2. Methodology

In order to analyze the different degradation phenomena in an SOC, there is a need for numerical models which sufficiently describe the different coupled physical phenomena.

The multiphysics model was built with COMSOL Multiphysics 5.2, a finite element method (FEM) based commercial software using the Batteries and Fuel Cells module. The model was developed for a single planar fuel electrode SOEC in 3D. The modeled cell is comprised of fuel and air channels, a contact layer, an anode, an electrolyte and a cathode (with an active and a support layer). The electrochemical reactions, transport of charged species, mass, heat and momentum were calculated simultaneously. Variation of temperature, type of fuel, fuel flow rates and composition as well as structural parameters were performed in the work to analyze different phenomena and their effects on the cell performance.

The choice of cell modeled in the work, i.e., geometry, cell materials, operation conditions, etc., has been dictated by the experimental data available from the Department of Energy Conversion and Storage at the Technical University of Denmark, (DTU Energy, Risø Campus) in collaboration with Haldor Topsoe A/S. All cell tests have been done on solid oxide electrochemical cells produced

by Haldor Topsoe A/S and these tests were performed at DTU Energy by PhD student Theis Løye Skafte.

1.3.   Thesis outline

The thesis can be divided in two parts. The first part contains an extended summary of the different concepts dealt with in the appended papers. It is, in turn, structured as follows: after a brief introduction and the aim and objectives of the thesis in the current **Chapter 1**, **Chapter 2** provides an overview of solid oxide electrochemical cells, with differentiation between fuel cell and electrolysis operating modes, description of the characteristic electrochemical reactions and the most common materials used for these devices. **Chapter 3** describes all the physical phenomena taking place in an SOC, with focus on SOEC, together with an overview of the most common equations used in the literature accounting for the different phenomena described. In **Chapter 4**, the validation conditions, i.e., equations used, experimental setup configuration and conditions under which the simulations have been performed are briefly introduced as well as the main validation results. **Chapter 5** presents the major findings of the application of the model, which is also presented in the appended publications with the corresponding discussion. Nevertheless, the successfully developed model and its leading broad validation discussed in **Chapters 3 and 4** are, per se, also major results of the work. **Chapter 6** discusses the conclusions of the present work as a whole and suggested paths for further research are proposed in **Chapter 7**.

The second part, on the other hand, compiles the appended publications.

CHAPTER 2

Introduction to Solid Oxide Electrochemical Cells

Solid oxide electrochemical cells (SOCs) are considered a highly promising technology for providing efficient, sustainable and economic conversion between chemical energy and electrical energy. SOCs can be operated as fuel cells, known as solid oxide fuel cells (SOFCs), in order to obtain electric power from fossil and non-fossil hydrocarbon fuels (depending on the fuel origin). However, SOCs can also be operated in the reverse direction, as solid oxide electrolysis cells (SOECs), so that electrical energy is supplied into the cell to drive electrochemical reactions, obtaining chemical energy stored as fuels.

The interest in the development of this technology has increased considerably in the last ten years but most of the development has been focused on employing SOCs as fuel cells for power generation. Yet, high temperature electrolysis in solid oxide electrochemical cells is gaining more attention. A feature of SOCs as energy storage devices is the easiness of scaling up systems by assembling individual cells into stacks to meet the desired output power. Although conventional batteries are more popular as energy storage devices, they store the electrical energy in expensive metals (Li, Pb, etc.) whereas SOECs store the electricity in

relatively economic fuels [2]. Nonetheless, for SOECs to become commercially interesting, a long-term stability for a period of 4+ years must be guaranteed, which is currently not possible due to various degradation mechanisms.

Today's state-of-the-art cells have high electrochemical performance. An important goal is improving the long-term durability. To do so, a deep understanding of the different degradation phenomena is required to be able to minimize their effects and increase the lifetime of the cells, e.g., carbon formation which destroys the electrochemical active sites, too high overpotential for nickel (Ni)-based anodes which causes Ni oxidation, too high overpotential for oxygen-electrodes which is responsible for build up of oxygen partial pressure near the interface of the electrolyte and oxygen electrode, etc.

2.1. Solid oxide fuel cells

Global environmental concerns have increased the interest in alternative high-performing electrical power units such as the solid oxide fuel cells (SOFCs). As defined in **Paper I**, SOFCs are high-temperature electrochemical devices that convert chemical energy of fuels into electrical energy in an environmental friendly and efficient manner.

The invention of fuel cells is not as recent as one might think. In fact, the principle behind fuel cells dates from the 19th century [3]. Although the discovery of the fuel cell is usually attributed to Sir William Groove in 1839 by demonstrating the reversibility of water electrolysis [4], Sir Humphrey Davy reported the same discovery already in 1802 [5]. In 1962, scientists at Westinghouse Electric Corporation (nowadays Siemens AG) demonstrated, for the first time, the extraction of electricity from a device they named "solid electrolyte fuel cell" [6]. Since then, an intense research from companies and universities have contributed to the development and improvement of this technology.

Despite almost six decades have passed since their discovery, SOFCs are still nowadays not being commercialized in large scales. Many reasons can be given to the non-commercialization of SOFCs at such scales but the lack of sufficient knowledge of some phenomena that take place in an SOFC, may be the key to the slow development of this technology. Besides, the market in which SOFCs must compete contains well established technologies like gas turbines, which are already mass produced and can supply electricity at much larger scales. Yet,

SOECs, described in Section 2.2, can turn the table as they cover a completely different, and new market.

The working principle of an SOFC is sketched in Figure 2.1. The cell shown is a planar design but other designs are also available, e.g., a tubular design. Oxygen or air is supplied into the channel on the cathode side or positive electrode whereas the fuel (hydrogen, methane, methanol, etc.) is supplied into the fuel channel on the anode side or negative electrode to obtain electricity and steam as a product as shown in Eq. (2.1). Oxygen molecules diffuse through the cathodic diffusion layer, to the reactive surfaces of the cathode active layer. The reactive surfaces of the active layer are where the reduction of oxygen to oxide ions (O^{2-}) takes place, Eq. (2.2). The electrons required are supplied by the oxidation of the fuel in the anodic active layer. The fuel molecules diffuse through the porous anode supporting structure, also known as the anode diffusion layer, to the anodic triple-phase boundaries (3PBs), where they are oxidized to water when reacting with the oxide ions that have diffused through the electrolyte from the cathodic reactive surfaces, Eq. (2.3). The 3PBs are where the electrochemical reaction in the anode occurs and receives the name of triple-phase boundaries as it is the location where the pores, the ionic conducting and the electronic conducting phases meet.

$$H_{2(g)} + \frac{1}{2}O_{2(g)} \Longleftrightarrow H_2O_{(g)} \tag{2.1}$$

$$\frac{1}{2}O_{2(g)} + 2\,e^- \Longleftrightarrow O^{2-} \tag{2.2}$$

$$H_{2(g)} + O^{2-} \Longleftrightarrow H_2O_{(g)} + 2\,e^- \tag{2.3}$$
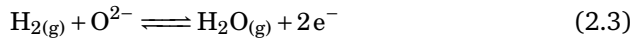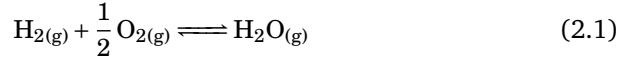
If another reactant rather than hydrogen is supplied, reformation of the fuel can take place in the porous region forming carbon monoxide and hydrogen. As with hydrogen, carbon monoxide can also be oxidized as follows:

$$CO_{(g)} + O^{2-} \Longleftrightarrow CO_{2(g)} + 2\,e^- \tag{2.4}$$
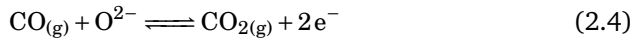
Different proposed reaction mechanisms try to describe the electrochemical phenomena taking place in the anode and in the cathode of the fuel cell without
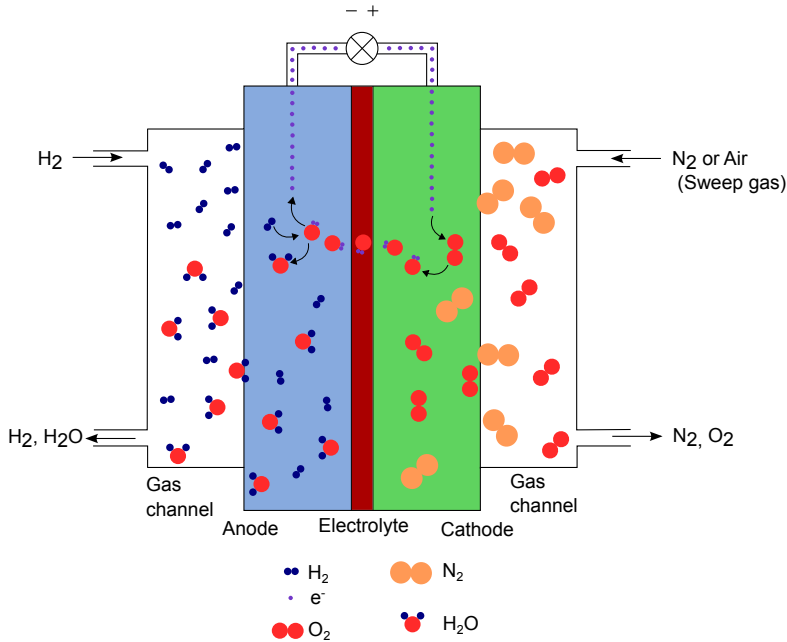
Figure 2.1: *Schematic drawing of the electrochemical reactions in an SOFC.*

a clear consensus on which is the most accurate one. Thus, different surface compounds are suggested under different assumptions stating that nothing is clear in this field when going into details of the reaction mechanisms [7–11]. However, the general reaction can always be used but if the performance of SOFCs must be improved, the understanding of the reaction mechanism for this reaction might be key to success. Yet, the electrochemical reactions are not the only chemical reactions that take place at the electrodes of the fuel cells. The other main group of reactions is the reforming reactions. Regarding reforming reactions, different kinetic expressions on Ni-YSZ electrodes have been reported in literature and are summarized in Table 1 in **Paper I**, claiming more attention due to the amount of ambiguities gathered around these kinetic expressions. Both of these types of reactions; the electrochemical and the reforming reactions, are known as surface reactions because both take place at the surface of the electrodes, electrochemical reactions at both electrodes and reforming reactions at the anode, and thus the active surface area or the 3PBs, depending on the electrode material, is very important.

One of the main characteristics of SOFCs is that they operate at high temperatures. The fact that these cells initially operated at temperatures around 1000 °C is due to the material of the electrolyte used, yttria-stabilized zirconia (YSZ) which presented a too high resistance at 800 °C for an electrolyte supported cell. YSZ is a ceramic material which becomes conductive to oxygen ions at certain temperatures while remaining non-conductive to electrons. Thus, electrochemical reactions can take place at the electrodes without the need of expensive catalysts [12–14]. In fact, the anode material, usually Ni-YSZ, is catalytic itself for both the internal reforming and electrochemical reactions that take place while strontium doped lanthanum manganite (LSM) is one of the common materials for the cathode at such temperatures. Nowadays, SOFCs operate at lower temperatures, e.g., 600-800 °C or even lower, that allow using other electrode materials rather than Ni-YSZ and LSM. Two of the most common materials used today for the cathode are the lanthanum strontium cobalt ferrite (LSCF) or the strontium doped lanthanum cobaltite (LSC), which present a mixed conductivity as ionic and electronic conducting phases coexist.

However, it is not just a matter of decreasing the operating temperature as other phenomena must be taken into account as well. The kinetics of the chemical reactions that take place in SOFCs are temperature dependent and this is also a matter of concern.

When comparing SOFCs to other current fuel cell types, for example, proton exchange membrane fuel cells (PEMFCs), SOFCs present a number of attractive features. SOFCs are fuel flexible, which means that different fuels apart from pure hydrogen can be used due to the tolerance of carbon monoxide, being a fuel as well. Then, short-chain hydrocarbon fuels like methane or ethanol among others can be supplied as fuel to SOFCs. Long-chain hydrocarbons can lead to carbon deposition on the Ni-based electrode damaging the cell if no upstream treatment is done. Moreover, all components are in solid state (there are no liquid electrolytes like for example in alkaline fuel cells), there is no electrolyte dehydration or cathode flooding, which are the most critical challenges for PEMFCs, and the high quality waste heat produced at a high temperature by SOFCs can be utilized effectively for either combined heat and power or for use in hybrid systems together with gas turbines.

2.2.   Solid oxide electrolysis cells

Hydrogen presents certain advantages as an energy carrier as it can be obtained from all primary energy resources such as fossil fuels, renewable energy sources and nuclear power as well as from synthesized hydrogen carriers like methanol, ammonia and synthetic fuels [15]. For example, devices such as fuel cells can convert hydrogen into electricity in an environmentally friendly and efficient way as previously mentioned. Due to the increasing interest of hydrogen as a fuel, industry and governmental institutions are putting more effort in developing hydrogen-related technologies [16]. Although nowadays the main hydrogen source is by hydrocarbon reforming, hydrogen can also be obtained through green energy procedures such as water splitting (electrolysis, photolysis or thermochemical water splitting), from biomass, etc. [17–21]. At present, water electrolysis is the most viable process for hydrogen production at large scales and consists of splitting water into hydrogen and oxygen by applying electrical energy [17]. The total energy required for electrolysis increases slightly with temperature while the required electrical energy decreases. Thus, high-temperature electrolysis might be a really interesting process to consider when waste heat from other processes is available [16, 17]. In fact, solid oxide electrolysis cells can use the waste heat from industry to decrease the heat demand from the endothermic electrochemical reactions and the electricity obtained from renewable sources, mainly solar cells or wind turbines. Moreover, there is growing interest in integrating electrolysis cells together with nuclear energy to improve the hydrogen production efficiency [22, 23].

High-temperature electrolysis (HTE) of water takes place at 700-1000 °C and the technology is based on the high-temperature cells, especially SOECs.

SOECs are usually understood as SOFCs operating in reversed mode due to the similarity. An SOEC consists of the same components as an SOFC: fuel and air channels, a cathode, an anode and an electrolyte. The components' materials are also usually the same: Ni-YSZ cermet for the steam/hydrogen electrode, YSZ for the electrolyte and LSM for the oxygen-side electrode. In the state-of-the-art solid oxide electrochemical cells, the LSM has been replaced by more active electrocatalysts such as LSC and LSCF with an interlayer of acceptor doped ceria, usually gadolinia doped ceria (CGO), to avoid reaction between the LSC or LSCF with the YSZ [24]. However, the transport characteristics in SOECs differ considerably from SOFCs, especially those related to kinetic models, potential ranges and gradients involved, influencing performance and long-term stability in different ways and thus, results from SOFCs cannot be

directly applied to SOECs. This further emphasizes the limited amount of research that has been done in this field and the need for more attention for development of the technology [24–26].

Typical SOC electrodes consist of three-phase composites (an ion conducting, an electron conducting and a gas phase for electrodes like Ni-YSZ) creating a porous microstructure in order to allow the transport of ions, electrons and gases at the same time within the electrodes. The electrochemical reactions take place at the percolated triple-phase boundaries (3PBs), where the ionic and the electronic pathways meet with the gas phase. Electrode performance is determined by several factors but two of the primary factors are the abundance of 3PBs and the transport properties. Also, the electrode microstructure is key for improving the electrochemical cell performance. Porous composite structures have been developed to increase the length of 3PBs in the electrodes. Due to the degree of complexity of the interactions between these and in order to be able to improve the cell performance, a deep understanding of the electrode microstructure is required in quantitative terms [27].

Steam (H_2O) is fed into the electrolysis cell where water splitting takes place giving hydrogen and oxygen as products, as shown in Eq. (2.5). Although hydrogen is the most important product obtained, oxygen should be considered as a co-product instead of a by-product as it is a valuable commodity which can be sold for other applications.

$$H_2O_{(g)} \rightleftharpoons H_{2(g)} + \frac{1}{2}O_{2(g)} \tag{2.5}$$
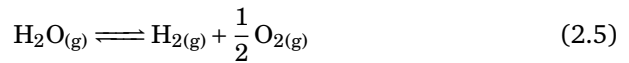
Steam is fed into the fuel channel on the cathode side as shown in Figure 2.2. The water molecules diffuse through the porous cathode structure to the cathodic 3PBs, where they react with the electrons supplied by an external source to produce hydrogen gas and oxide ions, Eq. (2.6). Apart from steam, another feedstock for SOECs is carbon dioxide (CO_2), which is reduced to carbon monoxide (CO), Eq. (2.7). Electrolysis of both feedstocks simultaneously, H_2O and CO_2, is also possible and is known as co-electrolysis.

$$H_2O_{(g)} + 2e^- \rightleftharpoons H_{2(g)} + O^{2-} \tag{2.6}$$

$$CO_{2(g)} + 2e^- \rightleftharpoons CO_{(g)} + O^{2-} \tag{2.7}$$

11
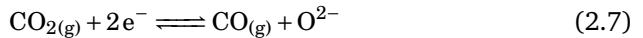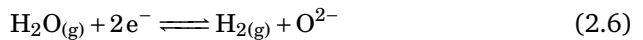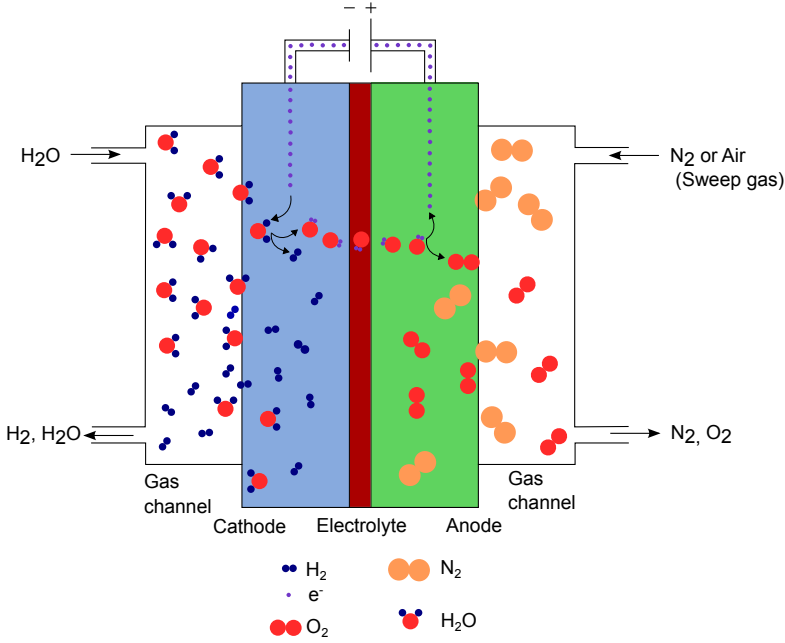
Figure 2.2: *Schematic drawing of the electrochemical reactions in an SOEC.*

The oxide ions are transported through the electrolyte to the reactive surfaces of the mixed ionic-electronic conducting ferrite/cobaltite anode, where the oxide ions are oxidized to oxygen gas, as shown in Eq. (2.8). Moreover, the electrolyte prevents the electrons crossing over from the oxygen electrode to the fuel electrode. The oxygen gas molecules produced diffuse back through the porous anode to the air channel. Note here the difference between the two devices, although the reactions are the same, they take place in opposite directions.

$$O^{2-} \Longleftrightarrow \frac{1}{2} O_{2(g)} + 2 e^- \tag{2.8}$$

CHAPTER 3

Modeling of Solid Oxide Electrochemical Cells

Current research in SOCs is oriented towards solving a certain number of problems like, for example, those material related arising from the high operating temperatures, mechanical and thermal stability of the cells and stacks. Also the issues regarding the different types of available fuels for SOFCs or those associated with the electrochemical reactions: possible reaction mechanisms, different surface species depending on the reaction mechanism, etc. Different possibilities exist to analyze these problems amongst which experimental measurements and numerical modeling are the strongest ones. However, due to the small dimensions of the cells and the high operating temperatures, the experiments become very demanding and expensive as a result of the materials and instruments required. Therefore, numerical modeling is needed for analyzing the current problems. Different levels of modeling have been performed by researchers depending on the scientific targets and objectives.

Several modeling approaches exist depending on the purpose of the research, each with its advantages and disadvantages. The ability to choose an adequate method relies on the clear understanding of the processes to model in terms

of physical phenomena, the different parameters involved as well as the dimensions and the computational capability. In general, the computational capability is still increasing, which leads to more possibilities for more detailed modeling at smaller scales and more complex problems [28]. The modeling of fuel cells and electrolysis cells involves complex geometrical structures on many length scales, which are important for macrostructural changes of, e.g., flow, temperature and stress on the macro-scale of an SOC stack as well as for implementing the electrochemical reactions at micro- and nano-scale. This can in turn, also be used to elucidate the reaction kinetics, which only limited information exists on. Yet, numerical approaches require experimental data in order to validate the simulated models. Obtaining experimental data under realistic conditions for these devices is not as straightforward as one can imagine, especially at micro- and nano-scale.

SOCs are known to be complex devices as different physical phenomena take place at the same time and these are highly coupled. The attraction for computational modeling of physical phenomena, known as multiphysics modeling, in these devices has increased in the last years. Multiphysics models consider the interaction and coupling between several physical phenomena.

The evolution of SOCs multiphysics models at cell level in the last twenty years can be summarized in Table 3.1. A selection of significant reported multiphysics models in literature, the model described in this work referred to as current work and what can be considered the ideal model with the corresponding numerical models describing the main physical phenomena occurring in SOCs are outlined. Achenbach *et al.* [29] reported one of the first three-dimensional (3D) models in literature of SOFCs, which was a transient model, in 1994. In the beginning of the 20th century, Chan *et al.* [30] went a step further by considering the Butler-Volmer equation for the reaction kinetics. Some years later, Ni [16] solved the fluid flow in detail while Laurencin *et al.* [31], further introduced the Dusty gas model for a more accurate resistance due to gas diffusion in the electrodes and considered radiation for a cell stack. Chatzichristodoulou [24] solved the ionic and electronic transport within the electrolyte layers for a detailed potential distribution as a starting point for discussing degradation mechanisms. In the current model, linear Chang-Jaffe kinetics have been introduced for description of the reaction kinetics and a detailed distribution of the overpotentials across the cells allows studying degradation phenomena in the device. The ideal model is also included in Table 3.1. The ideal model would be the one that combines the best models for describing the different physical phenomena, which are those stated in Table 3.1 and described later in the chapter.

Table 3.1: *Evolution of multiphysics models.*

	Flow model	Heat model	Gas diffusion	Reaction kinetics	Charge transfer in the electrolyte
[29] (1994)	PF	CC	ND	ND	ND
[30] (2001)	PF	UT	F-B	BV	ND
[16] (2009)	ME	CC	F-B	ND	ND
[31] (2011)	PF	CCR	DGM	BV	ND
[24] (2016)	PF	UT	DGM	ND	e^-/O^{2-}
Current model	ME	CC	SMM-B	CJ	O^{2-}
Ideal model	ME	CCR	DGM	CJ	e^-/O^{2-}

[a] PF: plug flow
[b] ME: momentum equation
[c] CC: conduction and convection
[d] UT: uniform temperature
[e] CCR: conduction, convection and radiation
[f] ND: not discretized
[g] F-B: Fick's law and Bosanquet equation
[h] DGM: Dusty gas model
[i] SMM-B: Stefan-Maxwell model and Bosanquet equation
[j] BV: Butler-Volmer
[k] CJ: Chang-Jaffe
[l] e^-: electronic transport
[m] O^{2-}: ionic transport

Another prominent modeling approach is multiscale modeling, which consists of connecting a specific process at different time- and length scales. Different length scales define the multiscale model: macro-, micro-, meso- and nano-although the divisions between the different scales is not stated clearly in the literature. A rough division of numerical models considering multiphysics and multiscale concepts consists of continuum models (finite element/volume methods) [32–35], discrete models (Lattice Boltzmann and Monte Carlo methods) [27, 36–40] and molecular dynamics based models [41–43].

In this section, the main physical phenomena occurring in SOCs, i.e., electrochemical reactions, transport of charged species, momentum transfer, mass transfer and heat transfer are defined. Moreover, a discussion of the available partial differential equations that describe these phenomena from a continuum model point of view is presented. Although the physical phenomena are the same for all SOCs, focus of the discussion is mainly on SOECs, as it is the main scope of the thesis. Furthermore, modeling of carbon formation, a degradation phenomenon, is also outlined.

3.1.   Electrochemical reactions

The electrochemical reactions that govern the electrolysis of steam and carbon dioxide, i.e., reduction and oxidation, are presented in Chapter 2.

One key issue in the physical modeling of SOCs is to determine the amount of current generated by the cell. The most common way of doing this today is to use the Butler-Volmer equation, in which the current density relates to the activation overpotential at each electrode/electrolyte interface. The Butler-Volmer equation is given by Eq. (3.1) [44, 45]:

$$i = i_0 \left[\exp\left(\alpha_a \frac{n_e F}{RT} \eta_{\text{act}} \right) - \exp\left(-\alpha_c \frac{n_e F}{RT} \eta_{\text{act}} \right) \right] \tag{3.1}$$

where R is the ideal gas constant, n_e is the number of electrons participating in the electrochemical reaction, F the Faraday constant, T the temperature, i_o is the exchange current density which depends strongly on the cell materials, construction and temperature and i is the current density, both in $\left[\text{Am}^{-2}\right]$. The charge transfer coefficients for each electrochemical half-reaction governed by the electron transfer process at the 3PB are α_a and α_c. The activation overpotential is η_{act}.

There is, however, no experimental support that this hypothesis is valid although most researchers, both experimental and modelers, assume that this equation describes the reaction kinetics in a satisfactory way [31, 32, 46–52]. When large activation losses are considered, a linear form of the Butler-Volmer equation can be used, see Tafel equation [53, 54]. Mogensen *et al.* have pointed out that the Butler-Volmer equation does not accurately describe the reaction kinetics when considering all the overpotentials. Some of the critique pointed out by Mogensen *et al.* is, quoting [55];

- *Composite electrodes do not follow a Butler-Volmer type expression.*

- *There is no experimental evidence that charge transfer, as described by the Butler-Volmer equation, is a rate limiting SOC electrode reaction.*

- *There will not be any single simple potential barrier to charge transfer. Charge transfer is limited by surface diffusion and transport through the surface layers.*

- *Electron transfer does not occur at a well-defined interface near the 3PB with a single activation barrier. It takes place through a non-homogeneous chemical and microstructural layer, which varies with temperature, time, gas compositions, etc. and several varying activation barriers.*

- *Complicated structures with several particle types involved will probably have a multi-step reaction mechanism with more than one process contributing to the polarization resistance.*

A possible reason for the widely assumed use of the Butler-Volmer equation in SOCs is because it has been well experimentally observed for ambient temperature aqueous systems like PEMFC electrodes. However, it does not necessarily translate to electrochemistry at 700 °C, where the actual charge-transfer process does not need to be rate-limiting compared with adsorption, diffusion and other processes.

For all the reasons stated, linear Chang-Jaffe kinetics, Eq. (3.2) [56], can be used as an alternative equally valid assumption.

$$i = \frac{\eta}{R_{\text{act,rx.}}} \tag{3.2}$$

where η is the overpotential and $R_{\text{act,rx.}}$ is the activation polarization resistance for the corresponding electrochemical reaction.

Thermodynamics of electrochemical cells

The chemical potential is an important part of thermodynamics and mass transfer for systems without electrical forces. This approach is valid also for electrochemical reactions but some modifications to the theory are needed because of the electrical charges. It can be shown that the electrochemical reactions can be taken into account by considering the electrical contribution [57]. The equilibrium condition for an electrochemical reaction can now be written as:

$$\sum_{i=1}^{r} \mu_i + z_i F \phi = \sum_{i=1}^{p} \mu_i + z_i F \phi \tag{3.3}$$

where z_i is the charge number of the component in the reaction, r stands for reactants and p for products. The chemical potential of species i is represented by μ_i and ϕ is the Galvani potential. The electrochemical potential is a composite potential which takes into account the chemical as well as the electrical forces. It is thus beneficial to introduce the definition of the electrochemical potential, η, as [57]:

$$\eta_i \equiv \mu_i + z_i F \phi \tag{3.4}$$

Note here that now η is the electrochemical potential and not the overpotential defined in Eq. (3.2). Using Eq. (3.3) and Eq. (3.4), the equilibrium condition for the electrochemical reaction, Eq. (2.8), can be written as:

$$\eta_{O^{2-}} = \frac{1}{2}\eta_{O_{2(g)}} + 2\eta_{e^-} \tag{3.5}$$

where Eq. (3.5), $\eta_{O^{2-}}$, $\eta_{O_{2(g)}}$ and η_{e^-} are the electrochemical potential of the oxide ions, oxygen gas and electrons, respectively.

By making use of Eq. (3.4), it is possible to express the terms in Eq. (3.5) for the different species as:

$$\eta_{O^{2-}} = \mu_{O^{2-}} - 2F\phi \tag{3.6}$$

$$\eta_{O_{2(g)}} = \mu_{O_{2(g)}} \tag{3.7}$$

$$\eta_{e^-} = \mu_{e^-} - F\phi \tag{3.8}$$

where $\mu_{O^{2-}}$, $\mu_{O_{2(g)}}$ and μ_{e^-} are the chemical potentials of the oxide ions, oxygen gas and electrons, respectively, F is the Faraday constant and ϕ is the Galvani potential. The Galvani potential can be understood as the electric potential in the interior of the solid [58]. Note that for the oxygen gas, Eq. (3.7), the electrochemical potential is equivalent to the chemical potential as there is no charge contribution. Moreover, for an ideal gas, i.e. O_2, the chemical potential

can be expressed as function of the chemical potential at a reference state plus a factor considering the activity of the gas i in the mixture [57].

It is also useful to define the electromotive potential, π, as [58]:

$$\pi \equiv \frac{-\eta_{e^-}}{F} \tag{3.9}$$

The electromotive potential, also known as Fermi potential, is therefore defined in terms of the electrochemical potential of the electron. This means that the electromotive potential can be considered as a measure of the electric potentials of the cell terminals.

By inserting and combining Eqs. (3.6), (3.8) and (3.9) in Eq. (3.5) at equilibrium, one obtains:

$$\left(\pi^{eq} - \phi^{eq}\right)_{air} = \frac{1}{4F}\left(\mu_{O_2}^* + RT\ln a_{O_2}\right) - \frac{\mu_{O^{2-}}}{2F} \tag{3.10}$$

where $\mu_{O_2}^*$ is the chemical potential of $O_{2(g)}$ at a reference state and a_i is the activity of the component i in the correspondent gas mixture. The chemical potential of oxide ions, $\mu_{O^{2-}}$, is assumed to be constant as consequence of considering that the electrolyte has constant oxygen stoichiometry.

It is possible to obtain similar expressions for the electrochemical reaction taking place at the fuel electrode, Eq. (2.6). Applying the same procedure, one obtains:

$$\left(\pi^{eq} - \phi^{eq}\right)_{fuel} = \frac{1}{2F}\left(\mu_{H_2O}^* - \mu_{H_2}^* + RT\ln\left(\frac{a_{H_2O}}{a_{H_2}}\right)\right) - \frac{\mu_{O^{2-}}}{2F} \tag{3.11}$$

Eq. (3.12) shows that the open circuit voltage of the cell (OCV) is the difference in the electromotive potentials of the electrodes at equilibrium. It is also known as equilibrium potential difference, and it is the minimum cell voltage required to decompose water (assuming negligible current leak at OCV).

$$V_{\text{cell}}^{\text{eq}} = \pi_{\text{air}}^{\text{eq}} - \pi_{\text{fuel}}^{\text{eq}} = \frac{\frac{1}{2}\mu_{O_2}^* + \mu_{H_2}^* - \mu_{H_2O}^*}{2F} + \frac{RT}{2F}\ln\left(\frac{a_{H_2}a_{O_2}^{\frac{1}{2}}}{a_{H_2O}}\right) \qquad (3.12)$$

where a_i is the activity of the component i in the correspondent gas mixture.

Now that the electromotive and the Galvani potentials have been introduced, the relationship between these, at a state i and at equilibrium, and the overpotential, η, defined in Eq. (3.2) is defined as:

$$\eta = \left(\pi^i - \phi^i\right) - \left(\pi^{\text{eq}} - \phi^{\text{eq}}\right) \qquad (3.13)$$

where η is the overpotential, π is the electromotive potential ϕ the Galvani potential.

For a better understanding of the potentials (Fermi and Galvani potentials) and the overpotential distribution in an SOC, these are exemplified in Figures 3.1 and 3.2, which are also present in **Paper III**. The distribution of these potentials and overpotential in fuel cell mode through the oxygen electrode, electrolyte and fuel electrode (active layer) are shown in Figure 3.1. The electromotive or Fermi potential at a state i, π, the electromotive potential at equilibrium, π^{eq}, the Galvani potential, ϕ, as well as the overpotential, η shown in Figure 3.1 follow Eq. (3.13) when $\phi^{\text{eq}} = 0$. Moreover, the cell voltage, V_{cell}, as well as the equilibrium cell voltage, V^{eq}, are also indicated.

The equivalent Figure 3.1 but for electrolysis mode under the same conditions specified above, i.e., $\phi^{\text{eq}} = 0$ is Figure 3.2. In electrolysis mode, and opposite to the fuel cell mode, the operating cell voltage is larger than the equilibrium cell voltage (open circuit voltage) due to the overpotential contribution.

Moreover, how the resistances of the electrodes and the electrolyte affect the Galvani potential in both cell modes as well as the overpotential distribution across the electrodes can be seen in both Figure 3.1 and Figure 3.2.
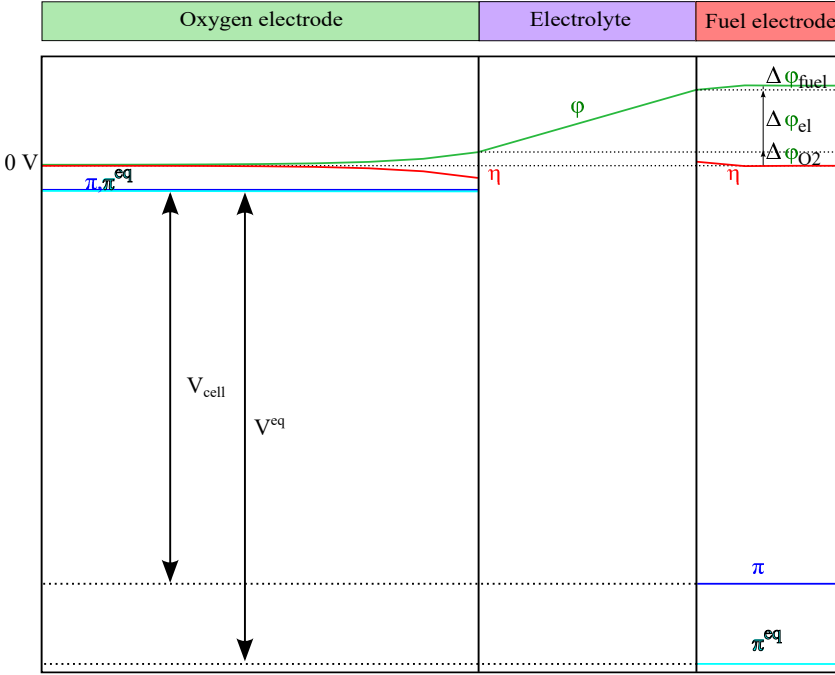
Figure 3.1: *Potentials and overpotential distribution across the oxygen electrode, electrolyte and fuel electrode thicknesses for fuel cell mode*

3.2. Carbon deposition

Carbon deposition is a degradation mechanism that can damage SOECs at certain operating conditions when CO_2 is used as feedstock. This phenomenon can lead to a complete destruction of the cell [59].

Degradation at the interface between the YSZ electrolyte and the Ni-YSZ electrode has been reported due to the formation of small amounts of carbon when performing co-electrolysis of CO_2 and H_2O at high current densities, which provides the highest syngas production rate. Raman spectroscopy was used by Duboviks *et al.* [59, 60] to show that the most common known carbon formation is when supplying hydrocarbons in fuel cell mode, which occurs at the electrode region close to the fuel channel, by methane cracking, Boudouard deposition or other thermochemical reactions depending on the fuel gas com-
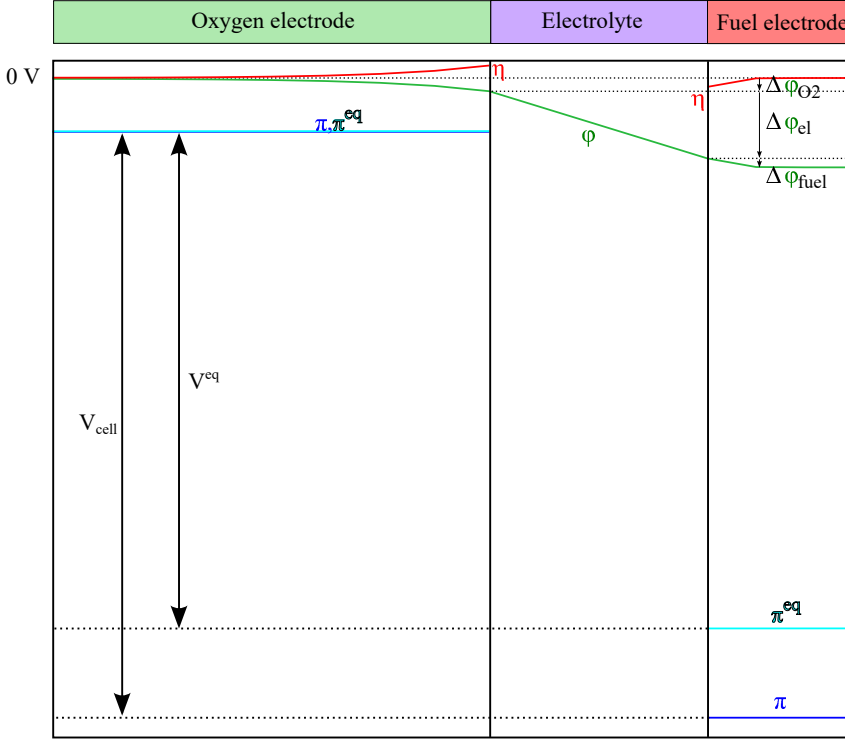
Figure 3.2: *Potentials and overpotential distribution across the oxygen electrode, electrolyte and fuel electrode thicknesses for electrolysis mode.*

position whereas in electrolysis mode, carbon formation takes place at the mentioned electrode/electrolyte interface, where CO is produced. The amount of active sites in the Ni-YSZ electrode can be reduced by formation of carbon in these locations. The worst carbon deposition scenario leads to a delamination of the electrode/electrolyte interface. Carbon formation can occur by the two-step reaction of electrolysis of CO_2 to CO, Eq. (3.14), followed by the Boudouard reaction, Eq. (3.15). Carbon deposition could also occur by electrolysis of carbon dioxide to solid carbon, Eq. (3.16), which is thermodynamically equivalent to the two-step reaction of electrolysis of CO_2 to CO followed by the Boudouard reaction. Another equivalent possibility to the two-step process described is the electrolysis of CO_2 to CO followed by the electrolysis of CO to C, Eq. (3.17).

$$2\,CO_{2(g)} + 4\,e^- \Longleftrightarrow 2\,CO_{(g)} + 2\,O^{2-} \tag{3.14}$$

$$2\,CO_{(g)} \longrightarrow C_{(s)} + CO_{2(g)} \tag{3.15}$$

$$CO_{2(g)} + 4\,e^- \Longleftrightarrow C_{(s)} + 2\,O^{2-} \tag{3.16}$$

$$CO_{(g)} + e^- \Longleftrightarrow C_{(s)} + O^{2-} \tag{3.17}$$
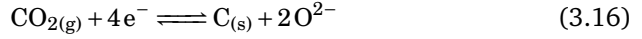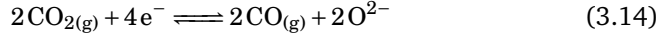
Carbon deposition has been observed at reactant conversion conditions considered not to be thermodynamically favored for carbon to deposit, i.e., higher reactant conversion than common values for SOEC operation. Therefore, understanding why the thermodynamic threshold is locally crossed and where this happens in the cell would be of great interest for determining the operating conditions and to avoid possible degradation of the cell [61].

Carbon deposition can be evaluated by calculating the thermodynamic carbon deposition threshold, $p_{CO,B}$. Carbon will form at the electrolyte/fuel electrode interface if the partial pressure of CO (p_{CO}) in the cell is larger than the carbon deposition threshold. This threshold, Eq. (3.20), can be derived from the Boudouard reaction equilibrium constant, Eq. (3.18), and Dalton's law of partial pressures, Eq. (3.19), at $p_{total} = 1$ atm:

$$K_{eq,B} = \frac{p_{CO_2}}{p_{CO}^2} \tag{3.18}$$

$$p_{total} = p_{CO_2} + p_{CO} \tag{3.19}$$

$$p_{CO,B} = \frac{1}{2K_{eq,B}} \left(-1 + \sqrt{1 + 4K_{eq,B}} \right) \tag{3.20}$$

where $K_{eq,B}$ is the equilibrium constant for the Boudouard reaction and p_i is the partial pressure of species i in the fuel gas mixture.

Carbon formation can also be evaluated by calculating the carbon activity, α_C, in the cell, Eq. (3.21). The carbon activity is similar to the thermodynamic threshold. For α_C values larger than 1, thermodynamics will favor carbon deposition while below 1, no carbon will be formed.

$$\alpha_C = K_{eq,B}\,\frac{p_{CO}^2}{p_{CO_2}} \tag{3.21}$$

3.3. Transport of charged species

The current conservation equation and Ohm's law, Eq. (3.22), describe the transport of ions and electrons in an SOC [28, 48, 62, 63].

$$\nabla \cdot \mathbf{J} = -\nabla \cdot \left(\frac{\sigma}{n_e F} \nabla \eta_{O^{2-}/e^-} \right) = S_\eta \tag{3.22}$$

where $\mathbf{J}$ is the current density flux, σ is the ionic or electronic conductivity, n_e is the number of electrons transferred per molecule of hydrogen or carbon monoxide produced, F the Faraday constant, η_{O^{2-}/e^-} the ionic or electronic electrochemical potential and S_η is the related source term.

Equation (3.22) can be expressed in terms of the Galvani potential, ϕ, when the ionic electrochemical potential is considered, see Eq. (3.6). It can also be written as function of the Fermi potential, π, for the electrochemical potential of the electron, see Eq. (3.9).

$$\nabla \cdot \mathbf{J} = \nabla \cdot (\sigma \nabla \phi) = S_\eta \tag{3.23}$$

$$\nabla \cdot \mathbf{J} = \nabla \cdot (\sigma \nabla \pi) = S_\eta \tag{3.24}$$

The related source term, S_η, is defined as follows:

$$S_\eta = \begin{cases} 0 & \text{in electrochemical inactive layers} & (3.25) \\ j & \text{in electrochemical active layers} & (3.26) \end{cases}$$

where j is the volumetric current density $[\text{Am}^{-3}]$. The electrochemical active areas are the regions where the electrochemical reactions occur, i.e., the fuel and oxygen electrodes, while the inactive layers refer to the porous support layers.

An effective ionic or electronic conductivity is calculated for porous media as [30, 64–66]:

$$\sigma_{\text{eff}} = \sum_{i=1}^{N} \sigma_i \frac{\chi_i}{\tau_{\text{i}}^2} \qquad (3.27)$$

where χ_i is the volume fraction of the electron or ion conducting material i in the electrode and τ_{i} the tortuosity of the corresponding material.

Few models in literature consider the current conservation equation explicitly. From those reported [24, 67–69], only [24] solves the electronic transport within the electrolyte layers for a bi-layer electrolyte SOEC, as a base for further study of degradation mechanisms. Other models in literature do not consider the current conservation or is not specifically discretized [16, 29–31, 70–73].

3.4. Momentum transfer

In a solid oxide electrochemical cell, momentum transfer of the gas takes place in the gas channels and in the porous electrodes. Momentum transfer is described by the momentum conservation equation [74]:

$$\nabla \cdot (\rho \mathbf{U} \mathbf{U}) = -\nabla p + \nabla \cdot (\mu \nabla \mathbf{U}) + S_d \qquad (3.28)$$

where $\mathbf{U}$ is the velocity vector, p the pressure, μ the dynamic viscosity of the gas mixture, ρ the density and S_d is the momentum source term, which is described as follows according to the different cell regions.

$$S_d = \begin{cases} 0 & \text{in gas channels} & (3.29) \\ -\dfrac{\mu}{K_0}\mathbf{U} & \text{in porous layers} & (3.30) \end{cases}$$

where K_0 is the permeability of the corresponding porous layer.

The momentum conservation equation started being used in SOCs when computational fluid dynamics (CFD) tools became available [16, 67–70, 72, 73]. Nevertheless, there are other numerical models which use plug flow when a detailed flow distribution in the cell is not focus of interest [24, 29–31, 71].

3.5. Mass transfer

Mass conservation is an important part in engineering analysis. The mass conservation, or as it is also known, the continuity equation, Eq. (3.31), ensures that mass is conserved throughout the system. For an electrochemical system, like SOCs, a source term accounting for the electrochemical reaction is added to the equation.

$$\nabla \cdot (c\mathbf{U}) = S_m \qquad (3.31)$$

where c is the molar density and S_m is the mass source term due to the electrochemical reactions. The molar density can be calculated via the ideal gas law for a system like SOCs. The mass source stems from the reacting species, and is thus linked to electrochemical reactions and the exchange current density as:

$$S_m = \begin{cases} 0 & \text{in non-electrochemical active layers} & (3.32) \\ \displaystyle\sum_i^n \dfrac{j}{n_e F} & \text{in electrochemical active layers} & (3.33) \end{cases}$$

where n_e is the number of electrons transferred per molecule of hydrogen or carbon monoxide produced and j is the volumetric current density. For a system where oxide ions (O^{2-}) are transported through the electrolyte, $n_e = 2$ [34].

The mass transfer equation Eq. (3.31) considers the bulk flow within the cell. However, the different species within the cell will also move relative to each other because of different gradients. An SOC is a multicomponent system that contains a mixture with n species. Thus, a balance equation for $(n-1)$ components is also required, Eq. (3.34), apart from the continuity equation, Eq. (3.31).

$$\nabla \cdot (c\mathbf{U}Y_i) = -\nabla \cdot \mathbf{N}_i + S_{m,i} \tag{3.34}$$

where $\mathbf{N}_i$ is the molar diffusion flux of species i, Y_i is the molar fraction of species i in the gas mixture and $S_{m,i}$ is the source term due to the electrochemical reaction for species i (Eq. 3.33).

The electrochemical reactions at the solid surfaces of the 3PBs influence gas diffusion. Mass diffusion is complex, especially within a porous region like an active electrode [75]. Apart from molecular diffusion, which dominates at large pore sizes and high pressure systems in the electrodes, Knudsen diffusion is also present. Knudsen diffusion becomes significant when the mean-free path of the species is larger than the pore size [76]. To take into account both type of diffusions, i.e., molecular and Knudsen, an effective diffusion coefficient can be calculated. The effective diffusion coefficient is a variable related to the molar diffusion flux, $\mathbf{N}_i$, which can be described by Fick's law. Fick's law is stated as:

$$\mathbf{N}_i = -cD_{ij}^{B,\text{eff}}\nabla Y_i - D_{Ti}\frac{\nabla T}{T} \tag{3.35}$$

where $D_{ij}^{B,\text{eff}}$ is the effective binary diffusion coefficient of gas species i and j and $D_{T,i}$ is the thermal diffusion coefficient of component i in the gas mixture.

Fick's law is only valid for a binary mixture, for a multicomponent mixture with invariable composition, for dilute mixtures or when the mass diffusion coefficient is independent of composition [77, 78]. Due to its simplicity, Fick's law has been often used in computational models due to its ease of implementation [16, 25, 46].

The Stefan-Maxwell (SMM) equations provide a more accurate description of the molar flux for an SOEC system [76]. As discussed by Bird *et al.* [77], the SMM can be seen as an extension of Fick's law for a multicomponent mixture. By the assumption that for ideal gases the Maxwell diffusion coefficients can be

approximated by the binary diffusion coefficients, the Stefan-Maxwell equations can be written as [76, 79]:

$$\sum_{j=1,j\neq i}^{n} \frac{Y_j \mathbf{N}_i - Y_i \mathbf{N}_j}{D_{ij}^{B,\text{eff}}} = -\frac{p}{RT}\nabla Y_i - \frac{Y_i}{RT}\nabla p \tag{3.36}$$

where p is the total pressure.

As Webb *et al.* [78] pointed out, Fick's law and the SMM describe gas diffusion in open spaces using effective diffusion parameters to account for the porous medium, but the basic transport equations are not altered. Thus, the Dusty gas model (DGM) appears to be a more suitable model for porous electrodes as it is seen as a breakthrough considering both the SMM formulation and Knudsen diffusion, Eq. (3.37) [78].

$$\sum_{j=1,j\neq i}^{n} \frac{Y_j \mathbf{N}_i - Y_i \mathbf{N}_j}{D_{ij}^{B,\text{eff}}} + \frac{\mathbf{N}_i}{D_i^{K,\text{eff}}} = -\frac{p}{RT}\nabla Y_i - \frac{Y_i}{RT}\left(1 + \frac{K_0 p}{\mu D_i^{K,\text{eff}}}\right)\nabla p \tag{3.37}$$

where $D_i^{K,\text{eff}}$ is the effective Knudsen diffusion coefficient of species i.

Tu understand gas transport mechanisms and their limitations, as well as for a proper evaluation of the transport phenomena at a continuum level, an accurate evaluation of the effective diffusion coefficients is needed. Geometric parameters of the porous electrodes, for example, porosity, tortuosity, particle size distribution, etc., are valuable input for calculation of these effective transport properties [80]. The effective diffusion coefficient, as well as for other transport properties, is usually calculated via Eq. (3.38).

$$D_{ij}^{B,\text{eff}} = \frac{\chi_i}{\tau^2} D_{ij}^B \tag{3.38}$$

where χ_i is the volume fraction of the void, electron or ion conduction material in the electrode, τ the tortuosity and D_{ij}^B the binary diffusion coefficient. Yet, the number of available tortuosity/porosity correlations in literature is significant [80], emphasizing the focus of attention in microstructure modeling, where specific values for a determined electrode can be obtained.

The binary diffusion coefficient, D_{ij}^B, can be evaluated by the kinetic theory of gases applying the Chapman-Enskog theory [81].

$$D_{ij}^B = D_{ji}^B = \frac{3.198 \cdot 10^{-8} T^{1.75}}{p \left(v_i^{1/3} + v_j^{1/3}\right)^2} \left(\frac{1}{M_i} + \frac{1}{M_j}\right)^{1/2} \qquad (3.39)$$

where p is the pressure, M_i and M_j are the molar masses of the gas component i and j, respectively, and v_i and v_j the diffusion volumes of component i and j, respectively.

The Knudsen diffusion coefficient, D_i^K, is defined as [82]:

$$D_i^K = \frac{d_p}{3} \sqrt{\frac{8RT}{\pi M_i}} \qquad (3.40)$$

where d_p is the mean pore diameter.

Other gas transport models have been reported in literature for modeling solid oxide electrochemical cells, mainly SOFCs, like the binary friction model (BFM) [83–85] and the cylindrical pore interpolation model (CPIM) [85, 86]. Despite the different available methods, Fick's model and the SMM are, by far, the most frequently used when modeling solid oxide electrochemical cells [51, 69, 87–90].

Due to the computational cost and simplicity, several authors in literature use the Bosanquet formula, Eq. (3.41), to account for both molecular and Knudsen diffusion in Fick's model or in SMM instead of the DGM [46, 47, 88, 89]. The main limitation of the Bosanquet formula, as Bertei and Nicolella [91] point out, is that it is only valid under the following conditions [92]: binary mixture, isobaric conditions and no net change in the number of moles. These are conditions which are hardly fulfilled in an SOC.

$$\frac{1}{D_{ij}^{\text{eff}}} = \frac{1}{D_{ij}^{B,\text{eff}}} + \frac{1}{D_i^{K,\text{eff}}} \qquad (3.41)$$

3.6. Heat transfer

Heat transfer in solid oxide electrochemical cells occurs by conduction, convection and radiation. Conduction takes place in the electrolyte, electrodes and interconnects. Convection through the entire cell occurs due to motion of the gases. Radiation within the electrolyte-electrode structure and surface to surface radiation in the fuel and air channels is also present. Moreover, depending on the operating temperature and cell voltage, heat generation or consumption exists.

As conduction is more significant than radiation inside the cell, radiative heat transfer can be neglected as demonstrated by a previous study [93]. Several models in literature can be found where radiation is neglected [16, 47, 67–69, 71–73, 94]. However, radiation has been found to be significant when determining the cell stack temperature distribution according to Hartvigsen *et al.* [95]. Thus, radiation effects can be considered for future studies of cell stacks.

The energy conservation equation is given by Eq. (3.42) to ensure that energy is conserved throughout the whole computational domain.

$$\nabla \cdot \left(\rho c_p \mathbf{U} T \right) = \nabla \cdot (k \nabla T) + S_T \tag{3.42}$$

where c_p is the specific heat at constant pressure and k is the thermal conductivity of the medium. S_T is the thermal source term, which takes into account the heat from the electrochemical reactions, the polarizations and joule heating and is defined as follows [46, 96]:

$$S_T = \begin{cases} 0 & \text{in gas channels} & (3.43) \\ \dfrac{i^2}{\sigma} & \text{in electrochemical inactive areas} & (3.44) \\ \dfrac{i^2}{\sigma} + j\left(\eta + \dfrac{T \Delta S}{2F} \right) & \text{in electrochemical active areas} & (3.45) \end{cases}$$

where i is the current density, j the volumetric current density, σ the electric conductivity of the material, ΔS the entropy change for the reaction and η is the overpotential.

To point out the importance of heat transfer in solid oxide electrochemical cells, the relative contributions of the different available heat sources for the fuel cell operating mode are reported in Table 2 in **Paper I**. Results show that the electrochemical reactions are the major contributors to the total heat in SOFCs followed by the reforming reaction.

Nevertheless, due to the scope of research, some models in literature assume a uniform temperature across the cell [24, 30, 70].

Validation

Developing a multiphysics model, no matter the scale, it is a challenge itself. A multiphysics model must however be validated against experimental data, increasing the degree of difficulty but at the same time, reliability. The accessibility to trustworthy experimental data might turn into a challenge as well. However, having a strong reliable multiphysics model can be a valuable tool for understanding certain phenomena occurring in the cell which cannot be observed experimentally, improving the cell performance as well as reducing the experimental cost amongst other advantages.

The conditions under which the model has been validated are presented in this chapter. Yet, one must bear in mind that nothing is set in stone due to the constant development in all fields, e.g., materials, modeling functions, computational capabilities, etc.

4.1. Experimental conditions

A cell consisting of a Ni-YSZ support, a Ni-YSZ active layer, a YSZ electrolyte and a LSCF-based oxygen electrode plus a contact layer has been considered in the multiphysics model and is shown in Figure 4.1. The Ni-YSZ support is the porous cathode while the Ni-YSZ active layer is the fuel electrode in Figure 4.1. A CGO barrier layer is present between the electrolyte and the LSCF-based electrode. The thicknesses of the different components are stated in Table 1 in **Paper III**.
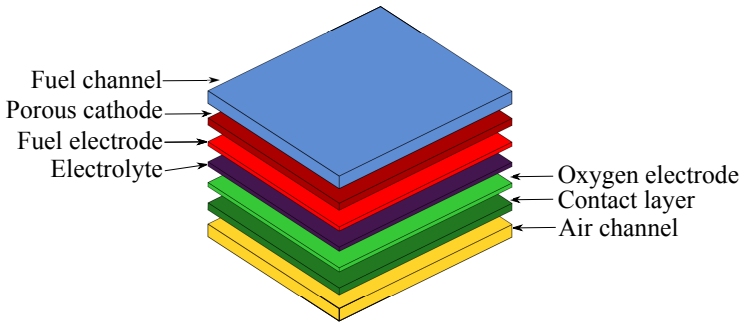
Figure 4.1: *Schematic drawing of the Haldor Topsoe A/S cell with its components.*

The test specimen consists of a 53 mm x 53 mm single cell with an active area of 40 mm x 40 mm, mounted into a test rig. The contacting of the cell is realized with corrugated nickel and gold meshes for the fuel and oxygen electrodes respectively, which provide a uniform contacting and gas distribution. The flow configuration in the cell test rig is shown in Figure 4.2.

All tests have been performed on planar fuel electrode supported solid oxide electrochemical cells produced by Haldor Topsoe A/S while the current-voltage (*i*-V) measurements were performed at DTU Energy. A number of *i*-V tests for the electrolysis of two feedstocks, i.e., H_2/H_2O and CO/CO_2, were measured at different inlet conditions. These conditions (temperature, flow rate and composition) are specified in Table 2 in **Paper III** for H_2/H_2O and in Table 1 in **Paper IV** for CO/CO_2.
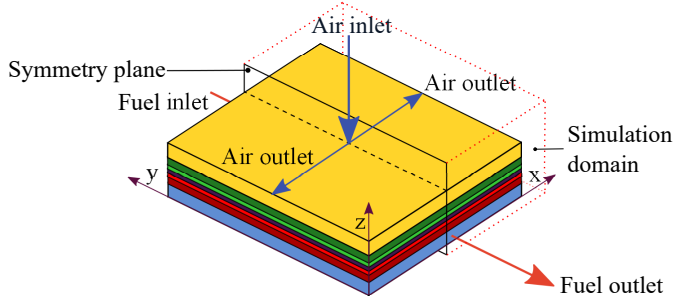
Figure 4.2: *Experimental setup arrangement with flow configuration and indication of the simulation domain.*

4.2. Simulation conditions

A three-dimensional (3D) multiphysics model of a planar SOC has been developed and validated with experimental data with H_2/H_2O in **Paper III** and CO/CO_2 in **Paper IV** as feedstocks at different temperatures, flows and gas compositions. The model considers the main transport phenomena taking place in such devices and are defined in Chapter 3. For the electrochemical reactions, due to all the reasons stated regarding the use of the Butler-Volmer equation, linear Chang-Jaffe kinetics [56], Eq. (3.2), are used in **Paper III** and **IV** to calculate the current density at the electrodes. At the fuel side, Eq. (4.1) or Eq. (4.2), are used according to the fuel selected while at the air side, Eq. (4.3) is proposed [97, 98]. The denominator of Eqs. (4.1) to (4.3) accounts for the activation polarization resistance, $R_{\text{act,rx.}}$, and it is partly Arrhenius temperature dependent and partly reactant/product activity dependent.

$$i_{\text{fuel,H}_2\text{O}} = \frac{\eta}{R_{0,\text{red,H}_2\text{O}} \exp\left(\frac{E_{a,\text{red,H}_2\text{O}}}{RT}\right) a_{\text{H}_2}^{0.1} a_{\text{H}_2\text{O}}^{-0.33}} \tag{4.1}$$

$$i_{\text{fuel,CO}_2} = \frac{\eta}{R_{0,\text{red,CO}_2} \exp\left(\frac{E_{a,\text{red,CO}_2}}{RT}\right) a_{\text{CO}}^{0.058} a_{\text{CO}_2}^{-0.25}} \tag{4.2}$$

$$i_{\text{air}} = \frac{\eta}{R_{0,\text{ox}} \exp\left(\frac{E_{a,\text{ox}}}{RT}\right) a_{\text{O}_2}^{-0.25}} \tag{4.3}$$

35

where η is the overpotential, a_i is the activity of the component i in the correspondent gas mixture, $E_{a,\mathrm{red}}$ is the activation energy of the activation polarization resistance, $R_{\mathrm{act,red}}$, for the reduction reaction, Eq. (2.6), $E_{a,\mathrm{ox}}$ is the activation energy of the activation polarization resistance, $R_{\mathrm{act,ox}}$, for the oxidation reaction, Eq. (2.8), and R_0 is the pre-exponential factor.

To model carbon deposition in **Paper IV**, the thermodynamic carbon deposition threshold, Eq. (3.20), has been locally calculated as well as the carbon activity, Eq. (3.21).

Transport of charged species is modeled by the current conservation equation and Ohm's law, Eq. (3.22), and momentum transfer via the momentum conservation equation, Eq. (3.28). Regarding mass transfer, the continuity equation is considered as well as the species conservation equation. Mass diffusion is modeled via the SMM and the effective diffusion coefficient is calculated via the Bosanquet formula, Eq. (3.41), to account for both molecular and Knudsen diffusion despite its limitations in both **Paper III** and **IV**.

Regarding heat transfer, radiation has been neglected to avoid a high complexity degree but heat sources due to joule heating, electrochemical reactions and polarizations are taken into account. The governing equation representing this transport phenomenon implemented in the multiphysics model is the energy conservation equation, Eq. (3.42), as defined in Chapter 3.

All the assumptions considered to model the setup in Figure 4.2, the specified boundary conditions, the parameters used as well as the calculation of gas properties are defined in **Paper III** and **IV**.

4.3. Validation against i-V curves

As mentioned above, a wide range of i-V curves were measured to validate the model for two different feedstocks at different temperatures, reactant flows and compositions. A single fitting parameter is required to fit the computational model to the experimental data, which is the pre-exponential factor of the activation polarization resistance for the fuel electrode, $R_{0,\mathrm{red,fuel}}$ contributing to the current density, defined via the linear Chang-Jaffe kinetics [56], Eqs. (4.1) and (4.2). $R_{0,\mathrm{red,fuel}}$ values are defined in **Paper III** for H_2O and in **Paper IV** for CO_2. The remaining material parameters have been taken from literature.

The comparison of *i*-V curves at different temperatures for a 24 Lh^{-1} at standard temperature and pressure (STP) H_2/H_2O at 50 % H_2 under electrolysis and fuel cell mode is shown in Figure 4.3, and for a 24 Lh^{-1} at STP CO/CO_2 at 50 % CO under electrolysis mode in Figure 4.4. Results for H_2/H_2O as feedstock show a maximum deviation with respect to the cell voltage of 1.3 % while for CO/CO_2, a maximum deviation of 1.2 % between the experimental and the simulated data for all the temperatures considered is reported.
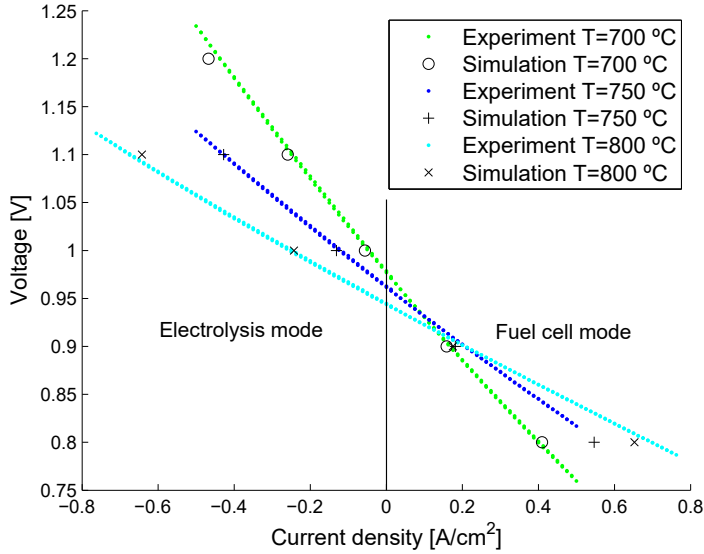
Figure 4.3: *i-V curves comparison at different gas inlet temperatures for H_2/H_2O as feedstock. Negative and positive current densities correspond to electrolysis mode and fuel cell mode operation, respectively.*

Comparisons of *i*-V curves for a 24 Lh^{-1} at STP H_2/H_2O at 96 % H_2 under fuel cell mode at three different temperatures are given in Figure 7 in **Paper III**, showing also a very small deviation between experimental and simulated data. The *i*-V curves shown correspond to fuel cell operation mode and the maximum deviation reported with respect to the cell voltage is 6 %.

The good results obtained from validation against *i*-V curves under different conditions, indicate that the multiphysics model has been developed with success and can be further used for the understanding of the physical processes
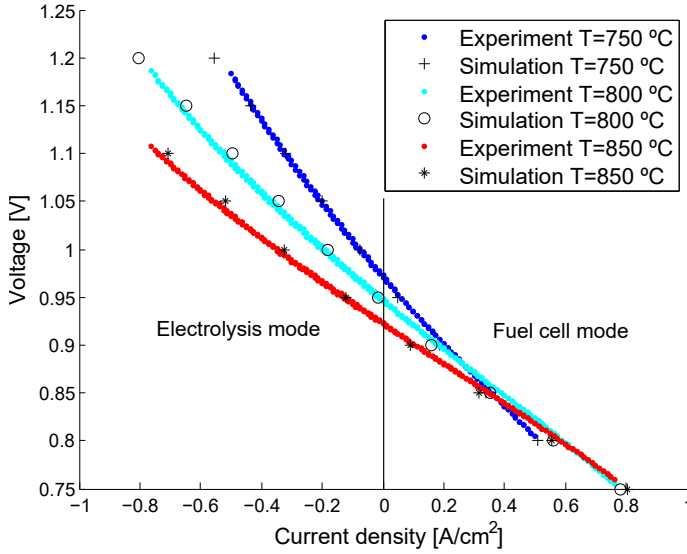
Figure 4.4: *i-V curves comparison at different gas inlet temperatures for CO/CO₂ as feedstock. Negative and positive current densities correspond to electrolysis mode and fuel cell mode operation, respectively.*

taking place as well as for degradation phenomena. Moreover, linear Chang-Jaffe kinetics are valid for describing the full *i*-V curves.

4.4. Validation against carbon deposition

For validating the multiphysics model ability to predict carbon deposition, the model results are compared with experiments at 750 °C with different gas composition. In the experiments, the current density is gradually increased until carbon formation is observed [61, 99]. The current density and the highest CO partial pressure, p_{CO}, achieved throughout the cell are shown in Figure 4.5. The location where carbon formation is first detected both experimentally and via simulations in the cell under different flow rates and compositions are at the cell outlet, close to the electrolyte/fuel electrode interface. These inlet conditions are specified in Table 2 in **Paper IV** as well as a brief description of the experimental and simulation procedure for detecting carbon formation.
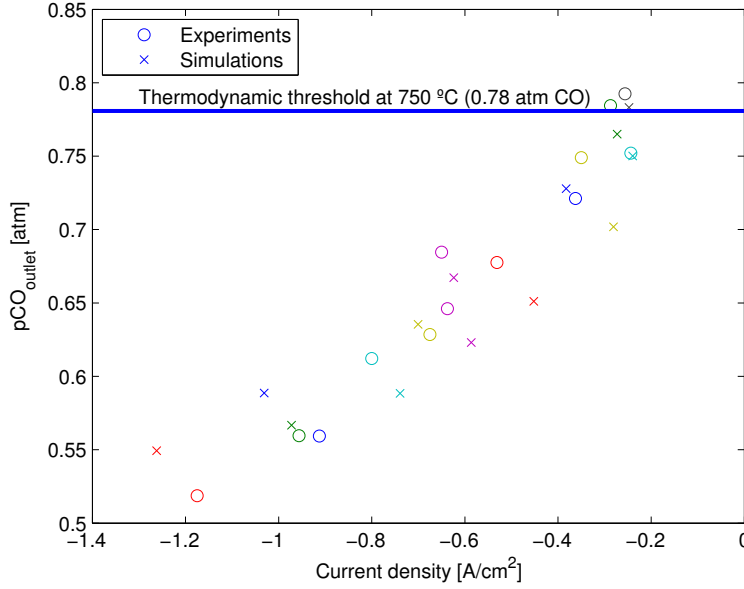
Figure 4.5: *Current density and p_{CO} at the cell outlet comparison when carbon formation is first detected in the cell for different fuel flow rates and compositions at 750 °C. The colors indicate different experiments with different inlet conditions.*

Simulation results seem to provide an acceptable agreement with the experimental values obtained presenting similar trends. Deviations between experimental and simulated data can be due to, among other factors, the magnitude of the step used for increasing the cell voltage or current in the experiments. Moreover, almost all the points from the experiments in Figure 4.5 are below the thermodynamic threshold at 750 °C, marked by the blue horizontal line, indicating that carbon deposition takes place at lower p_{CO} values than the theoretical p_{CO} threshold. This indicates that there is a local crossing of the thermodynamic carbon deposition threshold.

Main Results & Discussion

In this chapter, a brief description regarding **Paper II** is given and a summary of the main results from **Paper III** and **IV** is presented.

5.1. Paper II

In **Paper II**, a three dimensional SOC model of a cell operating in electrolysis mode was developed using the commercial software ANSYS Fluent, which is based on the finite volume method, for H_2/H_2O as feedstock operating in cross-flow configuration. Despite the simplicity of the model and the non-commercial dimensions of the cell, the model was suitable for studying the behavior of the current density, the temperature distribution and the hydrogen production in an SOEC under different operating cell voltages and flow configurations. A sketch of the computational domain used is shown in Figure 5.1, while all the dimensions and details are specified in **Paper II**.

Figure 5.1: *Computational domain for an initial study of an SOEC (not to scale).*

The simulations were conducted with four different operating cell voltages in order to study the effect on the different parameters. The simulations results showed that increased operating voltages leads to higher current densities. Increased operating cell voltages also led to an increased partial pressure of hydrogen. It should be noted that the increase in hydrogen production might lead to large temperature gradients. The different thermal modes of electrolysis cells and how the operating cell voltages affects these modes were also studied, that is, endothermic, thermo-neutral and exothermic modes.

Moreover, the effect of considering a co-flow configuration on the temperature distribution, current density and production of hydrogen were also investigated indicating that co-flow configuration leads to higher temperature gradients, lower current densities and consequently, lower production of hydrogen.

5.2. Paper III

In **Paper III**, apart from the extensive validation of the SOEC model when using H_2/H_2O as feedstock, the effect of the operating cell voltage on the steam partial pressure, overpotential and the temperature were investigated.

Detailed potential distribution

One of the major features of the multiphysics model presented is the ability to evaluate the potential and overpotential distribution through the cell. This is a valuable feature, which can be used for evaluation of degradation phenomena in the cell.

A base case was defined in **Paper III** for studying the temperature, current density, partial pressure of steam and potentials distribution through the cell, see Figure 8 in **Paper III**. The base case operating conditions are $24 \, \text{Lh}^{-1}$ at standard conditions (STP) for a 50 % H_2/50% H_2O feedstock at 750 °C and an operating cell voltage of 1.1 V.

Figure 5.2 shows the potential change through the active electrode layers and the electrolyte, see **Paper III**. The cell voltage is given by the difference in the Fermi potentials, which are stated as boundary conditions for the simulations. The Fermi potential for the air electrtode is $\pi_{\text{air}} = 0$ V and for the fuel electrode, $\pi_{\text{fuel}} = -1.1$ V, see Figure 5.2. The calculated cell voltage at equilibrium is defined by Eq. (3.12), and is approximately 1 V, see Figure 5.2. The Galvani potential, ϕ, is shown to decrease from the air electrode to the fuel electrode which is a result of different ohmic resistances from the different cell components. In the regions where the electrochemical reactions take place, i.e., electrode active layers close to the electrolyte interface, the overpotentials present higher values.

Effect of the operating cell voltage

The partial pressure of H_2O, the overpotential distribution as well as the temperature were chosen to study the effect of the operating cell voltage. Four different cell voltages were selected when operating the cell at 750 °C and $p_{H_2O} = 0.5$ atm as inlet conditions. 0.9 V represents the fuel cell operation mode while the remaining three correspond to the electrolysis operation mode. Different thermal behaviors in electrolysis operation mode are dictated by the operating cell voltage. To capture the endothermic behavior, 1.1 V is selected, which is below the thermo-neutral voltage. 1.3 V represents a voltage very close to the thermo-neutral voltage of steam electrolysis at 750 °C (1.285 V) while the exothermic behavior is captured by 1.5 V, a voltage above the thermo-neutral voltage. This provides current densities of 0.18, -0.43, -1.08 and -1.54 Acm^{-2}, respectively, as seen in Figure 4.3.
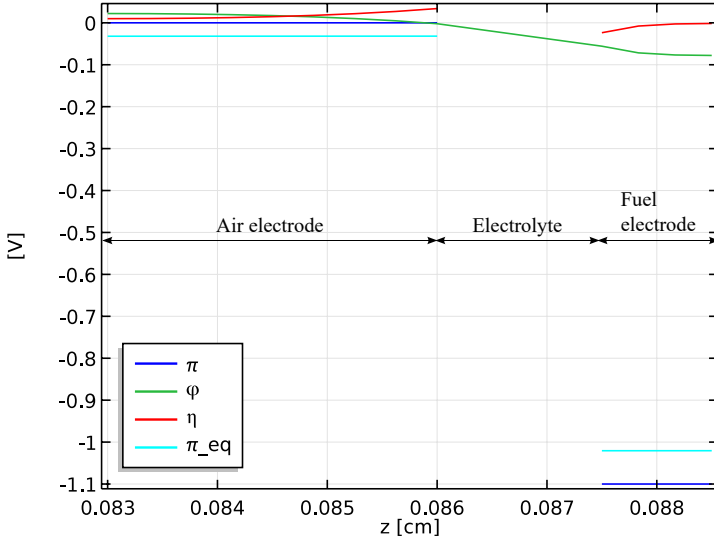
Figure 5.2: *Potential and overpotential distribution for the base case: 24* Lh^{-1}
STP for a 50 % H_2/50% H_2O *feedstock at 750 °C and an operating
cell voltage of 1.1 V.*

The H_2O partial pressure distribution along the fuel flow direction, where the
variation of p_{H_2O} is more significant, is shown in Figure 5.3a for the four cell
voltages. At the fuel inlet, $y = 4$ cm, the inlet partial pressure is set to $p_{H_2O} = 0.5$
atm. The fuel outlet is located at $y = 0$ cm. The partial pressure of H_2O increases
in fuel cell mode (0.9 V) as seen in Figure 5.3a due to the production of steam.
As this voltage is very close to the equilibrium cell voltage, cell voltage where
the current density is zero and thus, limited electrochemical reaction takes
place, the fuel utilization is very low. In electrolysis mode, lower H_2O partial
pressures are achieved at the fuel outlet with increasing cell voltage. The higher
the operating cell voltage, the higher the current density and consequently, the
fuel utilization. Fuel starvation can be observed at 1.5 V as steam is totally
consumed before the cell outlet is reached. An 86 % fuel utilization is attained
at 1.5 V in comparison to 60 % at 1.3 V and 24 % at 1.1 V.

Particularly noteworthy for this model is the capability to evaluate the over-
potential distribution through the air electrode, electrolyte and fuel electrode
at the four different cell specified voltages at the fuel and air outlets, see Fig-
ure 5.3b. Higher cell voltages result in higher overpotentials as seen in Fig-

ure 5.3b. Furthermore, higher overpotential voltages are detected at the active electrode regions, close to the electrolyte, as it is where the electrochemical reactions occur due to limiting ionic conductivities. However, the overpotential does not follow the general trend at 1.5 V. It tends to 0 V at the air side and is close to 0 V at the electrolyte/fuel electrode interface, increasing through the fuel electrode towards the fuel channel. This behavior is due to fuel starvation taking place at such high voltage. When fuel starvation occurs, there will not be any electrochemical reaction occurring in electrolysis mode as there is no fuel left to react, resulting in no overpotential nor current density increase. Gas diffusion limitations increase as fuel is consumed explaining the behavior of the fuel electrode overpotential when starvation takes place. Thus, most of the reaction will occur where there is a bit of reactant left, i.e., at the gas channels and consequently, the overpotential increases at the fuel electrode as reported. A more detailed explanation about the fuel starvation phenomenon at 1.5 V can be observed in Figure 5.4 as a result of the capacity of this model to evaluate the cell behavior under critical operating conditions.

The distribution of the steam partial pressure at the fuel active/diffusion interface in Figure 5.4a indicates that there is no reactant left half-way from the fuel inlet, located at $y = 40$ mm. The fuel, H_2/H_2O, flows from $y = 40$ to $y = 0$ mm while air flows from $x = 0$ to $x = 20$ mm. The same but in overpotential terms is shown in Figure 5.4b. The overpotential profile through the electrodes and electrolyte at four different cell points at 1.5 V is presented. The four correspond to the different fuel and air inlet/outlet combinations. In red, the overpotentials corresponding to the fuel inlet while in blue, the ones corresponding to the fuel outlet.

At the fuel inlet, the overpotentials follow the same distribution as presented in Figure 3.2, which is the most common, high overpotential at the electrolyte/ electrode interface due to the electrochemical reactions and tending to zero at the end of the electrode as the active electrochemical area reaches the end. Yet, at the fuel outlet, as there is no reactant left, and no electrochemical reaction can take place as explained above.

(a) p_{H_2O} *profile*

(b) *Overpotential profile*

(c) *Temperature at the fuel outlet*
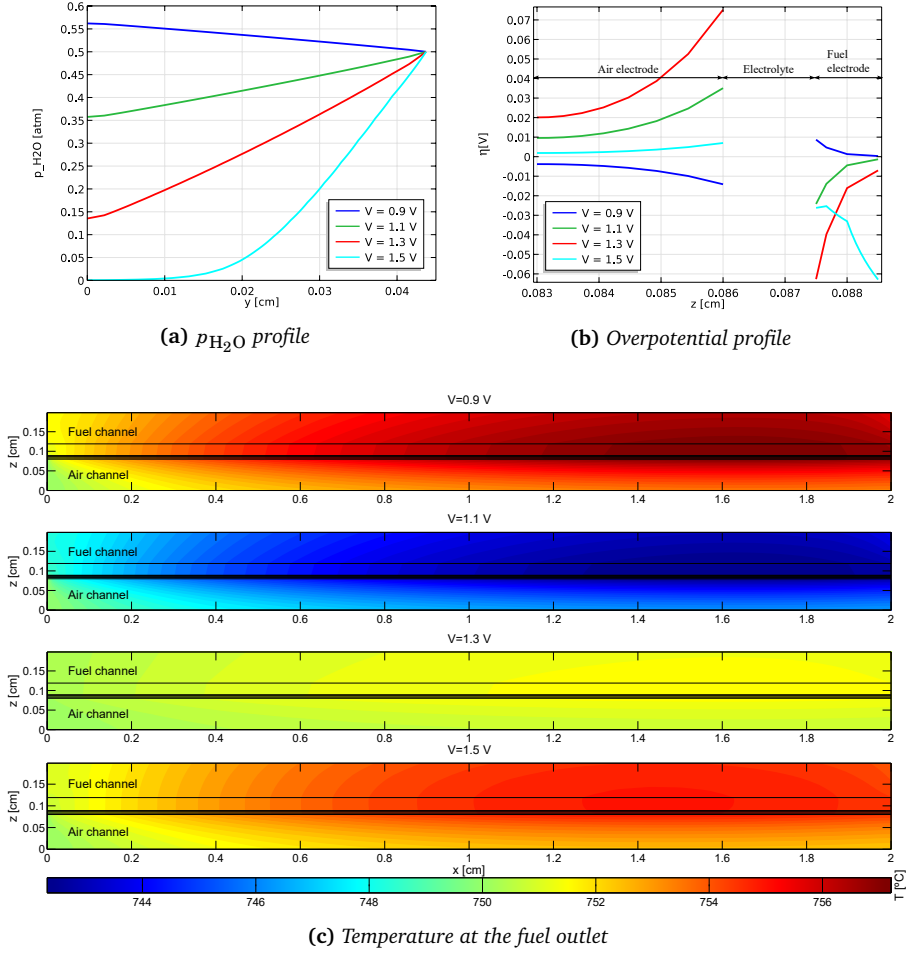
Figure 5.3: p_{H_2O} *profile along the fuel direction, overpotential distribution through the cell and temperature distribution at the fuel outlet for four different cell voltages at inlet $p_{H_2O} = 0.5$ and 750 °C.*

(a) $p_{\mathrm{H_2O}}$ *distribution*

(b) *Overpotential profile*
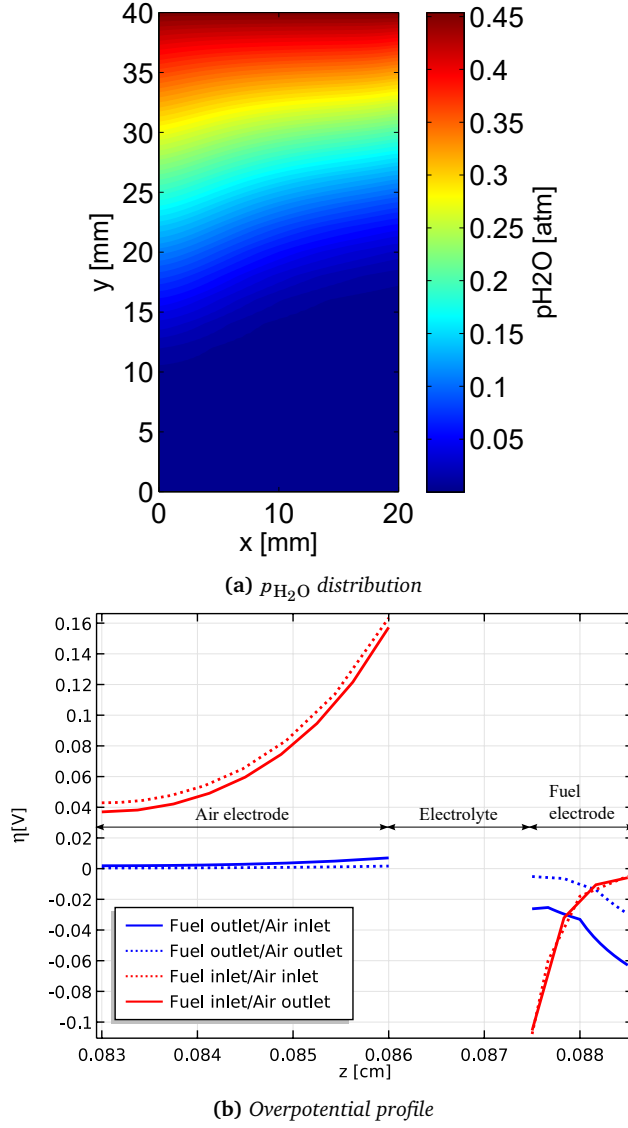
Figure 5.4: *Fuel starvation at 1.5 V. Distribution of: a) $p_{\mathrm{H_2O}}$ at the active/diffusion fuel electrode interface and b) overpotential through the cell at four different points.*

An electrolysis cell shows different thermal behaviors as function of the operating cell voltage, as the cell can be run below, above or at the thermo-neutral voltage. The temperature profiles at the fuel outlet for the four stated voltages are shown in Figure 5.3c. From top to bottom, the different temperature profiles are displayed for increasing cell voltage.

- At 0.9 V, fuel cell operation mode, results in exothermic behavior as the general electrochemical reaction for hydrogen is highly exothermic. Moreover, the contribution from Joule heating always results in a positive net heat flux. This is proved by a temperature increase of about 8 °C along the flow direction.

- At 1.1 V, electrolysis operation mode and a cell voltage below the thermo-neutral point for steam at 750 °C, the cell behaves as endothermic. Despite heat is supplied from the furnace, a temperature decrease of 8 °C is observed.

- At 1.3 V, electrolysis operation mode and a cell voltage very close to the thermo-neutral voltage, the net heat transfer should be almost zero if no extra heat is supplied to the cell. Figure 5.3c shows a 2 °C temperature increase along the fuel flow direction.

- At 1.5 V, electrolysis operation mode and a cell voltage above the thermo-neutral point, a temperature increase along the flow direction proves the positive net heat flux.

At higher cell voltages, higher current densities are achieved meaning higher steam utilization and thus, more hydrogen is produced. The temperature gradient should not be too large to avoid cell damage. Still, due to fuel starvation close to the cell outlets at 1.5 V, the temperature difference at the outlet of the cell channel is only 5 °C, due to no contribution from the electrochemical reactions. If the heat supply from the furnace where the cell is mounted was not taken into consideration, larger temperature gradients would have been reported.

Moreover, in **Paper III**, the importance of including heat transfer when performing simulations as well as the distribution of current, temperature, potential and overpotentials as well as steam for one specific operating voltage are presented.

5.3. Paper IV

In **Paper IV**, carbon deposition as a degradation phenomenon in solid oxide electrolysis cells was treated extensively. The validation presented in Chapter 4, demonstrated that the model can simulate an SOEC with CO/CO_2 as feedstock, see Figure 4.4. It is also shown that carbon deposition occurs due to local crossing of the thermodynamic carbon deposition threshold, a phenomenon which has been observed both experimentally and in simulations, see Figure 4.5. The major findings are presented as follows.

A base case was defined to study the effect of the fuel electrode's porosity, thickness and ionic conductivity on the carbon deposition phenomenon. The specified inlet conditions for the base case defined are 750 °C, 2 Lh^{-1} of CO and 13 Lh^{-1} of CO_2 at standard conditions. The cell voltage for the base case is 1.31 V, which corresponds to a cell voltage where carbon formation is first detected under the specified inlet conditions. Moreover, two different heat boundaries were considered to study their effect on carbon deposition. The first condition corresponds to a specified heat flux boundary to account for a furnace, where the cell is mounted reflecting the experimental setup, see **Paper III** and **IV** for all the details, while the other corresponds to thermal insulation (adiabatic, $q_{furnace} = 0$). The partial pressure distribution of carbon monoxide, p_{CO}, and the temperature distribution throughout the cell are two variables that can impact on the carbon deposition phenomenon. For analyzing the effect of the different geometric parameters on carbon formation, a detailed distribution of these variables in the cell domain is necessary, see Figure 5.5. For Figure 5.5 and the forthcoming figures, different plane locations have been defined for showing the distribution of certain variables. These plane locations correspond to the active layer/diffusion layer interface at the fuel electrode and three vertical planes in the fuel flow direction. For more details about the plane locations, refer to Figure 6 in **Paper IV**.

Effect of thermal boundary condition

The temperature and the CO partial pressure distribution, respectively, when considering the heat flux boundary condition are shown in Figures 5.5a and 5.5c while Figures 5.5b and 5.5d show the distribution of such parameters for the thermally insulated case. The distributions shown correspond to the fuel active/support layer interface.

(a) *T with heat flux boundary condition*

(b) *T with thermal insulation*

(c) p_{CO} *with heat flux boundary condition*

(d) p_{CO} *with thermal insulation*
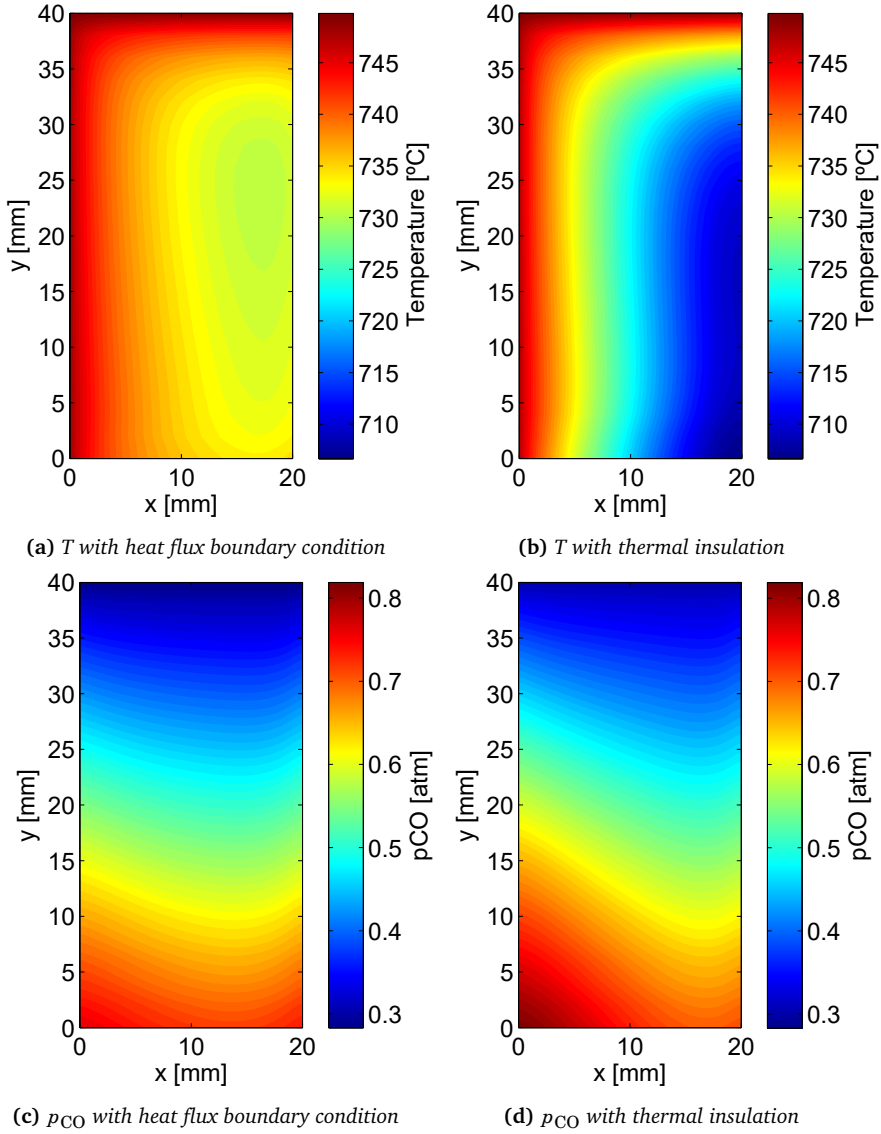
Figure 5.5: *Temperature and partial pressure of CO at the active/support layer interface with heat flux or thermal insulation as boundary condition.*

A temperature decrease along the air and fuel flows is observed for the two defined heat boundary conditions, see Figures 5.5a and 5.5b. The fuel flows from $y = 40$ mm to $y = 0$ mm, and the air flows, from $x = 0$ mm to $x = 20$ mm. This decrease in temperature is due to that the operating cell voltage, 1.31 V, corresponds to a cell voltage below the thermo-neutral point for CO_2 electrolysis at 750 °C (1.46 V). And when operating under the thermo-neutral voltage, the corresponding endothermic electrochemical reactions dominate over Joule heating, leading to an endothermic cell behavior, as seen in **Paper III**. For the thermally insulated case, the coldest region in the cell is at the fuel and air outlets. For the heat flux boundary condition case, the coldest region is shifted a bit upstream due to the heat the cell receives from the surrounding furnace. As the equilibrium constant for the Boudouard is temperature dependent, and consequently also the thermodynamic carbon deposition threshold, which is an indicator for carbon deposition, Eq. (3.20), temperature will affect carbon formation. If temperature decreases, the thermodynamic carbon deposition threshold, $p_{CO,B}$, will be lowered and as the temperature varies through the cell, so will the local threshold do. The lowest local thermodynamic carbon deposition threshold is attained where the lowest temperature is reached in the cell, which corresponds to the thermal insulated condition, Figure 5.5b, due to the heat consumption from the electrochemical reactions. Nevertheless, when the cell receives the heat from the furnace, the temperature gradient across the cell is decreased, see Figure 5.5a, shifting the local thermodynamic threshold. A temperature difference of 43.4 °C is obtained for the thermal insulation boundary while the maximum temperature difference is reduced to 20 °C for the heat flux boundary condition. Hence, by supplying heat to the system, the local thermodynamic threshold can be shifted towards the theoretical value at 750 °C, approaching isothermal conditions as the temperature gradient across the cell is decreased.

The partial pressure of CO increases along the fuel flow direction, from $y = 40$ mm to $y = 0$ mm as shown in Figure 5.5d. The highest p_{CO} value is attained at the fuel outlet, close to the air inlet ($x = 0$ mm) for the thermally insulated case. Figure 5.5d also shows that the CO partial pressure is highest at the electrolyte/fuel active layer interface. Similar tendency is observed for the heat flux condition, only that a more even distribution of the species throughout the cell is achieved, see Figure 5.5c. Highest p_{CO} values are registered at this interface. This fact corroborates that carbon formation in SOEC is electrochemically driven as Duboviks *et al.* [59, 60] pointed out, as it is where the electrochemical conversion of CO_2 to CO (or to C) takes place. Furthermore, higher partial pressure of CO will favor carbon formation as specified by the

Boudouard reaction, Eq. (3.15) or no CO will be formed at all if direct carbon deposition is occurring, Eq. (3.16).

To combine the effects of both temperature and species concentration, the carbon activity, Eq. (3.21), has been plotted for the base case defined in Figure 5.6, for the two described heat boundary conditions. The carbon activity distribution is shown at three vertical planes along the fuel flow direction corresponding to the fuel inlet, middle of the cell and fuel outlet. For the same operating cell voltage, which is 1.31 V, a higher carbon activity is registered for the thermally insulated case. A substantially larger temperature difference across the cell is registered for the thermal insulated boundary condition, see Figure 5.5b, being double of that for the heat flux boundary condition, see Figure 5.5a. This significant temperature decrease can explain the higher carbon activity for the adiabatic case, as the thermodynamic carbon deposition threshold is decreased significantly. Consequently, larger amounts of carbon are formed when thermal insulation is considered as the partial pressure values of CO registered for both heat boundary conditions do not differ as much as temperatures do. Furthermore, it can be clearly observed that the most carbon formation prone region is located at the fuel and air outlets, at the fuel electrode active layer close to the electrolyte interface, see Figures 5.6a and 5.6b.

High enough local concentration of CO can cause carbon deposition. A possible explanation is gas diffusion limitations away from the reaction sites at the electrode/electrolyte interface, where CO_2 has to diffuse a longer distance, increasing the concentration of CO at this interface. Temperature is another factor that may contribute to carbon formation as above-mentioned. When operating under the thermo-neutral voltage, a temperature decrease through the cell is expected, lowering the local carbon deposition threshold due to its temperature dependency. As temperature decreases along the flow direction when endothermic electrolysis, at certain locations the concentration of CO might not be sufficient for carbon to deposit, but as the flow continues downstream, the temperature decreases and then, carbon forms. Thus, there are multiple scenarios which can cause carbon deposition.
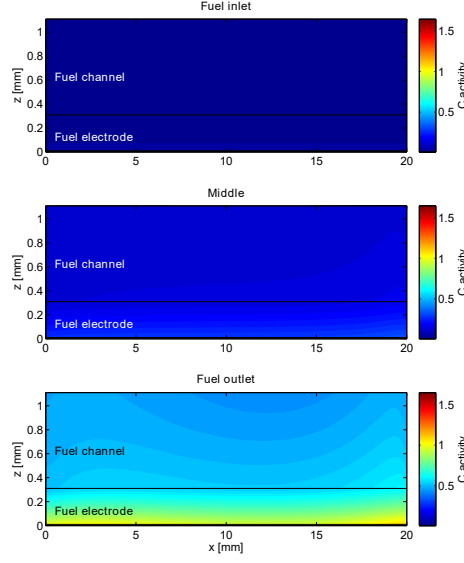
(a) *Heat flux boundary*
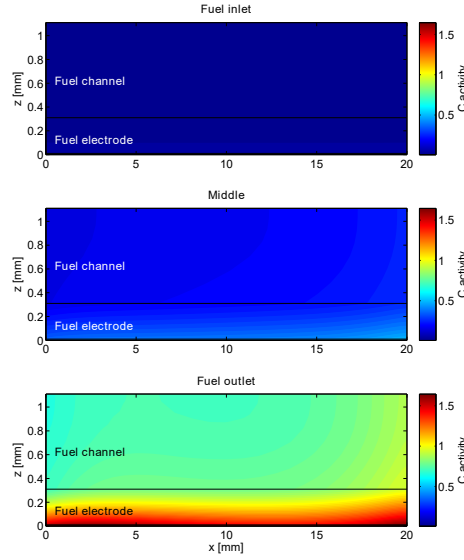
(b) *Thermal insulation boundary*

Figure 5.6: *Carbon activity distribution at different positions along the fuel flow for the base case: (a) with heat boundary condition and (b) with thermal insulation.*

Effect of fuel electrode porosity, thickness and ionic conductivity

A parameter study was performed to study the effect of the fuel electrode porosity, thickness and ionic conductivity on carbon formation. All the results presented were performed when the heat flux boundary condition was contemplated. Being the furnace temperature and the gases inlet temperature fixed to 750 °C.

In the primary y-axis of Figure 5.7, the highest CO partial pressure that can be obtained before carbon deposition is first detected in the cell is shown for the different fuel electrode porosities, thicknesses and ionic conductivity values considered for the study. In the secondary y-axis of Figure 5.7, the corresponding current densities are shown.
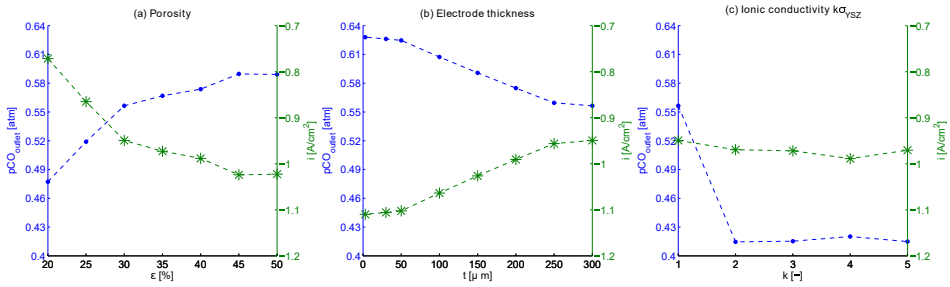
Figure 5.7: *Maximum p_{CO} values obtained before carbon deposition is detected in the cell for different fuel electrode porosity values, thicknesses and ionic conductivities and their corresponding current densities.*

Figure 5.7a shows the maximum p_{CO} values and corresponding current densities for different fuel electrode porosity values. The transport of the fuel molecules, CO_2 and CO, is hindered due to gas diffusion limitations at low porosity values. This results in higher CO partial pressures at the reaction site, favoring carbon formation. Hence, for low porosity values, carbon is detected at lower current densities, and corresponding operating cell voltages, than for higher porosity values. Diffusion limitations decrease when the fuel electrode porosity is increased, reducing the probabilities for carbon deposition to occur. However, for porosity values higher than 30 %, the maximum p_{CO} tends to a plateau. The plateau behavior can be explained by no gas diffusion limitations at high porosity values.

The effect of different fuel electrode thicknesses is shown in Figure 5.7b. The fuel electrode thickness was modified by changing the thickness of the electrode diffusion layer while the thickness of the active layer remained unchanged and set to 10 μm. The thickness values shown in Figure 5.7b correspond to the thickness of the diffusion layer. Diffusion limitations are diminished as the diffusion path is shortened by decreasing the electrode thickness, facilitating the transport of species. The amount of carbon monoxide at the reaction sites is consequently decreased and larger CO partial pressures at the cell outlet can be obtained before carbon formation is detected in the cell, i.e., higher current densities are required in thinner electrodes for carbon detection.

Last, the effect of the fuel electrode ionic conductivity on carbon formation is shown in Figure 5.7c. Due to the temperature dependency of the ionic conductivity of YSZ, see **Paper IV** for the detailed temperature-dependent equation, a factor is taken into account for the variation of this parameter. Higher current densities are achieved with increasing ionic conductivity, favoring the electrochemical reactions' distribution. Consequently, higher p_{CO} values are obtained promoting carbon deposition as dictated by the Boudouard reaction, Eq. (3.18). For further understanding, the overpotential distribution through the air electrode and the fuel active layer are plotted in Figure 5.8 for the different ionic conductivity values at 1.31 V. The operating cell voltage is the one corresponding to the base case, defined above. The overpotentials are plotted at the air and fuel outlets, like it is done in Figures 12, 13 and 14 in **Paper IV**.

The overpotential distribution at 1.31 V shown in Figure 5.8 corroborates that at higher ionic conductivities, carbon deposition is favored for the same inlet flow rates at this voltage. Considering that 1.31 V is the cell operating voltage where carbon is first detected for the base case ($k_\sigma = 1$), higher fuel overpotential values are achieved at the electrode/electrolyte interface due to limitations of the ionic conductivities. At higher conductivity values, charge transfer is increased, spreading out the reaction zone across the electrode and higher p_{CO} values are registered as explained above.

Moreover, **Paper IV** also presents the detailed distribution of the local partial pressure of CO, the local thermodynamic threshold ($p_{CO,B}$) and the temperature at the fuel/air outlets through the cell thickness for different fuel electrode porosity values, thicknesses and ionic conductivity values.
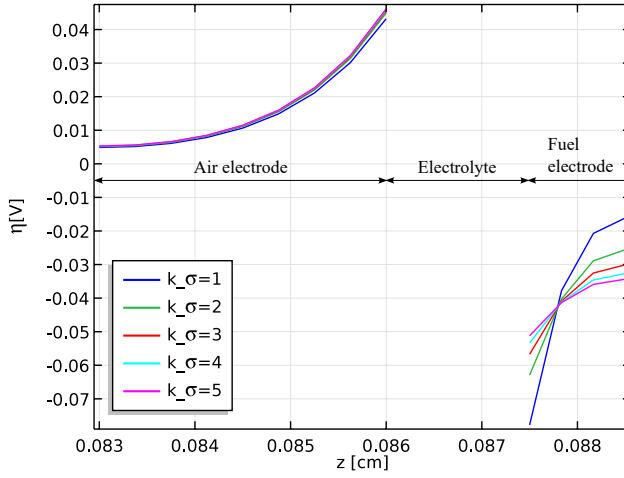
Figure 5.8: *Overpotential distribution through the active electrodes for the different fuel electrode ionic conductivities at the fuel/air outlets at 1.31* V.

CHAPTER 6

Conclusions

Research reported here aimed at developing a three-dimensional model of a solid oxide cell as complete and reliable as possible to predict the performance of it under certain operating conditions and better understanding of the physical phenomena as well as carbon deposition as degradation phenomenon. The scientific contributions can be summarized as:

- Modeling

  1. A 3D model of a fuel electrode planar solid oxide cell has been developed and described in detail. The model, which considers the main physical phenomena taking place in such devices, allows a detailed description of the overpotential through cell thickness, an important feature for studying degradation phenomena. The detailed overpotential spatial resolution has not described in such detail before.

  2. A thorough validation of the model has been presented with two feedstocks, H_2/H_2O and CO/CO_2, at different temperatures, flows

and compositions, where the deviation with respect to the cell voltage has been maximum of 1.2 % for CO/CO_2 electrolysis, 1.3 % for H_2/H_2O electrolysis and 6 % for H_2/H_2O in fuel cell mode. Such broad validation has not been reported before for computational models at continuum level.

3. The capability of this model to evaluate the overpotential distribution through the cell in detail has been demonstrated for steam starvation at high operating cell voltages.

4. The effect of considering heat transfer in the model in electrolysis mode is particularly observed at high voltages, where the impact on the current density is noticeable, resulting in a higher hydrogen production due to higher current densities achieved.

5. A new tool is now available for understanding and predicting degradation and failure mechanisms of SOCs.

- Carbon deposition

  1. Local crossing of the thermodynamic carbon deposition threshold has been observed both experimentally and numerically, with a good agreement between the two methods, validating the model even further.

  2. The concentration of CO and temperature affecting the local thermodynamic carbon deposition threshold have been quantified. Gas diffusion limitations favor carbon formation in SOECs.

  3. Different heat boundary conditions affect the local values of CO concentration and temperature but the carbon activity is similar at the same voltage, showing a lower sensitivity to temperature.

  4. The impact of porosity, conductivity and thickness of the fuel electrode on the thermodynamic carbon deposition threshold has been quantified in terms of temperature and CO concentration.

  5. Finding an optimal point of operation in SOCs is challenging due to the complexity through cross-coupling phenomena.

The model presented is a good tool for evaluating the performance of an SOEC under different operating conditions. Despite its reliability, the model is currently still under development for improvement. Several aspects have been taken into consideration, being the improvement of the mass diffusion model the first priority. Furthermore, it is intended the use of impedance data to model the conductivity for all the cell components from ohmic resistances to obtain more realistic values for the existing cells.

CHAPTER 7

Outlook

Despite the research in SOCs, and specially in SOECs, has increased in the latest years, there is still lot to be done before leaving no stone unturned, specifically in terms of modeling. Computational modeling is a strong tool for simulation of the cell performance under specific conditions and which can be of valuable help if the developed model is trustworthy. Thus, a model itself is meaningless if no proper validation with reliable experimental data is done. Yet, SOCs are in continue development and so does the modeling field, leaving space for a whole room of improvement. The thesis has addressed several individual issues that will improve the quality of the model developed in the work. Nevertheless, the suggestions for improving SOECs modeling are:

- Use microstructure reconstruction for obtaining microstructural parameters of the cell as well as specific transport properties instead of calculating effective transport properties, as it is currently done in most macrostructure models. This could be of great help to rule out uncertainty regarding the material parameters relating to microstructure, i.e., tortuosity and

porosity. A proper microstructure characterization is at hand and thus modeling the influence of all the physical phenomena in the cell, i.e., diffusion paths, available 3PBs, etc.

- Consider the interconnects at cell level and study the transport phenomena limitations due to this stack component, e.g., mass and current transport.

- Quantify the existing deviation between the different existing mass diffusion coefficient equations.

- More attention and effort should be set into modeling stacks of SOCs to shorten the path to mass production. A single cell model allows the study of the physical phenomena, but considering a cell stack can provide useful performance information which might be key for large scale applications.

- Study the effect of considering radiation in a single cell and in a stack model. Both in terms of effects on the cell performance itself as well as on the computational times required.

- Scaling up from stack modeling, system modeling should also be taken into account where the economics of the whole process could also be evaluated.

Last, one should bare in mind that increasing the complexity of the system usually translates into longer computational times. For being successful, the optimum between complexity and computational cost/time should be found. If experiments take less time than numerical calculations, performing simulations will be called into question.

Bibliography

[1] I. E. Agency, "Renewable electricity generation climbs to second place after coal." `http://www.iea.org/newsroom/news/2015/august/renewable-electricity-generation-climbs-to-second-place-after-coal.html`, 2015. Accessed: 2016-10-10.

[2] C. Graves, S. D. Ebbesen, S. H. Jensen, S. B. Simonsen, and M. B. Mogensen, "Eliminating degradation in solid oxide electrochemical cells by reversible operation," *Nature Materials*, vol. 14, no. 2, pp. 239–244, 2015.

[3] M. Saxe, *Bringing Fuel Cells to Reality and Reality to Fuel Cells*. Doctoral dissertation, Royal Institute of Technology (KTH), 2008.

[4] W. Grove, "On voltaic series and the combination of gases by platinum," *Philosophical Magazine*, vol. 14, 1839.

[5] H. Davy, "An account of a method of constructing simple and compound galvanic combinations, without the use of metallic substances, by means of charcoal and different fluids," *Nicholson's Journal of Natural Philosophy*, p. 144, 1802.

[6] EG and I. G Technical Services, "Fuel cell handbook," tech. rep., U.S. Dept. of Energy, 2004.

[7] P. Holtappels, L. G. J. de Haart, and U. Stimming, "Reaction of Hydrogen/Water Mixtures on Nickel/Zirconia Cermet Electrodes: I. DC Polarization Characteristics," *Journal of The Electrochemical Society*, vol. 146, no. 5, pp. 1620–1625, 1999.

[8] P. Holtappels, I. C. Vinke, L. G. J. de Haart, and U. Stimming, "Reaction of Hydrogen/Water Mixtures on Nickel/Zirconia Cermet Electrodes: II. AC Polarization Characteristics," *Journal of The Electrochemical Society*, vol. 146, no. 8, pp. 2976–2982, 1999.

[9] S. P. Jiang and S. P. S. Badwal, "Hydrogen Oxidation at the Nickel and Platinum Electrodes on Yttria/Tetragonal Zirconia Electrolyte," *Journal of The Electrochemical Society*, vol. 144, no. 11, pp. 3777–3784, 1997.

[10] S. P. Jiang and S. P. S. Badwal, "An electrode kinetics study of H_2 oxidation on Ni/Y_2O_3–ZrO_2 cermet electrode of the solid oxide fuel cell," *Solid State Ionics*, vol. 123, no. 1–4, pp. 209–224, 1999.

[11] M. Mogensen and S. Skaarup, "Kinetic and geometric aspects of solid oxide fuel cell electrodes," *Solid State Ionics*, vol. 86, pp. 1151–1160, 1996.

[12] R. M. Ormerod, "Solid oxide fuel cells," *Chemical Society Reviews*, vol. 32, no. 1, pp. 17–28, 2003.

[13] A. L. Dicks, "Advances in catalysts for internal reforming in high temperature fuel cells," *Journal of Power Sources*, vol. 71, no. 1–2, pp. 111–122, 1998.

[14] S. H. Clarke, A. L. Dicks, K. Pointon, T. A. Smith, and A. Swann, "Catalytic aspects of the steam reforming of hydrocarbons in internal reforming fuel cells," *Catalysis Today*, vol. 38, no. 4, pp. 411–423, 1997.

[15] J. Holladay, J. Hu, D. King, and Y. Wang, "An overview of hydrogen production technologies," *Catalysis Today*, vol. 139, no. 4, pp. 244 – 260, 2009.

[16] M. Ni, "Computational fluid dynamics modeling of a solid oxide electrolyzer cell for hydrogen production," *International Journal of Hydrogen Energy*, vol. 34, no. 18, pp. 7795–7806, 2009.

[17] I. E. Agency, "Hydrogen production and storage," tech. rep., International Energy Agency, 2006.

[18] S. A. Sherif, F. Barbir, and T. N. Veziroglu, "Wind energy and the hydrogen economy-review of the technology," *Solar Energy*, vol. 78, no. 5, pp. 647–660, 2005.

[19] M. Ni, D. Y. C. Leung, M. K. H. Leung, and K. Sumathy, "An overview of hydrogen production from biomass," *Fuel Processing Technology*, vol. 87, no. 5, pp. 461–472, 2006.

[20] M. S. Lee, D. Y. Goswami, and E. K. Stefanakos, "Immobilization of calcium oxide solid reactant on a yttria fabric and thermodynamic analysis of UT-3 thermochemical hydrogen production cycle," *International Journal of Hydrogen Energy*, vol. 34, no. 2, pp. 745–752, 2009.

[21] C. Graves, S. D. Ebbesen, M. Mogensen, and K. S. Lackner, "Sustainable hydrocarbon fuels by recycling CO_2 and H_2O with renewable or nuclear energy," *Renewable and Sustainable Energy Reviews*, vol. 15, no. 1, pp. 1–23, 2011.

[22] J. Sigurvinsson, C. Mansilla, P. Lovera, and F. Werkoff, "Can high temperature steam electrolysis function with geothermal heat?," *International Journal of Hydrogen Energy*, vol. 32, no. 9, pp. 1174–1182, 2007.

[23] J. S. Herring, J. E. O'Brien, C. M. Stoots, G. L. Hawkes, J. J. Hartvigsen, and M. Shahnam, "Progress in high-temperature electrolysis for hydrogen production using planar SOFC technology," *International Journal of Hydrogen Energy*, vol. 32, no. 4, pp. 440–450, 2007.

[24] C. Chatzichristodoulou, M. Chen, P. V. Hendriksen, T. Jacobsen, and M. B. Mogensen, "Understanding degradation of solid oxide electrolysis cells through modeling of electrochemical potential profiles," *Electrochimica Acta*, vol. 189, pp. 265–282, 2016.

[25] M. Ni, M. K. H. Leung, and D. Y. C. Leung, "A modeling study on concentration overpotentials of a reversible solid oxide fuel cell," *Journal of Power Sources*, vol. 163, no. 1, pp. 460–466, 2006.

[26] J. P. Stempien, Q. Sun, and S. H. Chan, "Solid Oxyde Electrolyzer Cell Modeling: A Review," *Journal of Power Technologies*, vol. 93, no. 4, pp. 216–246, 2013.

[27] J. Golbert, C. S. Adjiman, and N. P. Brandon, "Microstructural Modeling of Solid Oxide Fuel Cell Anodes," *Industrial & Engineering Chemistry Research*, vol. 47, no. 20, pp. 7693–7699, 2008.

[28] S. Kakaç, A. Pramuanjaroenkij, and X. Y. Zhou, "A review of numerical modeling of solid oxide fuel cells," *International Journal of Hydrogen Energy*, vol. 32, no. 7, pp. 761–786, 2007.

[29] E. Achenbach and E. Riensche, "Methane/steam reforming kinetics for solid oxide fuel cells," *Journal of Power Sources*, vol. 52, no. 2, pp. 283–288, 1994.

[30] S. H. Chan, K. A. Khor, and Z. T. Xia, "A complete polarization model of a solid oxide fuel cell and its sensitivity to the change of cell component thickness," *Journal of Power Sources*, vol. 93, no. 1–2, pp. 130–140, 2001.

[31] J. Laurencin, D. Kane, G. Delette, J. Deseure, and F. Lefebvre-Joud, "Modelling of solid oxide steam electrolyser: Impact of the operating conditions on hydrogen production," *Journal of Power Sources*, vol. 196, no. 4, pp. 2080–2093, 2011.

[32] G. Hawkes, J. O'Brien, C. Stoots, and B. Hawkes, "3D CFD model of a multi-cell high-temperature electrolysis stack," *International Journal of Hydrogen Energy*, vol. 34, no. 9, pp. 4189–4197, 2009.

[33] J. E. O'Brien, M. G. McKellar, C. M. Stoots, J. S. Herring, and G. L. Hawkes, "Parametric study of large-scale production of syngas via high-temperature co-electrolysis," *International Journal of Hydrogen Energy*, vol. 34, no. 9, pp. 4216–4226, 2009.

[34] J. E. O'Brien, "Thermodynamics and Transport Phenomena in High Temperature Steam Electrolysis Cells," *Journal of Heat Transfer*, vol. 134, no. 3, pp. 031017–031017, 2012.

[35] T. Boëdec, M. Reytier, D. Lhachemi, D. Tschumperlé, P. Louat, S. Di Iorio, P. Baurens, and G. Delette, "A New Stack to Validate Technical Solutions and Numerical Simulations," *Fuel Cells*, vol. 12, no. 2, pp. 239–247, 2012.

[36] Q. Cai, C. S. Adjiman, and N. P. Brandon, "Modelling the 3D microstructure and performance of solid oxide fuel cell electrodes: Computational parameters," *Electrochimica Acta*, vol. 56, no. 16, pp. 5804–5814, 2011.

[37] P. Costamagna and K. Honegger, "Modeling of Solid Oxide Heat Exchanger Integrated Stacks and Simulation at High Fuel Utilization," *Journal of The Electrochemical Society*, vol. 145, no. 11, p. 13, 1998.

[38] W. K. S. Chiu, A. S. Joshi, and K. N. Grew, "Lattice Boltzmann model for multi-component mass transfer in a solid oxide fuel cell anode with heterogeneous internal reformation and electrochemistry," *The European Physical Journal - Special Topics*, vol. 171, no. 1, pp. 159–165, 2009.

[39] N. Jeong, D. H. Choi, and C.-L. Lin, "Estimation of thermal and mass diffusivity in a porous medium of complex structure using a lattice Boltzmann method," *International Journal of Heat and Mass Transfer*, vol. 51, no. 15–16, pp. 3913–3923, 2008.

[40] S. Arcidiacono, I. Karlin, J. Mantzaras, and C. Frouzakis, "Lattice Boltzmann model for the simulation of multicomponent mixtures," *Physical Review*, vol. 76, pp. 046703–1, 2007.

[41] A. Tarancón, A. Morata, F. Peiró, and G. Dezanneau, "A Molecular Dynamics Study on the Oxygen Diffusion in Doped Fluorites: The Effect of the Dopant Distribution," *Fuel Cells*, vol. 11, no. 1, pp. 26–37, 2011.

[42] Y. Nishida and S. Itoh, "A modeling study of porous composite microstructures for solid oxide fuel cell anodes," *Electrochimica Acta*, vol. 56, no. 7, pp. 2792–2800, 2011.

[43] C. A. J. Fisher and H. Matsubara, "Molecular dynamics investigations of grain boundary phenomena in cubic zirconia," *Computational Materials Science*, vol. 14, no. 1-4, pp. 177–184, 1999.

[44] D. A. Noren and M. A. Hoffman, "Clarifying the Butler–Volmer equation and related approximations for calculating activation losses in solid oxide fuel cell models," *Journal of Power Sources*, vol. 152, no. 0, pp. 175–181, 2005.

[45] P. Gellings and H. Bouwmeester, *The CRC Handbook of Solid State Electrochemistry*. Boca Raton, Fl: CRC press, 1997.

[46] M. Ni, "Modeling of a solid oxide electrolysis cell for carbon dioxide electrolysis," *Chemical Engineering Journal*, vol. 164, no. 1, pp. 246–254, 2010.

[47] D. Grondin, J. Deseure, A. Brisse, M. Zahid, and P. Ozil, "Simulation of a high temperature electrolyzer," *Journal of Applied Electrochemistry*, vol. 40, no. 5, pp. 933–941, 2010.

[48] M. Ni, M. K. H. Leung, and D. Y. C. Leung, "Mathematical modeling of the coupled transport and electrochemical reactions in solid oxide steam electrolyzer for hydrogen production," *Electrochimica Acta*, vol. 52, no. 24, pp. 6707–6718, 2007.

[49] J. Udagawa, P. Aguiar, and N. P. Brandon, "Hydrogen production through steam electrolysis: Control strategies for a cathode-supported intermediate temperature solid oxide electrolysis cell," *Journal of Power Sources*, vol. 180, no. 1, pp. 354–364, 2008.

[50] Q. Cai, E. Luna-Ortiz, C. S. Adjiman, and N. P. Brandon, "The Effects of Operating Conditions on the Performance of a Solid Oxide Steam Electrolyser: A Model-Based Study," *Fuel Cells*, vol. 10, no. 6, pp. 1114–1128, 2010.

[51] X. Jin and X. Xue, "Computational fluid dynamics analysis of solid oxide electrolysis cells with delaminations," *International Journal of Hydrogen Energy*, vol. 35, no. 14, pp. 7321–7328, 2010.

[52] D. Klotz, A. Leonide, A. Weber, and E. Ivers-Tiffée, "Electrochemical model for SOFC and SOEC mode predicting performance and efficiency," *International Journal of Hydrogen Energy*, vol. 39, no. 35, pp. 20844–20849, 2014.

[53] T. Ishihara, S. Matsushita, T. Sakai, and H. Matsumoto, "Intermediate temperature solid oxide electrolysis cell using $LaGaO_3$-base oxide," *Solid State Ionics*, vol. 225, pp. 77–80, 2012.

[54] M. A. Laguna-Bercero, R. Campana, A. Larrea, J. A. Kilner, and V. M. Orera, "Performance and Aging of Microtubular YSZ-based Solid Oxide Regenerative Fuel Cells," *Fuel Cells*, vol. 11, no. 1, pp. 116–123, 2011.

[55] M. Mogensen, H. L. Frandsen, J. Nielsen, W. Li, T. Jacobsen, and C. Graves, "Current density - overvoltage relations for solid oxide electrodes." Smart Energy Conversion and Storage Conference, Krynica, Poland, 2013.

[56] H. Chang and G. Jaffé, "Polarization in Electrolytic Solutions. Part I. Theory," *The Journal of Chemical Physics*, vol. 20, no. 7, pp. 1071–1077, 1952.

[57] R. T. DeHoff, *Thermodynamics in materials science*. McGraw-Hill, 1993.

[58] T. Jacobsen and M. Mogensen, "The course of oxygen partial pressure and electric potentials across an oxide electrolyte cell," *ECS Transactions*, vol. 13, no. 26, pp. 259–273, 2008.

[59] V. Duboviks, M. Lomberg, R. C. Maher, L. F. Cohen, N. P. Brandon, and G. J. Offer, "Carbon deposition behaviour in metal-infiltrated gadolinia doped ceria electrodes for simulated biogas upgrading in solid oxide electrolysis cells," *Journal of Power Sources*, vol. 293, pp. 912–921, 2015.

[60] V. Duboviks, R. Maher, M. Kishimoto, L. Cohen, N. Brandon, and G. Offer, "A raman spectroscopic study of the carbon deposition mechanism on ni/cgo electrodes during CO/CO_2 electrolysis," *Physical Chemistry Chemical Physics*, vol. 16, no. 26, pp. 13063–13068, 2014.

66

[61] T. Skafte, C. Graves, P. Blennow, and J. Hjelm, "Carbon Deposition during CO_2 Electrolysis in Ni-based Solid Oxide Cell Electrodes," *ECS Transactions*, vol. 68, no. 1, pp. 3429–3437, 2015.

[62] S. Sohn, J. H. Nam, D. H. Jeon, and C.-J. Kim, "A micro/macroscale model for intermediate temperature solid oxide fuel cells with prescribed fully-developed axial velocity profiles in gas channels," *International Journal of Hydrogen Energy*, vol. 35, no. 21, pp. 11890–11907, 2010.

[63] K. N. Grew, A. S. Joshi, A. A. Peracchio, and W. K. S. Chiu, "Pore-scale investigation of mass transport and electrochemistry in a solid oxide fuel cell anode," *Journal of Power Sources*, vol. 195, no. 8, pp. 2331–2345, 2010.

[64] G. Reiss, H. L. Frandsen, A. H. Persson, C. Weiß, and W. Brandstätter, "Numerical evaluation of oxide growth in metallic support microstructures of Solid Oxide Fuel Cells and its influence on mass transport," *Journal of Power Sources*, vol. 297, pp. 388–399, 2015.

[65] K. Tseronis, I. K. Kookos, and C. Theodoropoulos, "Modelling mass transport in solid oxide fuel cell anodes: a case for a multidimensional dusty gas-based model," *Chemical Engineering Science*, vol. 63, no. 23, pp. 5626–5638, 2008.

[66] S. Wang, W. M. Worek, and W. J. Minkowycz, "Performance comparison of the mass transfer models with internal reforming for solid oxide fuel cell anodes," *International Journal of Heat and Mass Transfer*, vol. 55, no. 15–16, pp. 3933–3945, 2012.

[67] J. Shi and X. Xue, "CFD analysis of a symmetrical planar SOFC with heterogeneous electrode properties," *Electrochimica Acta*, vol. 55, no. 18, pp. 5263–5273, 2010.

[68] R. Bove and S. Ubertini, "Modeling solid oxide fuel cell operation: Approaches, techniques and results," *Journal of Power Sources*, vol. 159, no. 1, pp. 543–559, 2006.

[69] D. Grondin, J. Deseure, P. Ozil, J. P. Chabriat, B. Grondin-Perez, and A. Brisse, "Solid oxide electrolysis cell 3D simulation using artificial neural network for cathodic process description," *Chemical Engineering Research and Design*, vol. 91, no. 1, pp. 134–140, 2013.

[70] V. M. Janardhanan and O. Deutschmann, "CFD analysis of a solid oxide fuel cell with internal reforming: Coupled interactions of transport,

heterogeneous catalysis and electrochemical processes," *Journal of Power Sources*, vol. 162, no. 2, pp. 1192–1202, 2006.

[71] J. Udagawa, P. Aguiar, and N. P. Brandon, "Hydrogen production through steam electrolysis: Model-based steady state performance of a cathode-supported intermediate temperature solid oxide electrolysis cell," *Journal of Power Sources*, vol. 166, no. 1, pp. 127–136, 2007.

[72] N. Autissier, D. Larrain, J. Van herle, and D. Favrat, "Cfd simulation tool for solid oxide fuel cells," *Journal of Power Sources*, vol. 131, no. 1–2, pp. 313–319, 2004.

[73] M. Ni, "2D thermal modeling of a solid oxide electrolyzer cell (SOEC) for syngas production by H_2O/CO_2 co-electrolysis," *International Journal of Hydrogen Energy*, vol. 37, no. 8, pp. 6389–6399, 2012.

[74] D. Young, B. Munson, T. Okiishi, and W. Huebesch, *Introduction to Fluid Mechanics*. John Wiley & Sons, 5 ed., 2012.

[75] J. H. Nam and D. H. Jeon, "A comprehensive micro-scale model for transport and reaction in intermediate temperature solid oxide fuel cells," *Electrochimica Acta*, vol. 51, no. 17, pp. 3446–3460, 2006.

[76] R. Suwanwarangkul, E. Croiset, M. W. Fowler, P. L. Douglas, E. Entchev, and M. A. Douglas, "Performance comparison of Fick's, dusty-gas and Stefan–Maxwell models to predict the concentration overpotential of a sofc anode," *Journal of Power Sources*, vol. 122, no. 1, pp. 9–18, 2003.

[77] R. B. Bird, W. E. Stewart, and E. N. Lightfoot, *Transport Phenomena*. New York: Wiley, 1960.

[78] S. W. Webb and K. Pruess, "The Use of Fick's Law for Modeling Trace Gas Diffusion in Porous Media," *Transport in Porous Media*, vol. 51, no. 3, pp. 327–341, 2003.

[79] H. Merk, "The Macroscopic Equations for Simultaneous Heat and Mass Transfer in Isotropic, Continuous and Closed Systems," *Applied Sciences Research*, vol. A8, p. 26, 1959.

[80] J. Yuan and B. Sundén, "On mechanisms and models of multi-component gas diffusion in porous structures of fuel cell electrodes," *International Journal of Heat and Mass Transfer*, vol. 69, pp. 358–374, 2014.

[81] W. Kong, H. Zhu, Z. Fei, and Z. Lin, "A modified dusty gas model in the form of a Fick's model for the prediction of multicomponent mass

transport in a solid oxide fuel cell anode," *Journal of Power Sources*, vol. 206, no. 0, pp. 171–178, 2012.

[82] R. E. Cunningham and R. J. J. Williams, *Diffusion in Gases and Porous Media*. New York: Plenum Press, 1980.

[83] Y. Vural, L. Ma, D. B. Ingham, and M. Pourkashanian, "Comparison of the multicomponent mass transfer models for the prediction of the concentration overpotential for solid oxide fuel cell anodes," *Journal of Power Sources*, vol. 195, no. 15, pp. 4893–4904, 2010.

[84] P. J. A. M. Kerkhof, "A modified Maxwell-Stefan model for transport through inert membranes: the binary friction model," *The Chemical Engineering Journal and the Biochemical Engineering Journal*, vol. 64, no. 3, pp. 319–343, 1996.

[85] S. Wang, W. M. Worek, and W. J. Minkowycz, "Performance comparison of the mass transfer models with internal reforming for solid oxide fuel cell anodes," *International Journal of Heat and Mass Transfer*, vol. 55, no. 15–16, pp. 3933–3945, 2012.

[86] J. B. Young and B. Todd, "Modelling of multi-component gas flows in capillaries and porous solids," *International Journal of Heat and Mass Transfer*, vol. 48, no. 25–26, pp. 5338–5353, 2005.

[87] M. Dumortier, O. Lacroix, and J. Sanchez-Marcano, "Modeling of mass and energy transfers in a high temperature membrane electrolyser," *International Journal of Hydrogen Energy*, no. 0, 2010.

[88] Y. Xie and X. Xue, "Modeling of solid oxide electrolysis cell for syngas generation with detailed surface chemistry," *Solid State Ionics*, vol. 224, no. 0, pp. 64–73, 2012.

[89] W. Li, Y. Shi, Y. Luo, and N. Cai, "Elementary reaction modeling of CO_2/H_2O co-electrolysis cell considering effects of cathode thickness," *Journal of Power Sources*, vol. 243, no. 0, pp. 118–130, 2013.

[90] H. Zhang, J. Wang, S. Su, and J. Chen, "Electrochemical performance characteristics and optimum design strategies of a solid oxide electrolysis cell system for carbon dioxide reduction," *International Journal of Hydrogen Energy*, vol. 38, no. 23, pp. 9609–9618, 2013.

[91] A. Bertei and C. Nicolella, "Common inconsistencies in modeling gas transport in porous electrodes: The dusty-gas model and the Fick law," *Journal of Power Sources*, vol. 279, pp. 133–137, 2015.

[92] R. Krishna and J. A. Wesselingh, "The Maxwell-Stefan approach to mass transfer," *Chemical Engineering Science*, vol. 52, no. 6, pp. 861–911, 1997.

[93] D. L. Damm and A. G. Fedorov, "Radiation heat transfer in SOFC materials and components," *Journal of Power Sources*, vol. 143, no. 1-2, pp. 158–165, 2005.

[94] K. Tseronis, I. S. Fragkopoulos, I. Bonis, and C. Theodoropoulos, "Detailed Multi-dimensional Modeling of Direct Internal Reforming Solid Oxide Fuel Cells," *Fuel Cells*, vol. 16, no. 3, pp. 294–312, 2016.

[95] J. J. Hartvigsen, S. Elangovan, and A. Khandkar, *Modeling, Design and Performance of Solid Oxide Fuel Cells*. Technomic Publishing company, 1993.

[96] V. M. Janardhanan and O. Deutschmann, "Numerical study of mass and heat transport in solid-oxide fuel cells running on humidified methane," *Chemical Engineering Science*, vol. 62, no. 18–20, pp. 5473–5486, 2007.

[97] A. Leonide, S. Hansmann, A. Weber, and E. Ivers-Tiffée, "Performance simulation of current/voltage-characteristics for SOFC single cell by means of detailed impedance analysis," *Journal of Power Sources*, vol. 196, no. 17, pp. 7343–7346, 2011.

[98] H. Wendt and G. Kreysa, *Electrochemical Engineering*. Berlin: Springer, 1999.

[99] T. L. Skafte, C. Graves, P. Blennow, and J. Hjelm, "Carbon deposition and sulfur poisoning during CO_2 electrolysis in ni-based solid-oxide-cell electrodes." Submitted, 2016.

Appended publications

Paper I
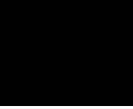
Transport phenomena in solid oxide fuel cell electrodes focusing on heat transfer related to chemical reactions

M Navasa, M Andersson, J Yuan and B Sundén

Department of Energy Sciences, University of Lund, Lund 22100, Sweden

E-mail: `Maria.Navasa@energy.lth.se`

Abstract. Solid oxide fuel cells (SOFCs) are widely studied for their advantages especially at high temperatures. However, operating at high temperatures represents a high cost due to the strict requirements the materials are expected to fulfill. Thus, the main goal in SOFC research has been to decrease the operating temperature so that the range of available materials is widened and hence, the operating cost can be reduced. In this paper, the different heat sources that contribute to the cell energy balance are presented with strong emphasis on the chemical reactions that take place in SOFCs. The knowledge of which heat sources or sinks taking place and their locations within the SOFC can provide useful information for further design and efficiency improvements.

1. Introduction

Solid oxide fuel cells (SOFCs) are high-temperature electrochemical devices which convert the chemical energy of fuels directly into electrical energy in an environmental friendly and efficient manner. For this reason and due to the depletion of fossil fuels, SOFCs are regarded as promising candidates for energy conversion and thus, for being able to obtain electrical power for our society in an environmental friendly way.

When comparing SOFCs to other current fuel cell types, for example, proton exchange membrane fuel cells (PEMFCs), SOFCs present a number of attractive features. SOFCs are fuel flexible, which means that different fuels apart from pure hydrogen can be used due to the tolerance of carbon monoxide (CO), a fuel as well. Then, short-chain hydrocarbon fuels like methane or ethanol among others can be supplied as fuel to SOFCs. Long-chain hydrocarbons can lead to carbon deposition if no previous treatment is done. Moreover, all components are in solid sate (there are no liquid electrolytes like for example in alkaline fuel cells), there are no water management issues, which is the main headache for PEMFCs, and the high quality waste heat produced by SOFCs can be utilized effectively for either combined heat and power or for use in hybrid systems together with gas turbines.

Substantial improvements in performance and durability have been made in the last years in SOFCs mainly due to the advances in manufacturing technology. Although other fuel cells are nowadays more technologically developed, for example, molten carbonate fuel cells, SOFCs are widely considered to be one of the two most promising fuel cells together with PEMFCs.

2. Problem Statement

SOFCs are particularly attractive fuel cells compared to other types as mentioned before and thus, they have become an important area of research and development all over the world in the last years and still nowadays [1].

One of the main characteristics of SOFCs is that they are high-temperature devices. The fact that these cells initially operated at temperatures around $1000°C$ is due to the material of the electrolyte used, yttria stabilized zirconia (YSZ). This is a ceramic material which becomes conductive to oxygen ions at certain temperatures and non-conductive to electrons as well as the anode and cathode materials. Thus, electrochemical reactions can take place at the electrodes without the need of expensive catalysts. In fact, the anode material (YSZ) is catalytic itself for both the internal reforming and electrochemical reactions that take place. The limited range of the available materials to operate at high temperatures is the major limitation to mass production of SOFCs due to the material cost. Nevertheless, long starting times are required for high temperature SOFCs and thermal control becomes difficult despite the high thermal efficiency and long-term stability. In order to be able to mass produce SOFCs, a substantial reduction in the system cost (cell and stack production processes) is required. One way to reduce the costs is by reducing the material costs and increase the durability of the cells. This can be done by reducing the operating temperature to an intermediate temperature, $600\text{-}800°C$ (IT-SOFC), or even lower than $600°C$, (LT-SOFC). When the temperature decreases, the overall performance is reduced because the electrolyte resistance increases and the reactions at the electrode become inactive [1, 2].

However, it is not just a matter of decreasing the operating temperature as other phenomena must be taken into account as well. As well known, the kinetics of the chemical reactions that take place in SOFCs are temperature dependent and this is also a matter of concern. Thus, it is of big interest to know the relationship between the chemical reactions and the heat transfer phenomena.

The main objective of this article is to describe the major concerns of the chemical reactions in SOFCs relating to thermal issues and thus, describe the major sources for heat transfer in SOFCs. How and where they originate and are located to obtain a detailed model for simulation are important so that the overall cell performance can be improved and the further fuel cell development can be promoted.

3. Chemical reactions: heat transfer effects

SOFCs consist of two porous electrodes (an anode and a cathode) separated by a dense electrolyte and connected into an electrically conducting circuit, see Figure 1. The electrodes must present large reaction sites for the electrochemical reactions having a great number of paths for ion and electron conduction and presenting the appropriate porosity for oxygen, hydrogen and the formed water migration. The required properties for the electrolyte are somehow similar to those required for the electrodes but present some variations. The electrolyte must present a high ionic conductivity, high density, long-term high temperature performance stability and high long-term reliability which means high strength and high durability [3].

One of the major concerns for SOFC technology at the temperatures used nowadays is that the steam reforming (SR) reaction rate is much faster than the electrochemical reaction rate. This fact can be explained by the high nickel (Ni) content which is necessary for the electric conductivity and offers a high number of catalytic sites. The steam reforming reaction (Eq.1) is a highly endothermic reaction ($\Delta H° = 206\,\text{kJ}\,\text{mol}^{-1}$) and thus, consumes energy while the electrochemical reactions produce energy as they are exothermic.

If the steam reforming reaction is faster than the electrochemical, there will be cooling at the inlet of the cell and heating at the outlet resulting in a large temperature gradient in the cell. This temperature gradient can cause thermal stress as well as reduced efficiency [4]. The SR reaction takes place in the anode support layer of the fuel cell (FC) while the electrochemical reactions take place at the three-phase boundaries (TPBs) in the reaction active region or functional layer, see Figure 1.
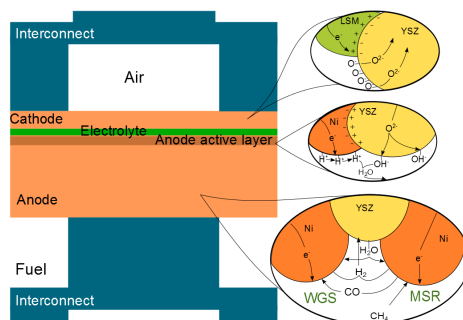
Figure 1. Schematic image of an SOFC with some detail on surface chemistry.

$$CH_4 + H_2O \rightleftharpoons CO + 3H_2 \qquad (1)$$

The steam reforming reaction rate needs to be lowered in order to decrease the existing temperature gradients and thus, improve the cell performance. To do so, detailed knowledge of the steam reforming kinetics is required. At present, steam reforming reaction on Ni based catalysts has been widely studied for catalytic reactors because of its industrial importance. However, few studies have been performed for SOFC.

The goal for optimizing the internal reforming reactions for an SOFC is to lower the reaction rate of the steam reforming reaction while maintaining a high electronic conductivity and a high reactivity for the electrochemical reaction. Yet, high reforming reaction rates are still required compared to the electrochemical reaction rates. To reduce the reforming reaction rate, different solutions have been presented [4, 5]:

- Lowering the temperature. The general trend is to lower the operating temperature as SR has a high activation energy (depending on the mechanism 63.3-228 kJ mol^{-1}, Table 1) and the reaction rate decreases rapidly with temperature. The present lower temperature limit for efficient operation is between $650 - 700°C$ (IT−SOFC) [4, 5] although the current trend is to even decrease it more to 300-600°C (LT−SOFC) by using ceria-based composites as electrolyte [6]. Such low temperatures, close to 300°C, are too low for internal reforming reactions and thus, external reforming is required. The major limitation for decreasing the operating temperature is the ionic conductivity in the electrolyte and thus, the materials used. Different kinetic expressions for the SR reaction over Ni/YSZ anodes have been reported and are shown in Table 1. The different expressions shown seem to vary significantly most probably due to different experimental conditions. Moreover, two types of kinetic expressions are used: power law expressions derived from data fitting from experimental conditions and general Langmuir-Hinshelwood expressions. Furthermore, it was intended to have the same units for the reaction rate in order to be able to compare the different expressions with more precision but the lack of information and the ambiguities with units add difficulty in this task stating that more work needs to be done in this field. Although no activation energy (E_A) value is shown in expression 5, the stated E_A value is calculated experimentally by Bebelis et al. [7].

- Reducing the fuel concentration. The fuel concentration can be decreased by recirculating part of the anode exhaust gas, [5].

- Modification of the Ni/YSZ anode or design of other anode materials to decrease the SR activity. Possibility exists to replace some Ni in the anode by copper (Cu) or using

$Cu/CeO_2/YSZ$ among others. The replacement of some Ni particles by Cu seems to be a promising option as it reduces the reforming rate without a significant reduction in the electrochemical reduction. However, more work needs to be done in this field [4, 5].

- Increase the particle size. For the same amount of Ni particles, the surface area decreases for larger Ni particles and thus, there are less active sites. Moreover, if the particle size in the active anode also increases, the TPB, where electrochemical reactions take place, decreases as well. This means that the Ni particle size also influences the electrical conductivity: when the particle size increases, the electrical conductivity decreases [8]. So, increasing the particle size to decrease the SR rate may reduce the cell performance [4]. However, a better alternative is to use functionally graded particle size electrodes. By this way, a large TPB reaction area near the anode-electrolyte can be obtained while avoiding high diffusion losses by using large particles at the electrodes, away from the boundary [9, 10].

Table 1. Steam reforming reaction kinetics reported for SR over Ni/YSZ SOFC anode/anode−supports. E_A in $\left[\mathrm{kJ\,mol^{-1}}\right]$

Expression r	$[r]$	E_A	T [°C]	k_0, k_{ad}, k^+, k^-	S/C	Ref.
$k_0 P_{CH_4} \exp\left(\frac{-E_A \cdot 1000}{RT_s}\right)$	$\frac{mol}{m^2 s}$	82	700−940	$4274\left[\frac{mol}{m^2 s\,bar}\right]$	2.6−8	[11]
$k_0 P_{CH_4} P_{H_2O} \exp\left(\frac{-E_A \cdot 1000}{RT_s}\right)$	$\frac{mol}{m^2 s}$	205	600−700	$30,8 \cdot 10^{10}\left[\frac{mol}{m^2 s\,bar^2}\right]$	2−3.5	[12]
$k_0 P_{CH_4}^{0.85} P_{H_2O}^{-0.35} \exp\left(\frac{-E_A \cdot 1000}{RT_s}\right)$	$\frac{mol}{m^2 s}$	95	850−900	$8542\left[\frac{mol}{m^2 s\,bar^{0.5}}\right]$	1.5−2.5	[13]
$k_0 P_{CH_4}^{1.3} P_{H_2O}^{-1.2} \exp\left(\frac{-E_A \cdot 1000}{RT_s}\right)$	$\frac{mol}{m^3}$	191	-	$1.01 \cdot 10^{13}\left[\frac{mol}{m^3 bar^{0.1}}\right]$	-	[14]
$k_{ad} P_{CH_4}\left(1 - \frac{k_{ad}}{k_r K_{H_2O}} \frac{P_{H_2} P_{CH_4}}{P_{H_2O}}\right)$	$\frac{mol}{s}$	228	800−900	$k_{ad_{1073K}} = 0.26 \cdot 10^{-6}\left[\frac{mol}{kPa\,s}\right]$	0−2	[7]
$k_0 P_{CH_4}\left(1 - \frac{P_{CO} P_{H_2}^3}{P_{CH_4} P_{H_2O} K_p}\right)\exp\left(\frac{-E_A \cdot 1000}{RT_s}\right)$	$\frac{mol}{m^2 s}$	63,3	650−950	$498\left[\frac{mol}{m^2 s\,bar}\right]$	2	[15]
$\frac{k' K_{adCH_4} P_{CH_4} K_{adH_2O} P_{H_2O}}{\left(1 + K_{adCH_4} P_{CH_4} + K_{adH_2O} P_{H_2O} + K_{adCO} P_{CO}\right)^2}$	$\frac{mol}{m^2 s}$	-	700−1000	-	3−7	[16]
$k_r^+ P_{CH_4} P_{H_2O} - k_r^- P_{CO} P_{H_2O}^3$	$\frac{mol}{m^3 s}$	-	700−950	$k_{r,1073K}^+ = 2.3 \cdot 10^{-8}\left[\frac{mol}{m^3 Pa^2 s}\right]$ $k_{r,1073K}^- = 1.4 \cdot 10^{-20}\left[\frac{mol}{m^3 Pa^4 s}\right]$	3	[17, 18]
$\frac{288.52 P_{CH_4} P_{H_2O} \exp\left(\frac{-11000}{RT_s}\right)}{1 + 16 P_{CH_4} + 0.143 P_{H_2O} \exp\left(\frac{39000}{RT_s}\right)}$	$\frac{mol}{m^2 s}$	-	-	-	-	[19]

One of the main goals in the fuel cell research is to lower the material cost in order to be able to mass produce SOFC. As seen, the current trend in SOFC development is to decrease the operating temperature. By lowering the operating temperature, other phenomena that take place within the SOFC are also affected. Therefore, the relationship between the chemical and electrochemical reactions with temperature is more than obvious. For this reason, considering heat transfer when performing a numerical simulation of an SOFC is of great interest.

4. Heat transfer in SOFCs affected by various reactions

Different phenomena take place in an SOFC at different length scales. As mentioned, chemical reactions are still the least understood phenomena taking place inside the fuel cell and the need to model at small length scales so that the different chemical species (surface species, ions, etc.) can be distinguished and thus, the existing reaction mechanisms implemented, is more than obvious in order to understand and improve the cell operating conditions if possible. Thus, a good model for the cell microstructure is required. Different models exist based on different time and length scales. Examples are computational fluid dynamics (CFD), Monte Carlo method (MC), Lattice Boltzmann (LB) or coarse-grained molecular dynamics method (CG) among others.

Nevertheless, when modeling chemical reactions, other transport phenomena, like heat transfer, must be taken into account as chemical reactions are strictly bonded to heat transfer, being special contributors to the global energy balance of the fuel cell.

Heat transfer within the whole FC unit cell consists of convection and conduction. Convection occurs between the gas flow and the solid surfaces while conduction takes place in the solid and in the porous parts. Moreover, radiation also takes place for example, within the electrode-electrolyte structure, from the stack to the surrounding environment and surface to surface radiation in the air and fuel channels. Nevertheless, considering radiation in the model adds a higher degree of complexity to the governing equations [20]. However, radiation should be considered if a detailed model is required. Heat generation or consumption is also present. The general heat conduction equation is used to calculate the temperature distribution for the solid phase in the porous electrodes [21]:

$$\nabla \left(-k_s \cdot \nabla T_s \right) = Q_s \tag{2}$$

where Q_s is the heat source, such as the heat transfer between the gas and the solid phases, and the heat generation due to the ohmic polarization and the internal reforming reactions.
The temperature for the gas phase in the porous electrodes (also valid for the air and fuel channels) is governed by [21]:

$$\nabla \left(-k_g \cdot \nabla T_g \right) = Q_g - \rho_g c_{p,g} u \nabla T_g \tag{3}$$

where k_g is the gas thermal conductivity and Q_g is the heat transfer between the gas and the solid phases which is calculated as follows:

$$Q_g = -Q_s = h_v \left(T_g - T_s \right) = A v h_{s,g,por} \left(T_g - T_s \right) \tag{4}$$

The subscript s refers to solid, g to gas and por to porous. All previous equations are based on the local temperature non-equilibrium (LTNE) approach where the temperature from the gas- and solid-phases are not assumed to be locally the same as in the local temperature equilibrium (LTE)[22].

It is very important to know where exactly the heat sources in the fuel cell are generated or consumed when modeling at the microscale region (nm and a few μm) in order to obtain an accurate temperature profile in the fuel cell.

There are different mechanisms of heat generation or consumption taking place in an SOFC. Basically, all the heat sources within an SOFC are due to the electrochemical and chemical reactions in an SOFC. Thus, knowledge about these sources is of interest as it can provide information for the overall performance, possible mechanical stresses, etc. The mentioned heat sources will be described in the following sections.

4.1. Methane steam reforming and water-gas shift reforming reactions
SOFCs using methane as fuel need to undergo a reformation process of the fuel as methane cannot be directly used in the FCs. Thus, by reforming methane, carbon monoxide and hydrogen are produced which can now be directly used as fuel. The reforming process can be done internally or externally but SOFCs present the possibility to have internal reforming reaction of methane due to the high operating temperatures. The methane steam reforming (MSR) reaction, Eq. 1, is a highly endothermic reaction ($\Delta H_{1273K} = 227.6\,\text{kJ mol}^{-1}$) and thus, introduces a high sink of heat into the cell components involved in the process [23]. The steam reforming reaction of methane takes place in the anode of the fuel cell as it requires the Ni particles which act as catalysts of the reaction. Thus, the steam reforming reaction strictly takes place at the Ni particles' surface.

As the SR reaction is endothermic, the heat absorbed or consumed by the reaction in $\frac{\text{W}}{\text{m}^3}$ can be determined by the reaction rate and the enthalpy of reaction. Different expressions for the reaction rate can be found in Table 2.

$$Q_{MSR}^{'''} = r_{MSR} \Delta H_{MSR} A v^{an} \tag{5}$$

Anyhow, the SR reaction of methane is accompanied by the water-gas shift (WGS) reaction. The WGS is slightly exothermic ($\Delta H_{1273K} = -31.8\,\mathrm{kJ\,mol^{-1}}$) and it is usually assumed to be in equilibrium as it is a much faster reaction than the SR reaction [17, 23–26].

$$CO + H_2O \rightleftharpoons CO_2 + H_2 \tag{6}$$

The heat generated by the WGS reaction can be expressed as follows.

$$Q'''_{WGS} = r_{WGS}\Delta H_{WGS}Av^{an} \tag{7}$$

The equilibrium approach can be modeled as [25].

$$r_{WGS} = k_{WGS}P_{CO}\left(1 - \frac{P_{CO_2}P_{H_2}}{K_{e,WGS}P_{CO}P_{H_2O}}\right) \tag{8}$$

$$K_{e,WGS} = \exp\left(\frac{4276}{T} - 3.961\right) \tag{9}$$

where k_{WGS} is the reaction rate constant and can be calculated according to Haberman and Young [25] and $K_{e,WGS}$ is the equilibrium constant for the WGS reaction.

4.2. Entropy changes due to the electrochemical reactions
The oxidation of hydrogen is the driving reaction of the energy conversion in an SOFC device. This process can be written as a general reaction as follows:

$$H_2 + \frac{1}{2}O_2 \rightleftharpoons H_2O \tag{10}$$

Nevertheless, this general electrochemical reaction consists of two semi-reactions that take place in different parts of the fuel cell. The reduction of oxygen, Eq. 11, takes place in the active layer of the triple-phase boundaries (TPBs) of the cathode while the oxidation of hydrogen, Eq. 12, takes place at the anodic TPBs.

$$\frac{1}{2}O_2 + 2e^- \rightarrow O^{2-} \tag{11}$$

$$H_2 + O^{2-} \rightarrow H_2O + 2e^- \tag{12}$$

Although the global electrochemical reaction is highly exothermic ($\Delta H_{1273K} = -250\,\mathrm{kJ\,mol^{-1}}$), only a part can be converted into electric work. The maximum work that can be obtained is given by the Gibbs free energy (ΔG).

$$\Delta G_{ER} = \Delta H_{ER} - T\Delta S_{ER} \tag{13}$$

where the subscript ER refers to electrochemical reaction and the term $(-T\Delta S_{ER})$ is the change of entropy released as heat due to the electrochemical reaction.

Despite the fact that most models assume that the heat associated with the general electrochemical reaction is assigned to the anodic TPB, this heat is generated at the two different electrodes and in different amounts. Therefore, if a detailed model is desired, one should take into account the entropy changes for each semi-reaction and thus, calculate the heat generation due to the electrochemical reaction for each electrode as follows. However, one must consider the reaction sites as infinitely thin layers and thus, the released heat per unit volume $\left[\frac{W}{m^3}\right]$, by considering TPBs reaction area, can be calculated [23].

$$Q'''^{an,cat}_{ER} = \frac{j}{2F}\left(-T\Delta S^{an,cat}_{ER}\right)Av^{an,cat} \tag{14}$$

where j is the local current density. Moreover, Fischer et al. [23] showed that the amounts of heat released or absorbed by the semi-reactions are the most important sources or sinks of heat in the fuel cell.

4.3. Concentration polarizations

Concentration polarizations are those polarizations associated with the variation of concentration of the critical species due to mass transfer processes. There are basically two main sources due to mass transport: transport of reactants and products through the electrodes and diffusion between the bulk flows and cell surfaces. Thus, concentration polarizations are highly dependent on the diffusion length, the pore volume percentage of the components as well as the gases involved [27]. Therefore, these concentration polarizations give a surplus heat at the anodic and cathodic reaction sites which can be calculated as follows [23].

$$Q_{conc}'''^{an,cat} = j\eta_{conc}^{an,cat} Av^{an,cat} \tag{15}$$

4.4. Activation polarizations

The activation polarizations can be considered as the extra potential needed in order to overcome the activation energy (E_A) or energy barrier of the rate-determining step to a value that the reaction proceeds at a desired rate [22, 27]. The activation polarizations are described by the Butler-Volmer equation [22, 23, 27].

$$j = j_0 \left[\exp\left(\alpha \frac{n_e F \eta_{act}^{an,cat}}{RT} \right) - \exp\left(-(1-\alpha) \frac{n_e F \eta_{act}^{an,cat}}{RT} \right) \right] \tag{16}$$

where n_e is the number of electrons participating in the reaction, α the charge transfer coefficient, usually assumed to be 0.5 in FCs and j_0 the exchange current density.

The heat generated by these irreversible polarizations is released at the anodic and cathodic catalyst particle surfaces. Thus, the heat source will be $\left[\frac{W}{m^3}\right]$ [23].

$$Q_{act}'''^{an,cat} = j\eta_{act}^{an,cat} Av^{an,cat} \tag{17}$$

4.5. Ohmic polarizations

The ohmic polarizations are due to the joule heating effect or, in other words, they are due to the resistance to ion transfer through the electrolyte (YSZ), electron transfer through the electrodes (Ni or strontium doped lanthanum manganate, LSM) and current collectors and also by the contact resistance between the different cell components. Thus, they are characteristic for the solid parts of the FC and they lead to a release of heat which can be determined by the local current density and the material conductivity [22, 23, 27].

$$Q_{\Omega}''' = \frac{1}{\sigma} j^2 \tag{18}$$

where Q_{Ω}''' is the local heat source $\left[\frac{W}{m^3}\right]$.

4.6. Comparison of different heat sources

In Table 2, the different kinds of heat generation or consumption within SOFCs are summarized. Moreover, in the last column, the percentage contributed by each one in absolute values is shown. The sum of all contributions adds up to 100 %. These values are estimated for the model used by Andersson et al. [28], in which reforming reactions take place through the whole cell operating a 30% pre-reformed natural gas as fuel.

The results show that the main contribution to heat generation or consumption is by the electrochemical reactions. It must be pointed out that this is the net contribution from both semi-reactions, that is why it is considered as a heat source (positive values) because, as mentioned previously, the different semi-reactions take place at different electrodes (one being endothermic and the other exothermic). Nevertheless, still electrochemical reactions are the main contributors. The second most important is the methane steam reforming reaction, which

is the heat sink of the SOFC as it is a strong endothermic reaction. Thus, as electrochemical and reforming reactions are the main contributors, it is reasonable that the major concerns of nowadays technology are that the SR reaction is much faster than the electrochemical reaction and the need of lowering the SR reaction rate. Activation polarizations are quite significant as they are directly related to the chemical reactions. The contribution from the WGS reaction and the ohmic polarizations are quite similar while the contribution from the concentration polarizations is less than 1%.

Table 2. Mechanisms and relative contribution of specific reaction to the total heat (source or sink) in SOFCs

Mechanism	Symbol	Location	Expression	Heat source/sink	% Relative contribution
MSR reaction	Q_{MSR}'''	anodic active layer	$r_{MRS}\Delta H_{MSR}Av^{an}$	sink	27
WGS reaction	Q_{WGS}'''	anodic active layer	$r_{WGS}\Delta H_{WGS}Av^{an}$	source	6
Electrochemical reaction	$Q_{ER}'''^{an,cat}$	active layer electrodes' TPBs	$\frac{j}{2F}\left(-T\Delta S_{ER}^{an,cat}\right)Av^{an,cat}$	source	47
Concentration polarizations	$Q_{conc}'''^{an,cat}$	electrodes' reaction sites	$j\eta_{conc}^{an,cat}Av^{an,cat}$	source	< 1
Activation polarizations	$Q_{act}'''^{an,cat}$	electrodes' reaction sites	$j\eta_{act}^{an,cat}Av^{an,cat}$	source	16
Ohmic polarizations	Q_{Ω}'''	solid cell components	$\frac{j^2}{\sigma}$	source	3

5. Conclusions

The research done lately in the FC field has allowed a decrease in the operating temperature of SOFCs. This has resulted in a big gain for SOFCs as internal reforming of natural gas is possible, cheaper materials can be used for the FC and also higher stability of the overall fuel stack. This is indeed an important path for improving SOFC performance to increase the future potential market.

Special attention has been given to the kinetics of the internal reforming reaction as it is believed to be one of the main issues for improving the SOFC performance. Different kinetic expressions based on the overall reaction schemes have been found in the literature for SR in Ni-YSZ catalysts on SOFC anodes. However, these expressions differ ones from each other making comparison difficult as the conditions they are derived from are also different.

Moreover, the different heat sources that take place within an SOFC have been described together with the place at which they are located as well as their relationship with the chemical and electrochemical reactions in an SOFC. From the different heat sources, the heat originated or consumed due to the electrochemical reactions at the two electrodes is the main contributor followed by the steam reforming reaction.

In order to perform a detailed simulation of an SOFC, heat transfer phenomena must be taken into account as well as a detailed reaction mechanism for each reaction. If a detailed heat transfer analysis is implemented, with special details on where the heat sources are located, detailed reaction mechanisms for the different chemical reactions are also required. This means modeling probably at nanometer scales and the computational cost may be increased. However, it is a good chance for obtaining a detailed model of the chemistry and temperature distribution so that the SOFC performance can be further improved.

Nomenclature

Av	Active surface area to volume ratio, $\left[\mathrm{m^2\,m^{-3}}\right]$	
C_p	Specific heat at constant pressure, $\left[\mathrm{kJ\,kg^{-1}K^{-1}}\right]$	
E_A	Activation energy, $\left[\mathrm{kJ\,mol^{-1}}\right]$	
F	Faraday constant, $\left[\mathrm{sA\,mol^{-1}}\right]$	
ΔG	Gibbs free energy of reaction, $\left[\mathrm{kJ\,mol^{-1}}\right]$	
h	Heat transfer coefficient, $\left[\mathrm{W\,m^{-2}K^{-1}}\right]$	
ΔH	Enthalpy change of reaction, $\left[\mathrm{kJ\,mol^{-1}}\right]$	
j	Current density, $\left[\mathrm{A\,m^{-2}}\right]$	
k	Thermal conductivity, $\left[\mathrm{W\,m^{-1}K^{-1}}\right]$	
k_i	Reaction rate constant, $\left[\mathrm{mol\,m^{-3}Pa^{-2}s^{-1}}\right]$	
K_e	Equilibrium constant, dimensionless	
n_e	Number of electrons, dimensionless	
P_i	Partial pressure, [bar] or [Pa]	
Q	Heat flow, [W]	
r	Reaction rate, mainly $\left[\mathrm{mol\,m^{-2}s^{-1}}\right]$	
R	Gas constant, $\left[\mathrm{J\,mol^{-1}K^{-1}}\right]$	
ΔS	Entropy of reaction, $\left[\mathrm{J\,mol^{-1}K^{-1}}\right]$	
T	Temperature, [°C] or [K]	
u	Velocity vector, $\left[\mathrm{m\,s^{-1}}\right]$	

Greek symbols

α	Charge transfer coefficient, dimensionless
η	Voltage loss, [V]
ρ	Density, $\left[\mathrm{kg\,m^{-3}}\right]$
σ	conductivity, $\left[\mathrm{S\,m^{-1}}\right]$

Superscripts

an	Anode
cat	Cathode
0	Standard conditions
$'''$	per unit volume

Subscripts

act	Activation polarizations
$conc$	Concentration polarizations
ER	Electrochemical reaction
g	Gas
i	Gas species
por	Porous
Ω	Ohmic
0	Standard conditions

References

[1] Kawamoto H 2008 *Sci. Technol. Trends* **47** 52–70

[2] Nielsen J, Jacobsen T and Wandel M 2011 *Electrochim. Acta* **56** 7963–7974

[3] Services E T 2004 *Fuel Cell Handbook* 7th ed (U.S. Dep. Energy Office of Fossil Energy Nat. Energy Technol. Lab.)

[4] Mogensen D, Grunwaldt J D, Hendriksen P V, Dam-Johansen K and Nielsen J U 2011 *J. Power Sources* **196** 25–38

[5] Andersson M, Paradis H, Yuan J and Sundén B 2011 *Int. J. Energ. Res.* **35** 1340–1350

[6] Zhu B 2006 *Int. J. Energ. Res.* **30** 895–903

[7] Bebelis Zeritis T N 2000 *Ind. Eng. Chem. Res.* **39** 7

[8] Simwonis D, Tietz F and Stöver D 2000 *Solid State Ionics* **132** 241–251

[9] Liu L, Flesner R, Kim G Y and Chandra A 2012 *Fuel Cells* **12** 97–108

[10] Ni M, Leung M K H and Leung D Y C 2007 *Chem. Eng. Technol.* **30** 587–592

[11] Achenbach E and Riensche E 1994 *J. Power Sources* **52** 283–288

[12] Leinfelder R 2004 *Reaktionskinetische untersuchung zur methan-damp-reformierung und shift-reaktion an anoden oxidkeramischer brenstoffzellen* Doctoral dissertation, Der Technischen Fakultät der Universität Erlangen-Nürenberg

[13] Ahmed K and Foger K 2000 *Catal. Today* **63** 479–487

[14] Yakabe H, Ogiwara T, Hishinuma M and Yasuda I 2001 *J. Power Sources* **102** 144–154

[15] Boder M and Dittmeyer R 2006 *J. Power Sources* **155** 13–22

[16] Peters R, Dahl R, Klüttgen U, Palm C and Stolten D 2002 *J. Power Sources* **106** 238–244

[17] Lehnert W, Meusinger J and Thom F 2000 *J. Power Sources* **87** 57–63

[18] Drescher I, Lehnert W and Meusinger J 1998 *Electrochim. Acta* **43** 3059–3068

[19] Drescher I 1999 *Kinetik der Methan-Dampf-Reformerung* Doctoral dissertation, Forschungszentrums Jülich

[20] Damm D L and Fedorov A G 2005 *J. Power Sources* **143** 158–165

[21] Sohn S, Nam J H, Jeon D H and Kim C J 2010 *Int. J. Hydrogen Energ.* **35** 11890–11907

[22] Andersson M 2011 *Solid Oxide Fuel Cell Modeling at the Cell Scale Focusing on Species, Heat, Charge and Momentum Transport as well as the Reaction Kinetics and Effects* Doctoral dissertation, Lund University

[23] Fischer K and Seume J R 2009 *J. Fuel Cell Sci. Technol.* **6** 011002

[24] Klein J M, Bultel Y, Georges S and Pons M 2007 *Chem. Eng. Sci.* **62** 1636–1649

[25] Haberman B A and Young J B 2004 *Int. J. Heat Mass Transfer* **47** 3617–3629

[26] Aguiar P, Adjiman C S and Brandon N P 2004 *J. Power Sources* **138** 120–136

[27] Hajimolana S A, Hussain M A, Daud W M A W, Soroush M and Shamiri A 2011 *Renew. Sust. Energ. Rev.* **15** 1893–1917

[28] Andersson M, Yuan J and Sundén B 2012 *International Journal of Heat and Mass Transfer* **55** 773–788

Paper II
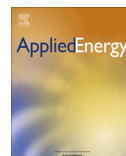
Computational fluid dynamics approach for performance evaluation of a solid oxide electrolysis cell for hydrogen production

Maria Navasa *, Jinliang Yuan, Bengt Sundén

Division of Heat Transfer, Department of Energy Sciences, Lund University, P.O. Box 118, SE-221 00 Lund, Sweden

HIGHLIGHTS

- A three-dimensional FVM based CFD model for a cathode-supported SOEC is developed.
- The effect of different operating voltages on cell performance is investigated and analyzed.
- Cross-flow and parallel-flow configurations are compared and differences are identified.

ARTICLE INFO

ABSTRACT

A finite volume method based computational fluid dynamics model has been developed and applied for a cathode-supported planar solid oxide electrolysis cell (SOEC) operating in cross-flow configuration arrangement. The performance behavior, in terms of current density, temperature distribution and hydrogen production in an SOEC, has been investigated for different operating voltages and compared with a corresponding parallel-flow configuration. The predicted results show that higher current densities are obtained for higher operating voltages. The anodic current density is higher than the cathodic one. Yet, the parallel-flow configuration yields lower current density values although they remain in the same order of magnitude as those from the cross-flow arrangement. The simulation reveals various temperature profiles depending on the operating voltage emphasizing the three thermal operating modes of an SOEC, i.e., endothermic, thermo-neutral and exothermic. Per contra, the parallel-flow arrangement gives a temperature decrease along the flow direction although operating in exothermic mode. Higher hydrogen molar fractions at the outlet of the cathode channel were obtained at higher operating voltages due to the higher current densities generated and the exothermic operating mode. The parallel-flow arrangement yields lower hydrogen production due to the lower current densities revealed.

© 2014 Elsevier Ltd. All rights reserved.

1. Introduction

Hydrogen, an ideal energy carrier, is considered to be an encouraging fuel candidate for improving the usage of renewable energy sources. Due to the increasing interest of hydrogen as a fuel, industry and governmental institutions are putting more effort to develop hydrogen-related technologies [1]. Despite the fact that nowadays the main hydrogen source is hydrocarbon reforming, hydrogen can also be obtained through green energy procedures such as water splitting (electrolysis, photolysis or thermochemical water splitting) and biomass [2–5]. At present, water electrolysis is the most viable process for hydrogen production at large scales and consists of splitting water into hydrogen and oxygen by applying electrical energy [2]. The thermal energy required for electrolysis increases with temperature while the required electrical energy decreases. Thus, high-temperature electrolysis might be a really interesting process to consider when waste heat from other processes is available [1,2]. Actually, electrolyzer cells can use the waste heat from industry and the electricity obtained from solar cells or wind turbines. Moreover, there is growing interest in integrating electrolysis cells together with nuclear energy to improve the hydrogen production efficiency [6,7].

However, the production of hydrogen via water electrolysis, especially via solid oxide electrolysis cells (SOECs), is strongly dependent upon two main factors. The first refers to the restriction of the consumption of fossil fuels, mainly by political reasons, which will lead to an increase of energy supply from renewable energy sources and a consequent increasing interest in hydrogen related energy technologies. The second factor is if the energy price for energy from non-fossil fuels sources, i.e., solar or wind energy, is lower than that of the energy from fossil fuels. Regarding the

* Corresponding author. Tel.: +46 462228610.
E-mail address: Maria.Navasa@energy.lth.se (M. Navasa).

Nomenclature

c_p	specific heat at constant pressure [J kg^{-1} K^{-1}]		ρ	density [kg m^{-3}]
D_m	mass diffusion coefficient [m^2 s^{-1}]		σ	electric conductivity [S m^{-1}]
D_T	thermal diffusion coefficient [kg m^{-1} s^{-1}]		Φ	potential [V]
F	Faraday constant [C mol^{-1}]			
i_0	exchange current density [A m^{-2}]		*Subscripts and superscripts*	
$\mathbf{J}$	mass diffusion flux [kg m^{-2} s^{-1}]		*act*	activation
j	volumetric current density [A m^{-3}]		*an*	anode
K	permeability [m^2]		*cat*	cathode
k	thermal conductivity [W m^{-1} K^{-1}]		*i*	gas species i
N	number of species i in the gas mixture, dimensionless		*j*	gas species j
n_e	number of electrons transferred per reaction, dimensionless		Ω	ohmic
P	pressure [Pa]		*Abbreviations*	
S	entropy [kJ mol^{-1} K^{-1}]		**CFD**	computational fluid dynamics
S_d	source term for the momentum conservation equation [W m^{-3}]		**FVM**	finite volume method
S_m	source term for the mass conservation equation [kg m^{-3} s^{-1}]		**HTE**	high-temperature electrolysis
			SOEC	solid oxide electrolysis cell
S_T	source term for the energy conservation equation [W m^{-3}]		**SOFC**	solid oxide fuel cell
			TPB	triple-phase boundary
S_Φ	source term for the charge transfer equation [A m^{-3}]			
T	temperature [K]		*Chemical species compounds*	
$\mathbf{U}$	velocity vector [m s^{-1}]		CH$_4$	methane
V	voltage [V]		CO	carbon monoxide
Y_i	molar fraction of species i, dimensionless		CO$_2$	carbon dioxide
			e$^-$	electron
Greek letters			H$_2$	hydrogen
η	polarizations [V]		H$_2$O	water
μ	dynamic viscosity [Pa s]		O$_2$	oxygen
			O^{2-}	oxide ion

second condition, the production cost of hydrogen and syngas will define the potential and viability of SOECs. The production cost of hydrogen and syngas by SOECs is mainly defined by the following parameters: the electricity price and the cell specifications and requirements (costs of cells and stacks, performance and durability of the device) [8]. The main part of the production cost of hydrogen and syngas is the electricity cost [2,9]. At higher operating temperatures, less electricity is required compared to low-temperature processes which can help to decrease the electricity cost. Nevertheless, if electricity at lower prices can be obtained from renewable energy sources, the production price can be lowered. Another factor that can even lower more the production price if operating at high temperatures is using the waste heat from other processes, as previously mentioned, as heat for steam generation. From a global perspective, most of the electricity produced nowadays is by fossil energy sources with relatively low efficiency compared to some renewable energy sources. For example, a SOEC operating in reversed mode, as a fuel cell, has an efficiency for electricity production of 60% compared to a 30–40% provided by conventional gas turbine power plants [9]. Another advantage that SOECs present in comparison with other electrochemical processes or hydrogen production methods is that it can be used as a device for recycling or reusing carbon dioxide from other energy systems or as a CO$_2$ capture device, i.e., a possibility for CO$_2$ storage. Although the materials are relatively expensive for the cell production, research in this area is moving forward but a major concern is how to improve the performance and durability of the cell.

High-temperature electrolysis (HTE) of water takes place at high temperatures (700–1000 °C) and its technology is based on the high-temperature fuel cells, especially solid oxide fuel cells (SOFCs). Thus, one of the most typical devices for HTE is the solid oxide electrolysis cell (SOEC), see Fig. 1. SOECs are usually understood as SOFCs operating in reversed mode. Steam is fed into the electrolysis cell where water splitting takes place giving hydrogen and oxygen as products, as shown in Eq. (1). Thus, an SOEC is comprised of the same components as an SOFC: fuel and air channels and two electrodes (anode and cathode) separated by an electrolyte. However, it seems that the transport characteristics in SOECs differ considerably from SOFCs, especially related to kinetic reactions, and thus, results from SOFCs cannot be directly applied to SOECs, emphasizing the significant need for SOEC modeling as relatively little has been done in this field [10,11].

$$H_2O_{(g)} \rightleftharpoons H_{2(g)} + O_{2(g)} \qquad (1)$$

2. Problem statement

Water steam is fed into the fuel channels on the cathode side. The water molecules diffuse through the porous cathode structure (the cathode diffusion layer in Fig. 2) to the triple phase boundary (TPB) at the cathode-electrolyte interface (the cathode TPB layer in Fig. 2) where they react with the electrons supplied by an external source to produce hydrogen gas and oxygen ions, Eq. (2). The oxide ions (O^{2-}) are transported through the electrolyte to the TPB at the anode-electrolyte interface (the anode TPB layer in Fig. 2) where the oxide ions are oxidized to oxygen gas, as shown in Eq. (3). The oxygen gas molecules produced diffuse through the porous anode structure (the anode diffusion layer in Fig. 2) to the outlet at the air channel.
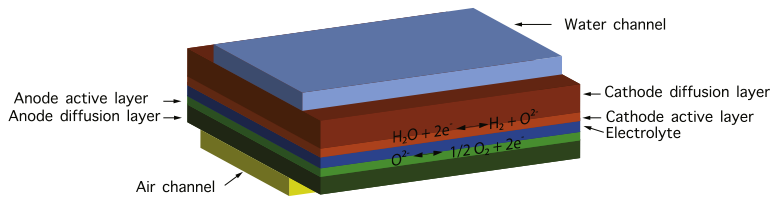
$$H_2O_{(g)} + 2e^- \rightleftharpoons H_{2(g)} + O^{2-} \qquad (2)$$

$$O^{2-} \rightleftharpoons 1/2 O_{2(g)} + 2e^- \qquad (3)$$

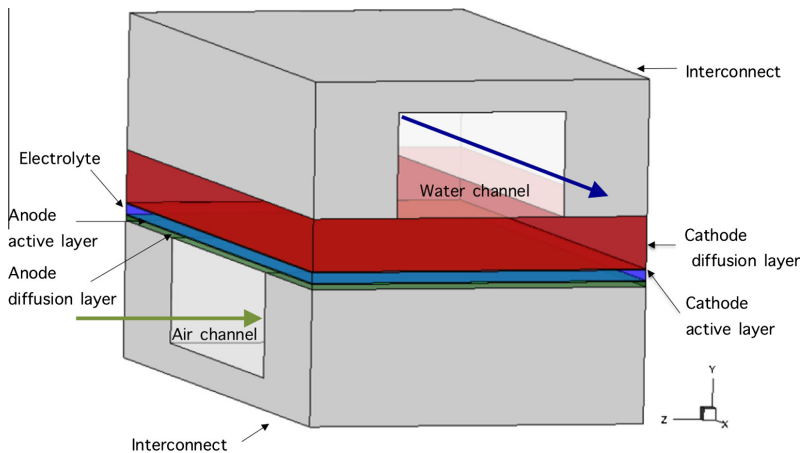**Fig. 1.** Schematic image of an SOEC with open view of interconnects.

Fig. 2. The computational domain for a unit planar SOEC (not to scale). Cell dimensions are stated in Table 1.

Nevertheless, mass diffusion is not the only transport phenomenon that takes place through the porous layers of the SOEC. An SOEC is known to be a complex device as many different transport phenomena occur simultaneously, i.e., mass convection in the gas channels, mass diffusion in the porous layers, transport of ions and electrons due to electrochemical reactions, heat generation or consumption, etc. The wide variety of transport phenomena that describes the behavior of an SOEC remarks the complexity of the system. Thus, in order to improve the efficiency of the device and the hydrogen production efficiency in general terms, numerical simulations are required to study the interactions of these phenomena and their effects on the overall performance. Although SOECs are not new devices, few modeling and simulation works have been done compared to SOFCs. Several models can be found in the literature from different research groups. Most of the models reported so far are based on 1D mathematical models [12–15] or 1D/2D computational fluid dynamics (CFD) simulations on a unit cell or a stack of planar SOECs [1,10,16–20] and just a few refer to 3D with some limitations [7,21–24]. Some models from the literature are briefly discussed.

The first 3D model was reported by Hawkes et al. [21] and O'Brien et al. [7,22,23]. Hawkes et al. presented 3D CFD cell stack models by using the commercial software ANSYS FLUENT. All their models include mass, momentum, energy and species conservation equations. The electrochemical reactions are implemented as well. The geometry of the electrolyte is simplified by treating the electrolyte as a 2D component, resulting in a zero thickness electrolyte (eliminating the transport processes in the thickness or cell height direction). Ni et al. [1,16,17] have also developed a couple of CFD models of SOECs. The effects of the inlet velocity as well as the electrode porosity were studied under different operating potentials for a 2D model (along the main flow and cell height directions) operating under parallel-flow configuration. The governing equations for momentum, mass, heat and species were discretized by the Finite Volume Method (FVM) and solved by an in-house code [1]. A mathematical model of the coupled transport phenomenon (mass transfer only) and the electrochemical reactions at microscale level has also been developed by Ni et al. [17] to study the effect of the gas transport on the concentration polarizations. Other one-dimensional mathematical models along the main flow direction can be found in the literature. Udagawa et al. [12–14] developed a mathematical model considering the electrochemical reactions, mass and heat transfer for a cathode-supported planar SOEC stack for steady and unsteady state. The effects of the current densities, the temperature under exothermic and endothermic operations as well as the air flow on the stack temperature were studied. Regarding CFD simulations, 2D models are the most reported ones in the literature. Grondin et al. [18] conducted a simulation of a single circular SOEC considering only charge, mass and heat transfer. The authors pointed out that the mechanism of water steam reduction on Ni–YSZ is not clearly identified for YSZ. Moreover, they showed that the temperature distribution depends on the gas feeding configuration under the three thermal operating modes (endothermal, exothermal and thermoneutral) of SOECs. Jin and Xue [19] developed a more complete 2D planar SOEC model considering the coupled processes of charge balance, electrochemical reaction kinetics, mass, momentum and energy balances to perform an analysis of the SOEC performance affected by the size and position of delaminations at the electrode/electrolyte interface.

Further, most of the models are based on the reversed SOFC operation mode concept to describe an SOEC which seems not to be the most optimal, especially for kinetic reactions related models. Hence, the need for 3D models that are able to capture the coupling between the different transport phenomena and the electrochemical reactions in an SOEC is more than necessary in order to understand SOEC performance in relation to the material properties, cell design parameters as well as operating conditions. Special emphasis on the electrochemistry concerning the electrochemical reactions should be made.

Despite the limited number of complete CFD models available, considering both 2D and 3D, one of the current trends in the SOEC field is to consider the electrolysis of carbon dioxide; probably due to environmental considerations as it can be used as a method for carbon adsorption [25–28].

3. Modeling description

The 3D geometry of a planar SOEC shown in Fig. 2 is used to study the performance of such devices by using ANSYS FLUENT. The modeling domain consists of a single cell which operates in cross-flow, i.e., the steam/hydrogen flow direction is perpendicular to the oxygen flow direction.

3.1. Cell geometry

A sketch of the cell geometry to be modeled can be found in Fig. 2. Note that the sketch is not to scale. In Table 1, the different parameters used in the calculation as well as the dimensions of the different components of the cell can be found. The modeling domain used for the calculations consists of two gas channels: one for the water/hydrogen at the cathode side and another one for the air at the anode side. Connected to the each channel, the diffusion layer is located followed by TPB layer where the electrochemical reactions take place, namely Eq. (2) at the cathodic TPB and Eq. (3) at the anodic TPB. The component that separates the two TPBs is the electrolyte layer, i.e., the region through which the oxide ions are transported. Interconnects for both sides are also considered in the computational domain.

3.2. Governing equations for transport processes in SOECs

A 3D (CFD) model is developed and implemented using the commercial software ANSYS FLUENT 14.5 with its fuel cell and electrolysis add-on module to simulate a single electrolysis cell as it would exist in the interior of a multiple cell stack. FLUENT

Table 1
Parameters used in simulation.

Parameter	Value	Units
Operating temperature	1073	K
Operating pressure	1	bar
Length and width	0.2	m
Cathode diffusion layer thickness	$5 \cdot 10^{-4}$	m
Cathode TPB layer thickness	$1 \cdot 10^{-5}$	m
Electrolyte thickness	$1 \cdot 10^{-4}$	m
Anode TPB layer thickness	$1 \cdot 10^{-5}$	m
Anode diffusion layer thickness	$5 \cdot 10^{-5}$	m
Gas channel height	$1 \cdot 10^{-3}$	m
Gas channel width	0.1	m
Open circuit voltage (OCV)	0.84	V
Cathode exchange current density	7500	A m^{-2}
Anode exchange current density	2000	A m^{-2}
Active surface area-to-volume ratio in TPBs	$2 \cdot 10^{5}$	m^{-1}
Permeability	$1 \cdot 10^{-12}$	m^{2}

is based on the Finite Volume Method (FVM) and thus, for each computational domain, the governing equations stated in Table 2 are solved. Moreover, the different source terms for each cell component are specified. When the equations are solved for the porous sub-domains, the effective values of the transport properties, such as the thermal conductivity, density, dynamic viscosity and the specific heat, are considered. The values used for the density, specific heat, thermal conductivity and charge transfer conductivity are independent of the temperature, as pre-defined by the FLUENT fuel cell and electrolysis add-on module [29]. Similar values can be found in the literature [1,7,17,22]. The major simplification done by this module is considering the same material for both electrodes. These limitations will be released in the future work using different electrode materials, temperature dependent thermophysical properties and reaction kinetics.

Apart from the governing equations stated in Table 2, the current conservation equation, Eq. (4), is also considered in the model's system of equations.

$$\int_{anode} j_{an}\, dV = \int_{cathode} j_{cat}\, dV \tag{4}$$

where j is the volumetric current density, [A m^{-3}].

It should be noted that the species transport equation in Table 2 is solved for H_2 and H_2O at the fuel side and for O_2 at the air side. N_2 is not included as it does not undergo the electrochemical reactions specified above. The mass diffusion flux from the species equation, $\mathbf{J}_i$, is calculated by Ficks law Eq. (5) taking into account the Soret effect.

$$\mathbf{J}_i = -\rho D_{m,i}^{eff} \nabla Y_i - D_{T,i}\frac{\nabla T}{T} \tag{5}$$

where $D_{m,i}^{eff}$ is the effective mass diffusion coefficient of component i in the gas mixture and $D_{T,i}$ is the thermal diffusion coefficient of component i in the gas mixture as well.

Fick's law is the simplest diffusion model and it is only valid for a binary mixture, for a multicomponent mixture with invariable composition, dilute mixtures or when the mass diffusion coefficient is independent of composition. As an SOEC operates under a mixture of four different gas species with variable composition, the Stefan–Maxwell equations should be used.

By the assumption that for ideal gases the Maxwell diffusion coefficients can be approximated by the binary diffusion coefficients, the external force is assumed equal on all species and by neglecting pressure diffusion, the Stefan–Maxwell equations can be written as [30]:

$$\sum_{j=1,j\neq i}^{N} \frac{Y_i Y_j}{D_{ij}}\left(\frac{\mathbf{J}_i}{\rho_i} - \frac{\mathbf{J}_j}{\rho_j}\right) = \nabla Y_i - \frac{\nabla T}{T}\sum_{j=1,j\neq i}^{N} \frac{Y_i Y_j}{D_{ij}}\left(\frac{D_{T,j}}{\rho_j} - \frac{D_{T,i}}{\rho_i}\right) \tag{6}$$

where D_{ij} is the binary diffusion coefficient which can be evaluated by the kinetic theory of gases applying the Chapman–Enskog theory [31].

3.3. Boundary conditions

The major boundary conditions applied in the SOEC computational model are specified in Table 3. The operating voltage (V) and the inlet molar fractions for the water mixture species, water and hydrogen, are specified in Table 4 according to the different simulation cases.

3.4. Solution methods

The semi-implicit method for pressure-linked equations (SIMPLE) has been used for the pressure–velocity coupling. The first-order discretization scheme has been employed for the convection

Table 2
Governing equations and corresponding source terms.

Governing equation	Source term		
Continuity equation	Except TPBs		TPBs
$\nabla \cdot (\rho \mathbf{U}) = S_m$	$S_m = 0$		$S_m = \sum_i S_{m,i}$
Momentum equation	Channels		TPBs and diffusion layers
$\nabla \cdot (\rho \mathbf{UU}) = -\nabla P + \nabla \cdot (\mu \nabla \mathbf{U}) + S_d$	$S_d = 0$		$S_d = -\frac{\mu}{K}\mathbf{U}$
Energy equation	Diffusion layer, electrode, interconnects		TPBs
$\nabla \cdot (\rho C_p \mathbf{U} T) = \nabla \cdot (k \nabla T) + S_T$	$S_T = \frac{i^2}{\sigma}$		$\frac{i^2}{\sigma} + j(\eta_{act} + \frac{T \Delta S}{2F})$
Species equation	Except TPBs		TPBs
$\nabla \cdot (\rho \mathbf{U} Y_i) = -\nabla \cdot \mathbf{J}_i + S_{m,i}$	$S_{m,i} = 0$		$S_{m,i} = \frac{j}{n_e F} M_i$
Charge transport	Except TPBs		TPBs
$-\nabla \cdot (\sigma \nabla \Phi) = S_\Phi$	$S_\Phi = 0$		$S_\Phi = j$

Table 3
Major boundary conditions.

Variable	Top wall	Bottom wall	Side walls	
			Inlet	Outlet
$\mathbf{U}$	$\mathbf{U} = 0$	$\mathbf{U} = 0$	$\dot{m}_{H_2O/H_2} = 1.61 \cdot 10^{-5}$ kg s^{-1}	$\frac{d\mathbf{U}}{dx} = 0 \, \frac{d\mathbf{U}}{dz} = 0$
			$\dot{m}_{O_2/N_2} = 8.66 \cdot 10^{-6}$ kg s^{-1}	
T	$\frac{dT}{dy} = 0$	$\frac{dT}{dy} = 0$	$T_{H_2O/H_2} = 1073$ K	
			$T_{O_2/N_2} = 1073$ K	
Y_i			Y_{H_2O}, Y_{H_2}	$\frac{dY_i}{dx} = 0 \, \frac{dY_i}{dz} = 0$
			$Y_{N_2} = 1, Y_{O_2} = 0$	
Ions	Insulation	Insulation	Insulation	Insulation
Electrons	0 [V]	V [V]	Insulation	Insulation

Table 4
Simulation cases investigated.

Case no.	V [V]	ε_{TPBs}	$\varepsilon_{diffusion}$	Y_{H_2O}	Y_{H_2}	Flow configuration
1	1.1	0.5	0.5	1	0	Cross-flow
2	1.2867	0.5	0.5	1	0	Cross-flow
3	**1.3**	**0.5**	**0.5**	**1**	**0**	**Cross-flow**
4	1.5	0.5	0.5	1	0	Cross-flow
5	1.3	0.5	0.5	1	0	Parallel-flow

term of all equations except for pressure where the standard scheme has been used. For the diffusive fluxes, the Green–Gauss cell based method has been applied.

Furthermore, all the residuals have been set to an absolute convergence criterion of 10^{-4} except for the energy equation, which has been set to 10^{-7}. A stabilization method based on the F-cycle with the bi-conjugate stabilized method (BCGSTAB) has been chosen for the species and the potential equations to avoid convergence problems. Pressure is stabilized by the V-cycle while the other governing equations are specified with the flexible cycle [29].

3.5. Parameter study

A parameter study has been performed to investigate the effects of different specifications on the cell performance. The effects of the operating voltage and flow configuration have been studied on the temperature distribution in the cell, on the current density and on the hydrogen molar fraction.

Four different operating voltages have been considered to investigate the behavior of the electrolysis in the endothermic, exothermic and thermo-neutral operation modes. All the different set-ups for the different cases have been summarized in Table 4. The voltage 1.2867 V (case No. 2) is the thermo-neutral voltage at 800 °C. The voltage 1.3 V (case No. 3) has been chosen for the base case and it is highlighted in bold in Table 4.

Despite that cross-flow configuration of the flow paths has been the conventional scheme for SOECs, and also for SOFCs, due to simplicity of separating the product streams in a cell stack [24], a parallel-, co-flow configuration has also been considered to study the effects of this flow configuration on the cell performance. The results from the parallel-flow configuration, case No. 5 in Table 4, are compared to those from the base case, case No. 3.

3.6. Validation analysis

The CFD model presented in the study was validated by comparing temperature values predicted as a function of the operating voltage to the data available in the literature. Fig. 3 shows the minimum and maximum cell temperature values for different
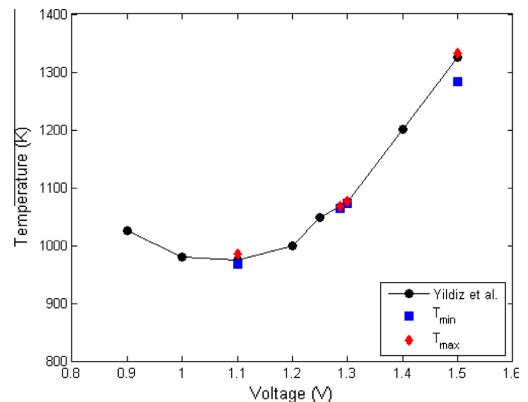

Fig. 3. Comparison of the predicted maximum and minimum temperatures with literature reported values for different operating voltages.

operating voltages compared to the average cell values reported by Yildiz et al. [24].

As it can be seen in Fig. 3, the results obtained from the current CFD model show a very good agreement with the ones divulged by Yildiz et al. for the temperature values despite the differences between the models. The average temperature as a function of the operating voltage verifies a good agreement, at least for this parameter.

A hexahedral mesh type arrangement has been used in order to perform the CFD calculations on the SOEC. A mesh independence study was performed on three different mesh sizes. The results from the mesh independence study show that although the current density distribution is almost invariable with the mesh size, the temperature distribution is not independent. Thus, the finest mesh, which consists of 1,497,840 nodes and 1,731,190 elements, was used for all the cases investigated in the study despite the higher computational demand involved.

Experimental data is required for a further validation of the SOEC model and for the physical and material properties which are currently from the literature. In the future work, more mesh independence tests will be performed on finer meshes to guarantee a complete mesh independence.

4. Results and discussion

The results of the parameter study are presented below for the different cases outlined in Table 4. First, the results from the effect of the different operating voltages on the current density, on the temperature and on the hydrogen molar fraction are discussed. Afterwards, a comparison between the cross-flow configuration and the parallel-flow one is given.

4.1. Variation of the operating voltage

Four different voltages have been tested to evaluate the effects on the parameters previously mentioned. The results from the different operating voltages correspond to cases No. 1–4 in Table 4. Note that the case No. 3 corresponds to the base case, a voltage very close to the thermo-neutral value at the operating temperature of 800 °C (1.2867 V), but operating under exothermic mode.

4.1.1. Current density distribution

Fig. 4 shows the current density distributions at the anode active layer surface for the four different operating voltages. The images correspond to the surface between the active layer and the diffusion layer. It is clear that a similar trend of the current density distribution is observed for the four cases presented. With increasing voltage, higher current densities (maximum values) are achieved and larger areas of higher current density values are observed as well. This is due to higher electron concentration at the solid regions and the diffusion mechanism of electrons from the solid interconnects to the porous layers and then to the reaction sites.

The current density distribution at the cathode active layer surface predicted for the different operating voltages are shown in Fig. 5. For this side, the results follow a similar trend as in the anode. This means, for higher operating voltages, higher current densities are achieved, having the highest values in those areas close to the interface with the channels' walls. Moreover, the maximum values of the current density for the cathode side (such as $2.65 \cdot 10^6$ A/m^2) are smaller than those obtained at the anodic site in Fig. 4. It is due to the fact that the cathode diffusion layer is much thicker than the anodic one making the electron transfer pathway strongly dominated in this side. Yet, similar distribution trends of the current density are observed for the four cases.

4.1.2. Temperature distribution

The temperature profile at the cathode active layer is presented in Fig. 6. The temperature profile at the anode side is omitted due to its similarity and thus, being of no relevance. In comparison with the current density distribution at different voltages, the temperature profiles shown in Fig. 6 present noticeable differences at first sight.

(a) 1.1 V

(b) 1.2867 V

(c) 1.3 V

(d) 1.5 V
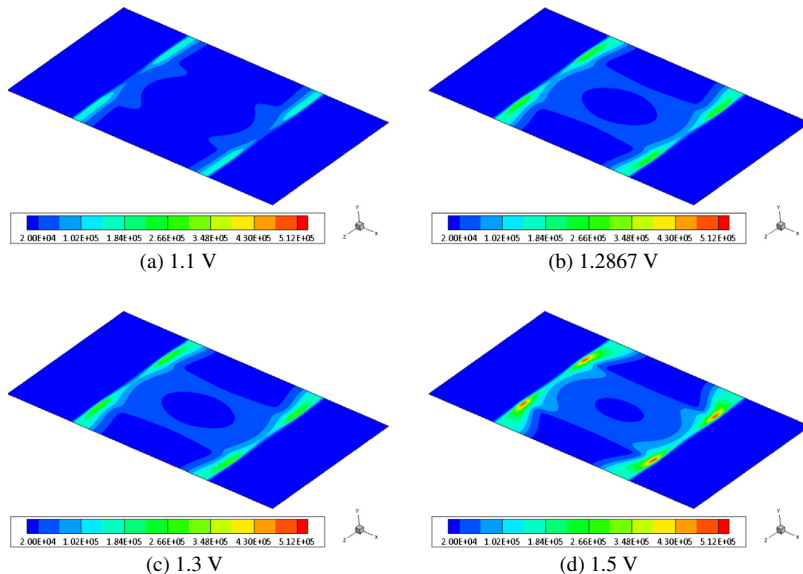
Fig. 4. Current density in $[A\,m^{-2}]$ at the anode active layer for different operating voltages.

(a) 1.1 V

(b) 1.2867 V

(c) 1.3 V

(d) 1.5 V
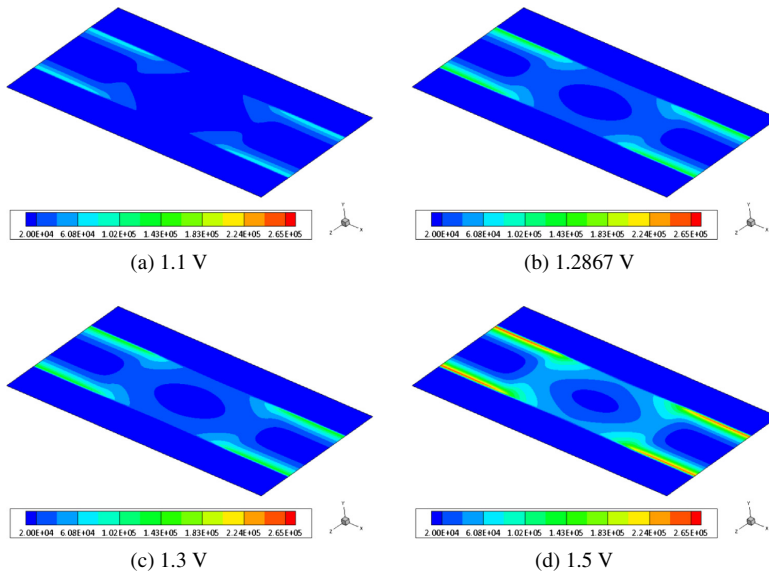
Fig. 5. Current density in $[A\,m^{-2}]$ at the cathode active layer for different operating voltages.

Fig. 6a presents the temperature distribution for 1.1 V which corresponds to a voltage below the thermo-neutral value and thus, the SOEC operates under the endothermic condition. Operating at the endothermic mode means that the electric energy is lower than the enthalpy change of reaction and heat must be externally supplied in order to maintain the electrochemical reaction as it is endothermic and thus, consumes heat. The results obtained for

1.1 V are consistent with the endothermic mode requirements. From Fig. 6a, a decrease in the temperature value is observed throughout the cell in the flow direction being highest at the region closest to the water channel inlet. As the reaction proceeds in the cell, a temperature drop is observed. However, if heat was supplied, the temperature could be maintained constant. Moreover, note that the temperature values are lower than the gas inlet

(a) 1.1 V

(b) 1.2867 V

(c) 1.3 V

(d) 1.5 V
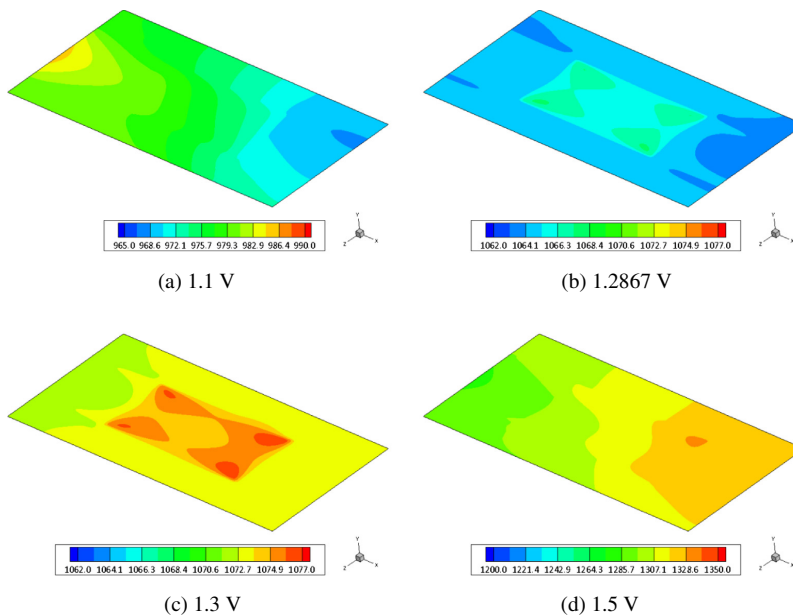
Fig. 6. Temperature in [K] at the cathode active layer for different operating voltages.
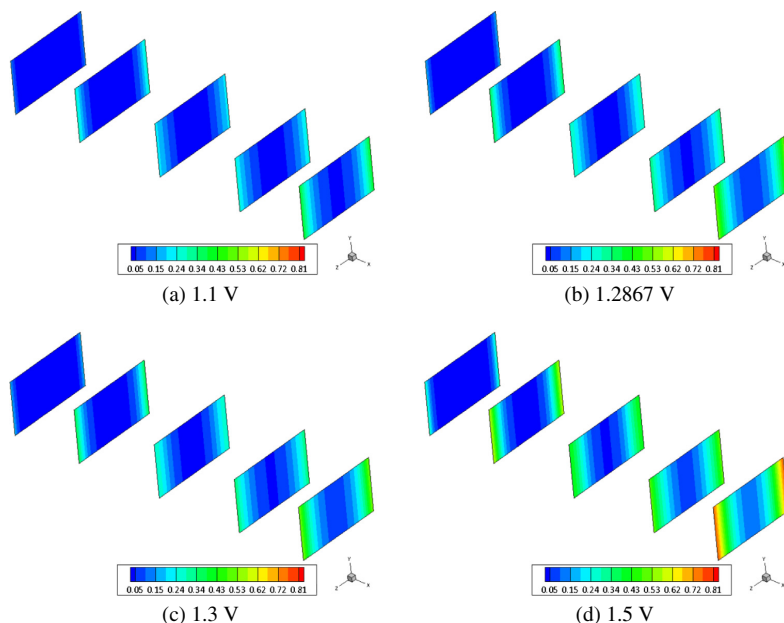
Fig. 7. Hydrogen molar fraction at the water channel for different operating voltages.

temperature, 1073 K. This temperature drop is due to the strong effect of the electrochemical reaction when operating at the endothermic mode.

The temperature distribution profile obtained from the exothermic operating mode corresponds to the SOEC operating at 1.5 V, Fig. 6d, as it is a higher voltage than the thermo-neutral one. Contrarily to the endothermic mode, the electric ohmic resistances are predominant against the enthalpy change of reaction in the exothermic mode and in order to maintain the same temperature, heat should be removed from the device. From Fig. 6d, an increase in the temperature values can be observed when moving downstream from the two channels, in a similar distribution as for the endothermic case in Fig. 6a, and the values presented are also higher than the inlet temperature values for the gas flow due to the predominance of electric resistances.

These two profiles in Fig. 6a and d are similar to those presented by the Argonne National Laboratory [24] despite the different operating voltages.

However, the temperature profiles shown in Fig. 6b and in Fig. 6c, are considerably different to the ones discussed previously. Fig. 6c corresponds to the 1.3 V which is the base case. Although the operating voltage 1.3 V is a bit higher than the thermo-neutral value, it is really close to, which can explain why the temperature distributions are very similar. The thermo-neutral voltage, 1.2867 V at 800 °C, is that point where the generated joule heat due to ohmic resistances in the cell and the heat consumption for the electrochemical reaction are the same. Thus, no heat must be supplied or removed to maintain the temperature constant. Fig. 6b, which corresponds to the thermo-neutral voltage, verifies this condition as the temperature difference in the cell is very small compared to the values obtained at 1.1 V and 1.5 V. The same happens for the 1.3 V case, Fig. 6c. Nevertheless, the temperature values are higher at 1.3 V than at the termo-neutral voltage which can indicate a slight effect from the joule heating due to operating at a voltage a bit higher than the thermo-neutral one.

4.1.3. Hydrogen production

The hydrogen molar fraction profiles obtained for the different operating voltages at different positions along the flow direction are shown in Fig. 7. The positions for the different profiles are: $x = 0.01$ m (by the channel inlet), $x = 0.05$ m, $x = 0.1$ m, $x = 0.15$ m and $x = 0.19$ m (close to the channel outlet).

Fig. 8. Current density in $[A\ m^{-2}]$ at the electrodes' active layer for parallel-flow condition.

Fig. 9. Temperature distribution in [K] at the cathode active layer for parallel-flow condition.

As expected, the highest molar fraction, $Y_{H_2} = 0.81$, is obtained at the highest operation voltage, 1.5 V, see Fig. 7d. Lower values are obtained for the 1.3 V, $Y_{H_2} = 0.58$, and for the 1.287 V, $Y_{H_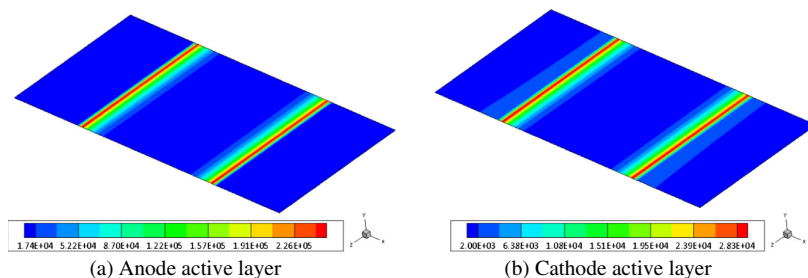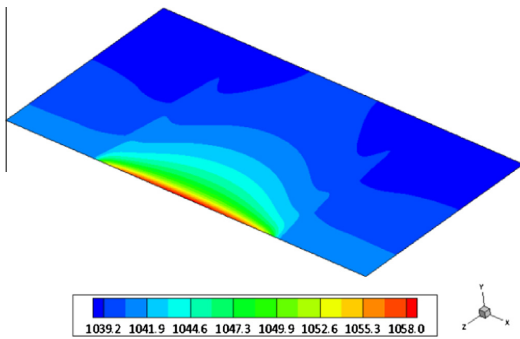2} = 0.55$. The lowest one is obtained for the case corresponding to the 1.1 V, $Y_{H_2} = 0.51$. This leads to emphasize the strong relationship between the operating voltage and the hydrogen molar fraction produced. However, other parameters affect this relation. When operating in the exothermic mode, which means operating at high voltages, high current densities can be obtained leading to larger hydrogen molar fractions when compared to lower operating voltages. Considerably higher current density values are obtained at the higher voltage for the cathodic and anodic sides than for the cases at or close to the thermo-neutral voltage or operating at the endothermic mode, see Figs. 4 and 5. Thus, depending on the operating mode, i.e., exothermic, thermo-neutral or endothermic, the higher or lower values of the current density achieved affect the hydrogen production in an SOEC device.

4.2. Effect of flow configuration

An SOEC operating in parallel-flow arrangement has been also simulated to investigate the effects of the flow configuration on the current density, temperature and hydrogen production of the electrolysis cell. The results obtained from the parallel-flow configuration are compared with those from the base case, which operates in cross-flow mode. The parallel-flow configuration case corresponds to case No. 5 in Table 4.

The parallel-flow case operates in co-flow mode, i.e., the cathodic and the anodic channel inlets are specified at the same side of the cell located at $z = 0.2$ m.

4.2.1. Current density distribution

The current density distributions at the anode and cathode active layers are shown in Fig. 8. The anode current density distribution is presented in Fig. 8a while the cathodic one appears in Fig. 8b. Not like in the base case, Figs. 4c and 5c, the highest values of the current density are identified at the continuous regions corresponding to the interface between the respective channel and the side interconnects. Moreover, the anode side also presents higher current density values than the cathode side. However, note here that different scales for the current density have been used due to the big differences in the order of magnitude between the two electrodes. Yet, a similar distribution profile is obtained for both sides. In general, the maximum current density values for the parallel-flow configuration are slightly lower than those obtained for the cross-flow configuration, but still the values remain in the same order of magnitude.

4.2.2. Temperature distribution

Fig. 9 shows the predicted temperature profile when operating in parallel-flow configuration. Only the temperature at the cathode active layer surface is presented as a similar profile is obtained for the respective surface at the anode side. A large temperature gradient is observed in the parallel-flow case compared to the cross-flow one in Fig. 6c. Moreover, the temperature decreases along the flow direction and lower values than the inlet temperature are observed. These results contradict the general definition of the exothermic operating mode where the temperature should increase in the cell along the flow direction due to joule heating by the ohmic resistances. It could be possible that when operating in parallel-flow configuration, the diffusion pathway for the reaction species is shorter and thus, the electrochemical reactions become much stronger and predominate at voltages near the thermo-neutral value. Nevertheless, different operating voltages should be applied in further studies on this phenomenon observed for the parallel flow configuration.

4.2.3. Hydrogen production

Last of all, the hydrogen molar fraction profile for the different cross-sections along the flow direction for the water channel are presented in Fig. 10. The different cross-sections showed correspond to the same locations defined in the x direction in Fig. 7.
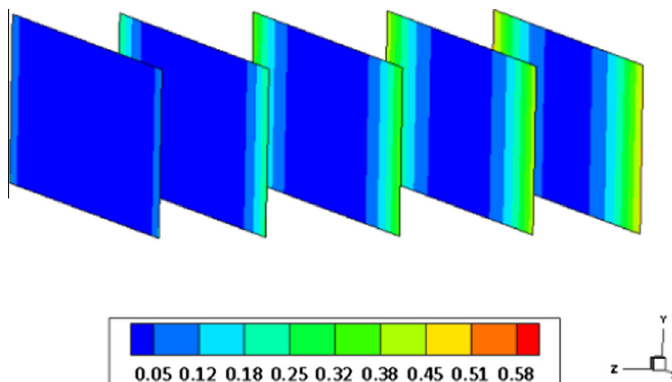

Fig. 10. Hydrogen molar fraction at the water channel for parallel-flow condition.

The main finding is that the average hydrogen molar fraction at the water channel outlet is lower, namely $Y_{H_2} = 0.50$, when operating in parallel-flow and when operating in cross-flow configuration, $Y_{H_2} = 0.58$. An explanation of this drop in the hydrogen molar fraction can be the lower current densities obtained for the parallel-flow configuration.

5. Conclusions

The behavior of the current density, the temperature distribution and the hydrogen production in an SOEC have been numerically investigated under different operating and configuration parameters.

First, four different operating voltages have been applied to evaluate their effects on the aforementioned parameters. With higher operating voltages, higher current densities are obtained. Furthermore, the temperature distribution profiles present noticeable differences. Depending on the operating voltage, the temperature simulation reveals the three thermal operating modes of an SOEC, i.e., endothermic, thermo-neutral and exothermic. A higher hydrogen molar fraction is obtained with a higher operating voltage although the effects from the current density as well as the thermal operation modes should be taken into account.

Second, a parallel-flow arrangement has been simulated to investigate the effects of the flow configuration in the SOEC. Not like in the base case, the highest values of the current density are identified at the continuous regions corresponding to the interface between the respective channel and the side interconnects. However, the anode side presents higher current density values than the cathodic side as in the cross-flow base case. Yet, the parallel-flow arrangement presents lower current density values than the cross-flow case although they remain in the same order of magnitude. A large temperature difference is observed due to the parallel-flow configuration. A lower hydrogen molar fraction is obtained, $Y_{H_2} = 0.5$, because of the lower current densities obtained in the parallel-flow configuration.

To sum up, the parametric studies performed allow to obtain a general idea of the behavior of the SOEC performance when some cell parameters are modified. However, more studies are required, especially for the parallel-flow configuration in order to obtain detailed results for better understanding of the relations between SOEC operating and cell design parameters.

Acknowledgements

References

[1] Ni M. Computational fluid dynamics modeling of a solid oxide electrolyzer cell for hydrogen production. Int J Hydrogen Energy 2009;34(18):7795–806.
[2] Agency IE. Hydrogen production and storage. Tech rep. International Energy Agency; 2006.
[3] Sherif SA, Barbir F, Veziroglu TN. Wind energy and the hydrogen economy – review of the technology. Sol Energy 2005;78(5):647–60.
[4] Ni M, Leung DYC, Leung MKH, Sumathy K. An overview of hydrogen production from biomass. Fuel Process Technol 2006;87(5):461–72.
[5] Lee MS, Goswami DY, Stefanakos EK. Immobilization of calcium oxide solid reactant on a yttria fabric and thermodynamic analysis of UT-3 thermochemical hydrogen production cycle. Int J Hydrogen Energy 2009;34(2):745–52.
[6] Sigurvinsson J, Mansilla C, Lovera P, Werkoff F. Can high temperature steam electrolysis function with geothermal heat? Int J Hydrogen Energy 2007;32(9):1174–82.
[7] Herring JS, O'Brien JE, Stoots CM, Hawkes GL, Hartvigsen JJ, Shahnam M. Progress in high-temperature electrolysis for hydrogen production using planar SOFC technology. Int J Hydrogen Energy 2007;32(4):440–50.
[8] Hauch A, Jensen S, Ebbesen S, Mogensen M. Durability of solid oxide electrolysis cells for hydrogen production. Denmark. Forskningscenter Risoe. Risoe-R, Ris National Laboratory; 2007, p. 327–338. ISBN 978-87-550-3603-1.
[9] Jensen SH, Larsen PH, Mogensen M. Hydrogen and synthetic fuel production from renewable energy sources. Int J Hydrogen Energy 2007;32(15):3253–7.
[10] Ni M, Leung MKH, Leung DYC. A modeling study on concentration overpotentials of a reversible solid oxide fuel cell. J Power Sources 2006;163(1):460–6.
[11] Laguna-Bercero MA. Recent advances in high temperature electrolysis using solid oxide fuel cells: a review. J Power Sources 2012;203(0):4–16.
[12] Udagawa J, Aguiar P, Brandon NP. Hydrogen production through steam electrolysis: Model-based steady state performance of a cathode-supported intermediate temperature solid oxide electrolysis cell. J Power Sources 2007;166(1):127–36.
[13] Udagawa J, Aguiar P, Brandon NP. Hydrogen production through steam electrolysis: model-based dynamic behaviour of a cathode-supported intermediate temperature solid oxide electrolysis cell. J Power Sources 2008;180(1):46–55.
[14] Udagawa J, Aguiar P, Brandon NP. Hydrogen production through steam electrolysis: control strategies for a cathode-supported intermediate temperature solid oxide electrolysis cell. J Power Sources 2008;180(1):354–64.
[15] Cai Q, Luna-Ortiz E, Adjiman CS, Brandon NP. The effects of operating conditions on the performance of a solid oxide steam electrolyser: a model-based study. Fuel Cells 2010;10(6):1114–28.
[16] Ni M. 2D thermal modeling of a solid oxide electrolyzer cell (SOEC) for syngas production by H2O/CO2 co-electrolysis. Int J Hydrogen Energy 2012;37(8):6389–99.
[17] Ni M, Leung MKH, Leung DYC. Mathematical modeling of the coupled transport and electrochemical reactions in solid oxide steam electrolyzer for hydrogen production. Electrochim Acta 2007;52(24):6707–18.
[18] Grondin D, Deseure J, Brisse A, Zahid M, Ozil P. Simulation of a high temperature electrolyzer. J Appl Electrochem 2010;40(5):933–41.
[19] Jin X, Xue X. Computational fluid dynamics analysis of solid oxide electrolysis cells with delaminations. Int J Hydrogen Energy 2010;35(14):7321–8.
[20] Laurencin J, Kane D, Delette G, Deseure J, Lefebvre-Joud F. Modelling of solid oxide steam electrolyser: Impact of the operating conditions on hydrogen production. J Power Sources 2011;196(4):2080–93.
[21] Hawkes G, O'Brien J, Stoots C, Hawkes B. 3D CFD model of a multi-cell high-temperature electrolysis stack. Int J Hydrogen Energy 2009;34(9):4189–97.
[22] O'Brien JE, McKellar MG, Stoots CM, Herring JS, Hawkes GL. Parametric study of large-scale production of syngas via high-temperature co-electrolysis. Int J Hydrogen Energy 2009;34(9):4216–26.
[23] O'Brien JE. Thermodynamics and transport phenomena in high temperature steam electrolysis cells. J Heat Transfer 2012;134(3). pp. 031017–031017.
[24] Yildiz B, Smith J, Sofu T. Thermal-fluid and electrochemical modeling and performance study of a planar solid oxide electrolysis cell: analysis on SOEC resistances, size and inlet flow conditions. Tech rep. Argonne National Laboratory, Nuclear Engineering division; 2006.
[25] Zhang H, Wang J, Su S, Chen J. Electrochemical performance characteristics and optimum design strategies of a solid oxide electrolysis cell system for carbon dioxide reduction. Int J Hydrogen Energy 2013;38(23):9609–18.
[26] Xie Y, Xue X. Modeling of solid oxide electrolysis cell for syngas generation with detailed surface chemistry. Solid State Ionics 2012;224(0):64–73.
[27] Shi Y, Luo Y, Cai N, Qian J, Wang S, Li W, et al. Experimental characterization and modeling of the electrochemical reduction of CO_2 in solid oxide electrolysis cells. Electrochim Acta 2013;88(0):644–53.
[28] Li W, Shi Y, Luo Y, Cai N. Elementary reaction modeling of CO_2/H_2O co-electrolysis cell considering effects of cathode thickness. J Power Sources 2013;243(0):118–30.
[29] FLUENT A. Fuel cell modules manual; 2012.
[30] Merk H. The macroscopic equations for simultaneous heat and mass transfer in isotropic, continuous and closed systems. Appl Sci Res 1959;A8:26.
[31] Kong W, Zhu H, Fei Z, Lin Z. A modified dusty gas model in the form of a Fick's model for the prediction of multicomponent mass transport in a solid oxide fuel cell anode. J Power Sources 2012;206(0):171–8.

Paper III

A Three Dimensional Multiphysics Model of a Solid Oxide Electrochemical Cell for Degradation Studies

Maria Navasa[1,2], Christopher Graves[2], Christodoulos Chatzichristodoulou[2], Theis Løye Skafte[2,3], Bengt Sundén[1] and Henrik Lund Frandsen[2]

[1]Department of Energy Sciences, Lund University, Sweden
[2]Department of Energy Conversion and Storage, Technical University of Denmark, Denmark
[3]Haldor Topsoe A/S, Denmark

Abstract

Mitigating degradation is essential for extending the lifetime of solid oxide electrochemical cells (SOC). Temperature, gas compositions and local overpotentials may all have an effect on various degradation phenomena, and these all vary spatially in SOC stacks and single cell tests. Furthermore, in-situ monitoring of the local conditions is extremely challenging and impossible to perform on a regular basis. Modeling can however be utilized for retrieving local quantities. In this work, a three dimensional multiphysics model was developed to simulate the performance of solid oxide electrochemical cells, operating either in fuel cell or electrolysis mode. The main transport phenomena are included and coupled to the electrochemical reactions. This enables the calculation of

1

the local partial gas pressures, potentials and temperature distributions through the electrodes and across the cells as function of the operating voltage. The model is validated by comparison to cell test experiments at different operating conditions, i.e. with H_2/H_2O as feedstock at different temperatures, flows and gas compositions.

keywords: SOCs, SOECs, modeling, three dimensional, potential distribution, overpotential, transport phenomena, electrochemical reactions, validation, temperature distribution, current density, heat transfer.

1   Introduction

Solid oxide electrochemical cells (SOCs) are devices that can be operated reversibly as electrolysis cells (SOECs) to produce hydrogen (H_2), carbon monoxide (CO) or syngas (CO and H_2 simultaneously) using electrical energy, or as fuel cells (SOFCs) to produce electrical energy using the same fuels.

Optimizing performance by modeling of SOFCs resulted in substantial amounts of research over the past twenty years [1–16]. However, limited amount of the modeling work has been focused on the SOEC operation mode and even less on degradation issues connected to SOEC operation. Despite the similarities between the two operation modes, the different operating voltage ranges and the gradients involved influence the long-term degradation and performance in different ways.

The performance and durability of SOCs is function of the cell geometry, the materials selected, the cell manufacturing process, particle sizes, porosity, tortuosity and operating parameters such as temperature, pressure, gas flow rates, cell voltage, gas composition, etc. In order to become commercially interesting, the durability of SOCs or knowledge about operation must be improved as degradation issues hinder the long-term operation of the cells.

Until most recently, the majority of the SOEC models reported are based on one dimensional (1D) mathematical models or 1D/2D multiphysics simulations on a unit cell or a

stack of planar SOECs, where parametric studies are performed [17–31].

Ni [19] developed a 1D numerical model considering only mass transfer and the electrochemical reactions at micro-scale level to study the effect of the gas transport on the concentration polarizations. Other 1D mathematical models that can be found are, for example, Udagawa *et al.* and Cai *et al.* [20–23], who extended Ni's model by incorporating heat transfer for a cathode-supported planar SOEC stack for steady and unsteady state.

The variations of various quantities across the cells and stacks are however significant under realistic operating conditions, and this type of 1D models will not describe this variation. For this, 2D or 3D models are needed depending on flow geometry and possible assumptions regarding the flow and thermal field.

Regarding multiphysics simulations, 2D models are the most reported ones. Grondin *et al.* [24] conducted a simulation of a circular SOEC taking into account charge, mass and heat transfer. Jin and Xue [25] developed a more complete 2D planar SOEC model considering the coupling between charge balance, electrochemical reaction kinetics, mass, momentum and energy balances to evaluate the SOEC performance due to the size and position of delaminations at the electrode/electrolyte interface. Ni [17, 18] also developed multiphysics models for a 2D planar cell operating in co-flow configuration for both H_2O electrolysis and co-electrolysis of H_2O and CO_2. Laurencin *et al.* [26] further introduced the Dusty gas model (DGM) for a more accurate description of the resistance due to gas diffusion in the porous cathodes. They further enhanced the computational efficiency of the in-house code by an analytical integration of the DGM. The effects of the cell polarizations, geometry and operation parameters as well as the radiative heat losses were studied for an SOEC stack. Back to cell level, Chatzichristodoulou *et al.* [32] recently developed a 2D SOC model for single or bi-layer electrolyte, including activation, concentration and conversion contributions to both electrodes, and mixed ionic and electronic transport within the electrolyte layers. This model was used for a sensitivity analysis showing detailed potential distributions in the electrolyte and at the electrolye/electrode interfaces as a starting point for discussing degradation mechanisms.

The first three dimensional (3D) model was reported by Hawkes *et al.* [27] and O'Brien

3

et al. [28–30]. Hawkes *et al.* presented 3D multiphysics cell stack models, operating in cross-flows configuration, including all the transport conservation equations as well as the electrochemical reactions developed with the commercial computational fluid dynamics (CFD) code Ansys Fluent with a modified SOFC add-on module to account for the electrolysis mode. Ansys Fluent, as with other commercial codes, presents some limitations, i.e. the geometry of the electrolyte is simplified by treating the electrolyte as a 2D component, resulting in a zero thickness electrolyte or not considering Knudsen diffusion in porous electrodes. The latest versions of Ansys Fluent considers electrolysis in the fuel cell add-on module, but it is only valid for H_2/H_2O as feedstock. Moreover, no spatial resolution of overpotentials, among other parameters, is possible because of reactive zones being collapsed. Apart from Hawkes *et al.*, not many similar models have been reported so far. Boëdec *et al.* [31] developed a new 3D cell stack design, also with Ansys Fluent, based on metallic seals to evaluate the contact resistance under operation as it appears to be a critical issue for the electrode performance.

In this work, a 3D multiphysics model of a planar solid oxide electrochemical cell has been developed and validated with experimental data with H_2/H_2O as feedstock at different temperatures, flows and gas compositions. The model considers the main physical phenomena taking place in such devices. This is achieved by a full description of the spatial variation of gas compositions (in channels and porous electrodes), electric potential, ionic potential, overpotentials, temperature and couplings through local electrochemical reaction. Hereby, the spatial variation of the overpotentials is modeled, which is a main factor for many types of degradation of SOCs.

The developed model describes both SOEC and SOFC modes of operation, but it is mainly verified towards electrolysis experiments. The model is built with the finite element method (FEM) based commercial software Comsol Multiphysics 5.2 using the Batteries and Fuel Cells module. Moreover, overall considerations such as a distributed reaction zone trough the electrode (reactive zones are not collapsed), steady state condition or gases treated as ideal gases are accounted.

2   Model description

In this section the partial differential equations to describe the physical phenomena occurring in the SOCs are provided, i.e. electrochemical reactions, transport of charged species, momentum transfer, mass transfer and heat transfer. State-of-the-art models for the different phenomena are used for all of these, except for the electrochemical model, where the method to obtain the spatially varying overpotentials is presented.

2.1   Electrochemical reactions

The electrochemical reaction for water electrolysis in a solid oxide electrolysis cell takes place at the active layers of the electrodes. Reduction of water to hydrogen, Eq. (1), occurs at the cathodic triple phase boundaries (3PBs), while oxidation of oxide ions to oxygen, Eq. (2), takes place at the reactive surfaces of the anodic mixed conductor.

$$H_2O_{(g)} + 2\,e^- \rightleftharpoons H_{2(g)} + O^{2-} \tag{1}$$

$$O^{2-} \rightleftharpoons \tfrac{1}{2}\,O_{2(g)} + 2\,e^- \tag{2}$$
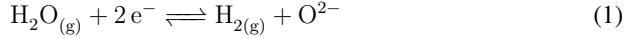
The current generated by the above electrochemical reactions is often calculated with the Butler-Volmer equation, which relates the current density with the activation overpotential at each electrode-electrolyte interface. The general Butler-Volmer equation is [33, 34]:

$$i = i_0 \left[\exp\left(\alpha_a \frac{n_e F}{RT} \eta_{\text{act}} \right) - \exp\left(-\alpha_c \frac{n_e F}{RT} \eta_{\text{act}} \right) \right] \tag{3}$$

where R is the ideal gas constant, n_e is the number of electrons participating in the electrochemical reaction, T the temperature, F the Faraday constant, i_o is the exchange current

density, which strongly depends on the cell materials, construction and temperature and i is the current density, both in $[\mathrm{A\,m^{-2}}]$. α_a and α_c are the charge transfer coefficients for each electrochemical half-reaction governed by the electron transfer process at the 3PB and η_{act} is the activation overpotential.

Most of the researchers, both experimentalists and modelers, still assume that a Butler-Volmer type of equation describes the full current-voltage (*i*-V) curve despite no direct experimental values that support this hypothesis. Mogensen *et al.* point out different arguments against the Butler-Volmer equation being descriptive of the full *i*-V curve, citing [35];

- *Composite electrodes do not follow a Butler-Volmer type expression.*

- *There is no experimental evidence that charge transfer, as described by the Butler-Volmer equation, is a rate limiting SOC electrode reaction.*

- *There will not be any single simple potential barrier to charge transfer. Charge transfer is limited by surface diffusion and transport through the surface layers.*

- *Electron transfer does not occur at a well-defined interface near the 3PB with a single activation barrier. It takes place through a non-homogeneous chemical and microstrucural layer which varies with temperature, time, gas compositions, etc. and several varying activation barriers.*

- *Complicated structures with several particle types involved will probably have a multi-step reaction mechanism with more than one process contributing to the polarization resistance.*

For all the reasons stated, linear Chang-Jaffe kinetics [36] are used in this work to calculate the current density at the electrodes instead of the Butler-Volmer equation. At the fuel side, Eq. (4) is used while at the air side, Eq. (5) is valid [37, 38].

$$i_{\mathrm{fuel}} = \frac{\eta}{R_{0,\mathrm{red}} \exp\left(\frac{E_{a,\mathrm{red}}}{RT}\right) a_{\mathrm{H_2}}^{0.1} a_{\mathrm{H_2O}}^{-0.33}} \tag{4}$$

$$i_{\text{air}} = \frac{\eta}{R_{0,\text{ox}} \exp\left(\frac{E_{a,\text{ox}}}{RT}\right) a_{\text{O}_2}^{-0.25}} \tag{5}$$

where η is the overpotential, a_i is the activity of the component i in the correspondent gas mixture, E_a is the activation energy of the activation polarization resistance and R_0 is the pre-exponential factor of this resistance.

The overpotential, η, is related to the electromotive potential, π, and the Galvani potential, ϕ, at a state i and at equilibrium as follows:

$$\eta = \left(\pi^i - \phi^i\right) - \left(\pi^{\text{eq}} - \phi^{\text{eq}}\right) \tag{6}$$

The electromotive potential π, also known as the Fermi potential, can be interpreted as the electric potentials of the cell terminals. On the other hand, the Galvani potential ϕ can be understood as the electric potential in the interior of the solid [39].

The electromotive and Galvani potentials at equilibrium $(\pi^{\text{eq}} - \phi^{\text{eq}})$ for SOC operation, can be determined as follows. By considering the electrochemical reaction at the oxygen electrode, Eq. (2), the equilibrium condition in terms of electrochemical potentials is:

$$\eta_{\text{O}^{2-}} = \frac{1}{2}\mu_{\text{O}_{2(g)}} + 2\eta_{\text{e}^-} \tag{7}$$

where $\mu_{\text{O}_2(g)}$ is the chemical potential of $\text{O}_{2(g)}$ and $\eta_{\text{O}^{2-}}$ and η_{e^-} are the electrochemical potentials of the oxide ions respectively electrons, which are defined as [39]:

$$\eta_{\text{O}^{2-}} = \mu_{\text{O}^{2-}} - 2F\phi \tag{8}$$

$$\eta_{\text{e}^-} = \mu_{\text{e}^-} - F\phi \tag{9}$$

where $\mu_{O^{2-}}$ and μ_{e^-} are the chemical potentials of the oxide ions and electrons, respectively, ϕ is the Galvani potential and F is the Faraday constant.

The electromotive potential is by definition related to the electrochemical potential as [39]:

$$\pi = \frac{-\eta_{e^-}}{F} \tag{10}$$

By inserting and combining Eqs. (8) to (10) in Eq. (7) taken at equilibrium ($\pi = \pi^{eq}$, $\phi = \phi^{eq}$), and that the chemical potential of a component i in an ideal gas mixture (O_2) can be expressed as function of the chemical potential of this species at a reference state plus the contribution from the temperature, pressure and composition, one obtains:

$$\left(\pi^{eq} - \phi^{eq}\right)_{\text{air}} = \frac{1}{4F}\left(\mu_{O_2}^* + RT\ln a_{O_2}\right) - \frac{\mu_{O^{2-}}}{2F} \tag{11}$$

where $\mu_{O_2}^*$ is the chemical potential of $O_{2(g)}$ at a reference state and $\mu_{O^{2-}}$ is the chemical potential of the oxide ions. The chemical potential of oxide ions is assumed to be constant as consequence of considering that the electrolyte has constant oxygen stoichiometry.

By following the same procedure, but for the electrochemical reaction taking place at the fuel electrode, Eq. (1), one obtains:

$$\left(\pi^{eq} - \phi^{eq}\right)_{\text{fuel}} = \frac{1}{2F}\left(\mu_{H_2O}^* - \mu_{H_2}^* + RT\ln\left(\frac{a_{H_2O}}{a_{H_2}}\right)\right) - \frac{\mu_{O^{2-}}}{2F} \tag{12}$$

The open circuit voltage of the cell (OCV) is the difference in the electromotive potentials of the electrodes at equilibrium, also known as equilibrium potential difference, and it is the minimum cell voltage required to decompose water, Eq. (13), (assuming negligible leak current at OCV).

$$V_{\text{cell}}^{\text{eq}} = \pi_{\text{air}}^{\text{eq}} - \pi_{\text{fuel}}^{\text{eq}} = \frac{\frac{1}{2}\mu_{\text{O}_2}^* + \mu_{\text{H}_2}^* - \mu_{\text{H}_2\text{O}}^*}{2F} + \frac{RT}{2F}\ln\left(\frac{a_{\text{H}_2}a_{\text{O}_2}^{\frac{1}{2}}}{a_{\text{H}_2\text{O}}}\right) \tag{13}$$

For implementing the electromotive potentials at equilibrium in the model for each electrode, the following expressions are used:

$$\pi_{\text{air}}^{\text{eq}} = \frac{RT}{2F}\ln\left(p_{\text{O}_2}^{\frac{1}{2}}\right) \tag{14}$$

$$\pi_{\text{fuel}}^{\text{eq}} = \frac{\Delta G_{rx,\text{H}_2\text{O}}}{2F} - \frac{RT}{2F}\ln\left(\frac{p_{\text{H}_2}}{p_{\text{H}_2\text{O}}}\right) \tag{15}$$

where $\Delta G_{rx,\text{H}_2\text{O}}$ is the Gibbs energy change for the water splitting at standard conditions, which is equal to $\frac{1}{2}\mu_{\text{O}_2}^* + \mu_{\text{H}_2}^* - \mu_{\text{H}_2\text{O}}^*$. Note that the chemical potential of the oxide ion, $\mu_{\text{O}^{2-}}$, is not taken into account for each electrochemical reaction as in the end, it cancels out at cell level, see Eq. (13). The reason is that it is an unknown value, as the electrochemical potential of an ion in solution cannot be measured independently and thus, the ion activity cannot be determined.

The Gibbs energy change is implemented as a temperature dependent function with data obtained from the FactSage 5.5 database. The Gibbs energy change used in the model, Eq. (16), is only valid for temperatures between 600 and 900 °C.

$$\Delta G_{rx,\text{H}_2\text{O}} = -0.0031T^2 - 49.119T + 244778 \tag{16}$$

where T is the temperature in [K] and $\Delta G_{rx,\text{H}_2\text{O}}$ in [J mol^{-1}].

To help make the potentials and overpotential distribution in an SOC more tangible, these are exemplified in Figures 1 and 2. Figure 1 shows the distribution of the electromotive potential (π), the electromotive potential at equilibrium (π^{eq}), the Galvani potential (ϕ)

as well as the overpotential (η) when the cell operates in fuel cell mode. The potentials and overpotentials shown follow Eq. (6) when $\phi^{eq} = 0$. Moreover, the cell voltage (V_{cell}) as well as the equilibrium cell voltage (V^{eq}) are shown.
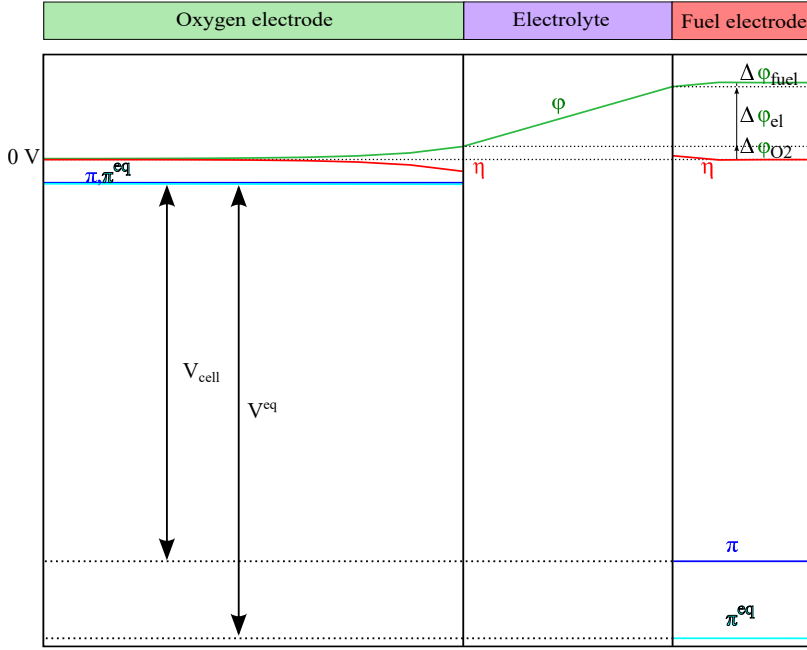
Figure 1: *Potentials and overpotential distribution across the oxygen electrode, electrolyte and fuel electrode thicknesses for fuel cell mode.*

Figure 2 is the equivalent to Figure 1 but for electrolysis mode under the same conditions. In fuel cell mode the operating cell voltage is lower than the equilibrium cell voltage due to the contribution of the overpotential. In electrolysis mode it is the opposite: the overpotential contributes to the cell voltage resulting in an operating cell voltage higher than the equilibrium cell voltage.

Moreover, how the resistances of the electrodes and the electrolyte affect the Galvani potential in both cell modes as well as the overpotential distribution across the electrodes can be seen in both figures.
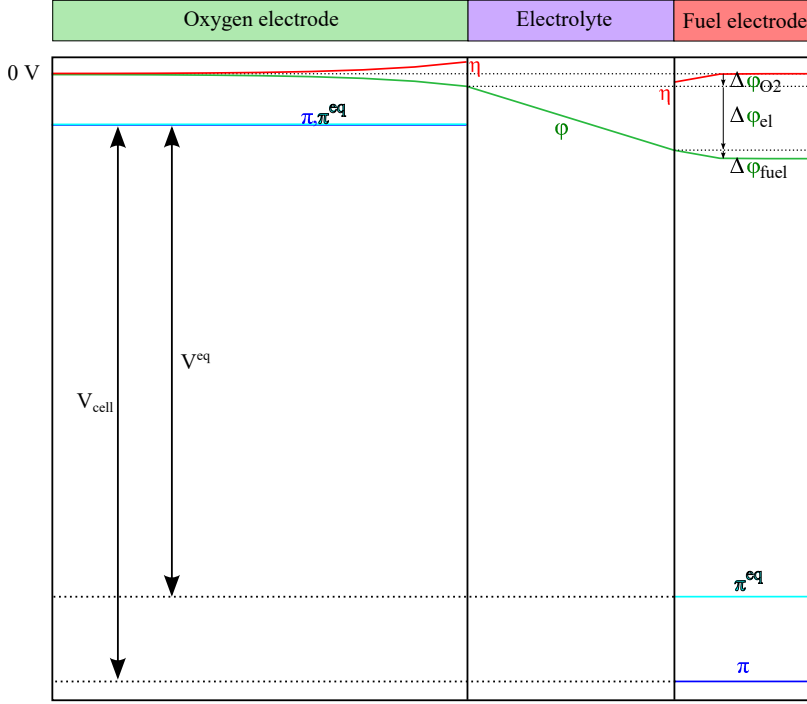
Figure 2: *Potentials and overpotential distribution across the oxygen electrode, electrolyte and fuel electrode thicknesses for electrolysis mode.*

In some commercial codes like Comsol Multiphysics, the Galvani potential is referred to as ϕ_l while the electromotive potential is known as ϕ_s.

2.2 Transport of charged species

The transport of ions and electrons is described by the current conservation equation and Ohm's law, Eq. (17) [1, 19, 40, 41].

$$\nabla \cdot \mathbf{J} = -\nabla \cdot \left(\frac{\sigma}{n_e F} \nabla \eta_{\mathrm{O^{2-}/e^-}} \right) = S_\eta \qquad (17)$$

where $\mathbf{J}$ is the current density flux, σ is the ionic or electronic conductivity, $\eta_{\mathrm{O^{2-}/e^-}}$ the ionic or electronic electrochemical potential and S_η is the related source term which is defined as follows:

$$S_\eta = \begin{cases} 0 & \text{in electrochemical inactive layers} \quad (18) \\ j & \text{in electrochemical active layers} \quad (19) \end{cases}$$

where j is the volumetric current density $[\mathrm{A\,m^{-3}}]$. The electrochemical active areas correspond to the fuel electrode and the oxygen electrode in Figure 3, where the electrochemical reactions are defined.

When considering the ionic electrochemical potential, $\eta_{\mathrm{O^{2-}}}$, Eq. (17) can be expressed in terms of the Galvani potential, ϕ, by considering Eq. (8) as follows:

$$\nabla \cdot \mathbf{J} = \nabla \cdot (\sigma \nabla \phi) = S_\eta \qquad (20)$$

For the electronic electrochemical potential, $\eta_{\mathrm{e^-}}$, Eq. (17) can be rewritten in terms of the electromotive potential, π, by implementing Eq. (10). The current conservation equation becomes then:

$$\nabla \cdot \mathbf{J} = \nabla \cdot (\sigma \nabla \pi) = S_\eta \qquad (21)$$

For porous media, an effective ionic or electronic conductivity is calculated as:

$$\sigma_{eff} = \sum_{i=1}^{N} \sigma_i \frac{\chi_i}{\tau_{\mathrm{i}}^2} \qquad (22)$$

12

where χ_i is the volume fraction of the electron or ion conducting material i in the electrode and τ_i the corresponding tortuosity. The volume fractions and the tortuosity values used are defined in Table 3 and are obtained from calculations on a 3D microstructure reconstruction model from DTU Energy cells sectioning the microstructure with a focused ion beam and imaging with a scanning electron microscope (FIB-SEM). The data is presented elsewhere [42] and the method explained in [43].

2.3   Momentum transfer

Momentum transfer of the gas flows takes place in the gas channels and in the porous electrodes. The porous electrodes consist of the diffusion and the electrochemical active layers in the air and fuel electrodes (contact layer and oxygen electrode for the air side and porous support and fuel electrode for the fuel side in Figure 3). The momentum conservation equation used in the model is given by [44]:

$$\nabla \cdot (\rho \mathbf{U}\mathbf{U}) = -\nabla p + \nabla \cdot (\mu \nabla \mathbf{U}) + S_d \qquad (23)$$

where $\mathbf{U}$ is the velocity vector, p the pressure, μ the dynamic viscosity of the gas mixture, ρ the density and S_d is the momentum source term, which is described as follows according to the different cell regions.

$$S_d = \begin{cases} 0 & \text{in gas channels} & (24) \\ -\dfrac{\mu}{K_0}\mathbf{U} & \text{in porous layers} & (25) \end{cases}$$

where K_0 is the permeability of the porous medium and is defined in Table 3.

The dynamic viscosity of a gas mixture at relative low pressures, common operating conditions for SOC applications, is calculated via the Wilke's method, Eqs. (26) to (28),

based on the kinetic theory approach [45] and using Einstein's summation convention in Eq. (26).

$$\mu_m = \frac{Y_i \mu_i}{Y_j A_{ij}} \tag{26}$$

$$A_{ij} = \frac{\left[1 + \left(\frac{\mu_i}{\mu_j}\right)^{\frac{1}{2}} \left(\frac{M_j}{M_i}\right)^{\frac{1}{4}}\right]^2}{\left[8\left(1 + \frac{M_i}{M_j}\right)\right]^{\frac{1}{2}}} \tag{27}$$

$$A_{ji} = \frac{\mu_j}{\mu_i} \frac{M_i}{M_j} A_{ij} \tag{28}$$

where Y_i and Y_j are the molar fractions of components i and j in a gas mixture of n components, μ_i is the pure dynamic viscosity of component i and M_i and M_j are the molar masses of the aforementioned components. The pure dynamic viscosity for each component is implemented as a temperature dependent polynomial function as suggested in [46].

2.4   Mass transfer

Conservation of mass throughout the whole computational domain is fulfilled by enforcing the continuity equation, Eq. (29).

$$\nabla \cdot (c\mathbf{U}) = S_m \tag{29}$$

where c is the molar density, which can be calculated via the ideal gas law for a system like SOCs, and S_m is the mass source term due to the electrochemical reactions. The

mass source stems from the reacting species, and is thus linked to electrochemical reactions and the exchange current density as:

$$S_m = \begin{cases} 0 & \text{in non-electrochemical active layers} \quad (30) \\ \displaystyle\sum_i^n \frac{j}{n_e F} & \text{in electrochemical active layers} \quad (31) \end{cases}$$

where n_e is the number of electrons transferred per molecule of hydrogen or carbon monoxide produced and j is the volumetric current density. For a system where oxide ions (O^{2-}) are transported through the electrolyte, $n_e = 2$ [30].

As a mixture of n species is modeled, a species balance equation for $(n - 1)$ components is also required, Eq. (32), apart from the continuity equation, Eq. (29). Four different species are modeled for the SOEC in this work: hydrogen and water vapor for the fuel electrode, and oxygen and nitrogen for the oxygen electrode. Nitrogen is an inert gas acting as a carrier gas for the produced oxygen.

$$\nabla \cdot (c\mathbf{U}Y_i) = -\nabla \cdot \mathbf{N}_i + S_{m,i} \tag{32}$$

where $\mathbf{N}_i$ is the molar diffusion flux of species i and $S_{m,i}$ is the source term due to the electrochemical reaction for species i Eq. (31).

Gas diffusion is influenced by the electrochemical reaction at the solid surfaces of the 3PBs. The mass diffusion is complex, especially within this porous region [2]. Apart from molecular diffusion which is dominant for large pore sizes and high pressure systems in the electrodes, Knudsen diffusion is also present and becomes significant when the mean-free path of the species is larger than the pore size [3]. Due to the combination of both molecular and Knudsen diffusion, an effective diffusion coefficient must be determined considering the aforementioned diffusion phenomena.

The molar diffusion flux, $\mathbf{N}_i$ in Eq. (32), can be calculated by Fick's law. However,

Fick's law is the simplest diffusion model, and it is only valid for a binary mixture, for a multicomponent mixture with invariable composition, for dilute mixtures or when the mass diffusion coefficient is independent of composition. As an SOEC operates under a mixture of at least four different gas species with variable composition, the Stefan-Maxwell (SMM) equations should, at least, be used if an accurate model is desired [3]. By the assumption that for ideal gases the Maxwell diffusion coefficients can be approximated by the binary diffusion coefficients, the Stefan-Maxwell equations can be written as [3, 47]:

$$\sum_{j=1, j\neq i}^{n} \frac{Y_j \mathbf{N}_i - Y_i \mathbf{N}_j}{D_{ij}^{B,\text{eff}}} = -\frac{p}{RT}\nabla Y_i - \frac{Y_i}{RT}\nabla p \tag{33}$$

where $D_{ij}^{B,\text{eff}}$ is the effective binary diffusion coefficient. Nonetheless, SMM only takes into account molecular diffusion. Yet, the Dusty gas model (DGM) appears to be a more suitable model for porous electrodes as it includes both the SMM formulation and Knudsen diffusion, Eq. (34).

$$\sum_{j=1, j\neq i}^{n} \frac{Y_j \mathbf{N}_i - Y_i \mathbf{N}_j}{D_{ij}^{B,\text{eff}}} + \frac{\mathbf{N}_i}{D_i^{K,\text{eff}}} = -\frac{p}{RT}\nabla Y_i - \frac{Y_i}{RT}\left(1 + \frac{K_0 p}{\mu D_i^{K,\text{eff}}}\right)\nabla p \tag{34}$$

where $D_{ij}^{K,\text{eff}}$ is the effective Knudsen diffusion coefficient.

An accurate evaluation of the effective diffusion coefficients is noteworthy for understanding gas transport mechanisms and their limitations as well as for a proper evaluation of the transport phenomena at a continuum level. Characterization parameters of the porous electrodes, e.g., porosity, tortuosity, particle size distribution, etc., are valuable input for calculation of these effective transport properties [48]. The effective diffusion coefficient, as well as for other transport properties, is usually calculated via Eq. (35).

$$D_{ij}^{B,\text{eff}} = \frac{\varepsilon}{\tau^2} D_{ij}^B \tag{35}$$

where ε is the electrode porosity, τ the tortuosity and D_{ij}^B the binary diffusion coefficient.

The porosity values for the electrodes are stated in Table 3 while the tortuosity is implemented as [43, 48, 49]:

$$\tau = (1 - \varepsilon)^{\frac{2-2D_s}{2-D_s}} \tag{36}$$

where D_s is the fractal dimension scale of pore-solid interface and set to 1.2 [43].

The binary diffusion coefficient, D_{ij}^B, can be evaluated by the kinetic theory of gases applying the Chapman-Enskog theory [10].

$$D_{ij}^B = D_{ji}^B = \frac{3.198 \cdot 10^{-8} T^{1.75}}{p \left(v_i^{1/3} + v_j^{1/3} \right)^2} \left(\frac{1}{M_i} + \frac{1}{M_j} \right)^{1/2} \tag{37}$$

where T is the temperature, p the pressure, M_i and M_j are the molar masses of the gas component i and j, respectively, and v_i and v_j the diffusion volumes of component i and j, respectively. The diffusion volumes were obtained from [10] and are specified in Table 3.

The Knudsen diffusion coefficient, D_i^K, is defined as follows [50].

$$D_i^K = \frac{d_p}{3} \sqrt{\frac{8RT}{\pi M_i}} \tag{38}$$

where d_p is the mean pore diameter. The corresponding mean pore diameters of the electrodes used are stated in Table 3.

Other gas transport models have been reported in literature for modeling solid oxide electrochemical cells, mainly SOFCs, like the binary friction model (BFM) [51–53] and the cylindrical pore interpolation model (CPIM) [53, 54]. Despite the different available

methods, Fick's model and the SMM are, by far, the most frequently used when modeling solid oxide electrochemical cells [25, 55–59].

Due to the computational cost and simplicity, several authors in literature use the Bosanquet formula, Eq. (39), to account for both molecular and Knudsen diffusion in Fick's model or in SMM instead of the DGM [24, 57, 58, 60]. The main problem of this simplification is, as Bertei and Nicolella [61] point out, the limitation of the Bosanquet formula which is only valid under the following conditions [62]: binary mixture, isobaric conditions and no net change in the number of moles. These are conditions which are not fulfilled in an SOC. Moreover, most of the commercial multiphysics softwares, e.g. Comsol Multiphysics or Ansys Fluent, omit Knudsen diffusion for minimizing the computational cost and thus, only consider Fick's model or SMM for species diffusion in porous media.

$$\frac{1}{D_{ij}^{\text{eff}}} = \frac{1}{D_{ij}^{B,\text{eff}}} + \frac{1}{D_i^{K,\text{eff}}} \tag{39}$$

Despite the limitations of the Bosanquet formula discussed by Bertei and Nicolella [61], this equation has been used in the work to take into account both molecular and Knudsen diffusion.

2.5 Heat transfer

An SOEC is a complex device in terms of heat transfer. Different heat transfer mechanisms dominate at the different cell components. Furthermore, heat generation or consumption is also present and is function of the operating voltage and temperature itself. Heat transfer within an SOEC consists of conduction, convection and radiation. Conduction takes place in the solids of the cell (electrolyte, interconnects and electrodes), while convection occurs via the flowing gas. Radiation is also present within the electrolyte-electrode structure and surface to surface radiation in the fuel and air channels.

A former study demonstrated that radiative heat transfer inside the cell could be neglected ahead of conductive heat transfer in an SOFC [63]. Examples of other models where radiation effects are neglected can be found in the literature [16, 17, 24]. Nevertheless, radiation can be considered for future studies of cell stacks as according to Hartvigsen *et al.* [64], its effect has been found to play a major role in determining the thermal condition of the cell stack and must be considered for accurate determination of temperature distributions. Yet, radiation has been neglected in the simulated model to avoid a high degree of complexity in the system.

As energy must be conserved throughout the whole computational domain, the energy conservation equation must be applied, Eq. (40).

$$\nabla \cdot (\rho c_p \mathbf{U} T) = \nabla \cdot (k \nabla T) + S_T \tag{40}$$

where c_p is the specific heat at constant pressure and k is the thermal conductivity of the medium. S_T is the thermal source term, which takes into account the heat from the electrochemical reactions and the polarizations and is defined as follows [12, 60]

$$
S_T = \begin{cases} 0 & \text{in gas channels} \hspace{1cm} (41) \\ \dfrac{i^2}{\sigma} & \text{in electrochemical inactive areas} \hspace{1cm} (42) \\ \dfrac{i^2}{\sigma} + j\left(\eta + \dfrac{T\Delta S}{2F}\right) & \text{in electrochemical active areas} \hspace{1cm} (43) \end{cases}
$$

where i is the current density, j the volumetric current density, σ the electric conductivity of the material, ΔS the entropy change for the reaction and η is the overpotential.

The entropy change term for each electrochemical half-reaction is implemented by Eq. (44), for which data is available.

$$\Delta S = n_e F \frac{\partial \pi^{\text{eq}}}{\partial T} = -\frac{\partial \Delta G}{\partial T} \tag{44}$$

At the high operating temperatures that solid oxide electrochemical cells work, all gas mixtures can be treated accurately as mixtures of ideal gases [45]. This entails a temperature dependency of the heat capacities but not of the pressure. Hence, the molar heat capacity at constant pressure for an ideal gas mixture of n components is described by Eq. (45) [45].

$$c_p(T) = \sum_{i=1}^{n} Y_i c_{pi}(T) \tag{45}$$

where c_{pi} $[\mathrm{kJ\,kmol^{-1}\,K^{-1}}]$ is the heat capacity for the component i. c_{pi} is implemented as a temperature dependent polynomial function by Eq. (46). The coefficients b_k are stated in [46]. The temperature T is in $[\mathrm{K}]$.

$$c_{pi} = \sum_{k=0}^{6} b_k \left(\frac{T}{1000} \right)^k \tag{46}$$

For a mixture of gases at low pressure, typical operation conditions for SOCs, the thermal conductivity of the mixture, k_m, can be calculated via the Wassileja equation with Einstein's summation convention, Eq. (47), together with the Mason and Saxena modification, Eqs. (48) and (49) [45].

$$k_m = \frac{Y_i k_i}{Y_j B_{ij}} \tag{47}$$

$$B_{ij} = \frac{\zeta \left[1 + \left(\frac{k_{tri}}{k_{trj}} \right)^{\frac{1}{2}} \left(\frac{M_i}{M_j} \right)^{\frac{1}{4}} \right]^2}{\left[8 \left(1 + \frac{M_i}{M_j} \right) \right]^{\frac{1}{2}}} \tag{48}$$

$$\frac{k_{tri}}{k_{trj}} = \frac{\mu_i}{\mu_j} \frac{M_j}{M_i} \tag{49}$$

where ζ is a constant set to unity and k_i is the thermal conductivity of species i. ζ is a factor that was proposed by Mason and Saxena and initially was equal to 1.065 for calculating the function B_{ij}, Eq. (48), but subsequently was set to unity by the same authors as it did not represent much loss in the overall accuracy [65]. The thermal conductivity for each component i is implemented as a temperature dependent polynomial function as stated in [46].

3   Experimental

To validate the model and calibrate the unknown parameter of the model, a number of cell test experiments have been performed with different gas mixtures at different temperatures.

The cell tests have all been done on planar supported SOCs produced by Haldor Topsoe A/S, and current-voltage measurements were performed at DTU Energy. A schematic drawing of the cell with all the components considered in the multiphysics model is shown in Figure 3. The cell has a nickel-yttria-stabilized zirconia (Ni-YSZ) support (porous support in Figure 3), a Ni-YSZ active layer (fuel electrode in Figure 3), a YSZ electrolyte and a lanthanum strontium cobalt ferrite (LSCF)-based oxygen electrode, a gadolinia doped ceria (CGO) barrier layer is present between the electrolyte and the LSCF-based electrode plus a contact layer. The thicknesses of the different components are stated in Table 1.

A cell of 53 mm x 53 mm with an active area of 40 mm x 40 mm is mounted into a cell test rig. The contacting of the cell is with corrugated nickel and gold meshes for the fuel and oxygen electrodes respectively, which provide a uniform contacting and gas distribution. The flow configuration in the cell test rig is shown in Figure 4.

A number of current density-voltage (*i*-V) measurements were performed with different H_2/H_2O compositions with air as oxidant gas and at temperatures ranging from 650 to 850 °C. An overview of the different inlet temperatures, flows and compositions (partial pressure of H_2) for these measurements are specified in Table 2.

21
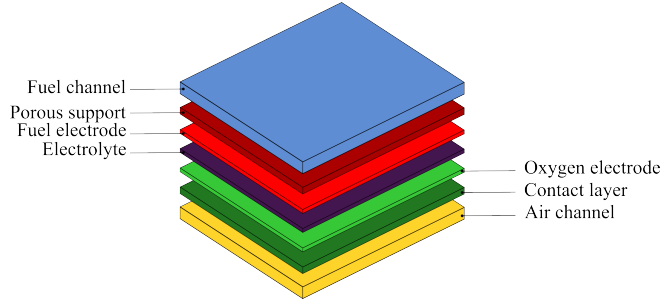
Figure 3: *Schematic drawing of the Haldor Topsoe A/S cell with its components.*

Table 1: *Cell layer thicknesses used in the multiphysics model.*

Parameter	Value [μm]
Gas channel height	800
Porous support layer thickness	300
Fuel electrode layer thickness	10
Electrolyte thickness	~ 15
Oxygen electrode layer thickness	30
Contact layer thickness	30

4 Validation

In this section, two different validation studies are presented by using the model presented in Section 2 to model the experimental setup presented in Section 3. First, an extensive current-voltage (*i*-V) curves comparison between the simulated and the experimental data is shown. Then, focus is set on evaluating the impact of considering the thermal effects on different cell operating parameters.

To model the setup in Section 3 different considerations have been made.

- Due to the flows configuration (see Figure 4) a symmetry plane can be drawn for
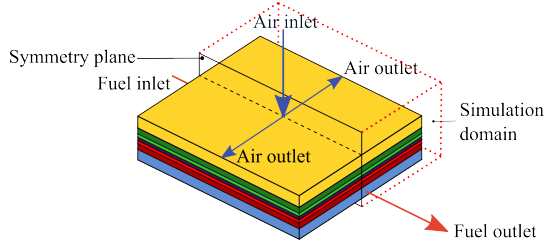
Figure 4: *Experimental setup arrangement with flow configuration and indication of the simulation domain.*

Table 2: *Inlet conditions for H_2/H_2O tests.*

Test	Temperature [°C]	Air flow $[\mathrm{L\,h^{-1}}]_{\mathrm{STP}}$	Fuel flow $[\mathrm{L\,h^{-1}}]_{\mathrm{STP}}$	$p_{\mathbf{H_2}}$ [atm]
1	700	140	24	0.5
2	750	140	24	0.5
3	800	140	24	0.5
4	700	140	25	0.96
5	750	140	25	0.96
6	850	140	25	0.96

the air inlet, reducing the simulation domain to a half. The flow geometry can thus be considered to be cross-flow over a $20\,\mathrm{mm}$ x $40\,\mathrm{mm}$ area.

- The current is collected by meshes on either side, as described in Section 3, and a reasonable assumption in the model is therefore that the current collection occurs evenly across both electrode surfaces.

- To account for the CGO barrier layer, which has not been modeled, the electrolyte thickness modeled is the sum of both the electrolyte and the CGO barrier layer thicknesses, see Table 1. Moreover, the conductivity is adjusted to match the ohmic resistance obtained via impedance measurements.

- The density of the gases is kept constant throughout the domain.

Table 3: *Cell parameters used in the multiphysics model.*

Parameter	Value	Units
Operating pressure (p)	1	atm
Fuel electrode porosity (ε)	0.3	—
Oxygen electrode porosity (ε)	0.20	—
Fuel or oxygen electrode permeability (K_0)	$1 \cdot 10^{-13}$	m^2
YSZ ionic conductivity (σ_{YSZ})	$\frac{100}{10^{4.9\frac{1000}{T}-3.30}}$ [66]	$\mathrm{S\,m^{-1}}$
Ni electronic conductivity (σ_{Ni})	$2.2 \cdot 10^6$	$\mathrm{S\,cm^{-1}}$
LSCF electronic conductivity $(\sigma_{\mathrm{LSCF,el}})$	$2 \cdot 10^3$	$\mathrm{S\,cm^{-1}}$
LSCF ionic conductivity $(\sigma_{\mathrm{LSCF,io}})$	0.2	$\mathrm{S\,cm^{-1}}$
CGO electronic conductivity (σ_{CGO})	0.07	$\mathrm{S\,cm^{-1}}$
LSCF volume fraction (χ_{LSCF})	0.5	—
Ni volume fraction (χ_{Ni})	0.26	—
YSZ volume fraction (χ_{YSZ})	$1 - \varepsilon - \chi_{\mathrm{Ni}}$	—
Ni tortuosity (τ_{Ni})	2.8	—
YSZ tortuosity (τ_{YSZ})	1.5	—
H_2 diffusion volume $\left(\upsilon_{\mathrm{H_2}}\right)$	$6 \cdot 10^{-6}$ [10]	$\mathrm{m^3\,mol^{-1}}$
H_2O diffusion volume $\left(\upsilon_{\mathrm{H_2O}}\right)$	$1.27 \cdot 10^{-5}$ [10]	$\mathrm{m^3\,mol^{-1}}$
O_2 diffusion volume $\left(\upsilon_{\mathrm{O_2}}\right)$	$1.66 \cdot 10^{-5}$ [10]	$\mathrm{m^3\,mol^{-1}}$
N_2 diffusion volume $\left(\upsilon_{\mathrm{N_2}}\right)$	$1.79 \cdot 10^{-5}$ [10]	$\mathrm{m^3\,mol^{-1}}$
H_2O reduction reaction activation energy $(E_{a,red})$	105.04 [67, 68]	$\mathrm{kJ\,mol^{-1}}$
Oxidation reaction activation energy $(E_{a,ox})$	123 [69]	$\mathrm{kJ\,mol^{-1}}$
Polarization resistance factor reduction reaction $(R_{0,red})$	$5 \cdot 10^{-12}$	$\Omega\,\mathrm{cm}^2$
Polarization resistance factor oxidation reaction $(R_{0,ox})$	$1.25 \cdot 10^{-12}$	$\Omega\,\mathrm{cm}^2$
Alumina block thickness $\left(t_{\mathrm{Al_2O_3}}\right)$	4	cm

Main boundary conditions

The main boundary conditions considered in the multiphysics model to model the experimental setup are shown in Figure 5. Unless specified, all other boundaries are electric insulated.
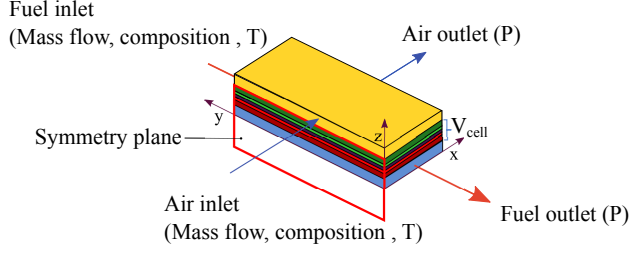
Figure 5: *Main boundary conditions.*

Moreover, a heat flux boundary condition is specified to these boundaries to take into the account the effect from the furnace at 750 °C where the cell is mounted surrounded by alumina (Al_2O_3) blocks, Eq. (50).

$$q_{\text{furnace}} = \frac{k_{Al_2O_3}}{t_{Al_2O_3}} \left(T_{\text{furnace}} - T\right) \tag{50}$$

where q_{furnace} is the heat from the furnace to the cell in $[\text{W m}^{-2}]$, $k_{Al_2O_3}$ the thermal conductivity of alumina, t the thickness of the alumina blocks surrounding the cell (4 cm), T_{furnace} is the furnace temperature and T, the cell temperature (at the boundary of the simulation domain).

The conductivity of alumina can be expressed as function of temperature, Eq. (51) [70, 71].

$$k_{Al_2O_3} = 5.5 + 34.5 \exp\left(-0.0033\left(T - 273\right)\right) \tag{51}$$

where $k_{\mathrm{Al_2O_3}}$ is in $[\mathrm{W\,m^{-1}\,K^{-1}}]$ and T is in $[\mathrm{K}]$. Equation (51) is valid for temperatures between 25 and 1300 °C.

4.1 Validation against *i*-V curves

A way to validate a computational model is by comparing *i*-V curves, simulated data versus experimental data. A wide range of tests have been performed in order to be able to validate the model under different flow rates, compositions and temperatures. In order to fit the computational model to the experimental data, where the only fitting parameter is the pre-exponential factor of the activation polarization resistance of the fuel electrode, $R_{0,\mathrm{red}}$, a sufficient number of experiments are required. To do so, *i*-V measurements are carried out when fixing one boundary condition, i.e. fuel composition while varying others, i.e. the inlet gas temperature.

The inlet conditions are those specified previously in Table 2 while all the parameters required for performing the simulations are defined in Table 3.

Figure 6 presents the different *i*-V curves, from experiments and simulations, for the H_2/H_2O system when operating under electrolysis and fuel cell mode at temperatures ranging from 700 to 800 °C at 50 % H_2. Inlet flow rates and compositions are kept constant for all temperatures as noted in Table 2, tests 1-3. Results show a very good agreement between the experimental and the simulated data at all the different temperatures tested as the maximum deviation with respect to the cell voltage is found to be 1.3 %.

Despite the good results regarding temperature variation, other tests are required to check the validity of the multiphysics model under different compositions and flow rates. Figure 7 shows the *i*-V curves comparison for the cell operating only in fuel cell mode for a 96 % H_2/4 % H_2O feedstock at three different temperatures. As pointed out in Table 2 tests 4-6, different flow rates and compositions for the fuel side are used compared to the ones used in Figure 6. Results show again a reasonable agreement between simulated and experimental data with the highest deviation with respect to the
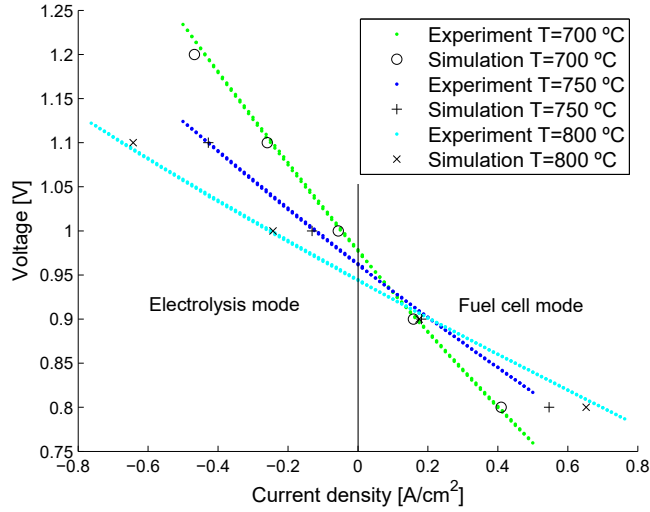
Figure 6: *i-V curves comparison for 24* $[\mathrm{L\,h^{-1}}]_{\mathrm{STP}}$ *H_2/H_2O at 50 % H_2 under electrolysis and fuel cell mode at different gas inlet temperatures. Negative and positive current densities correspond to electrolysis mode and fuel cell mode operation, respectively.*

cell voltage being 6 % at 700 °C. Moreover, Figure 7 reveals that the multiphysics model captures the thermodynamics well. It should be pointed out that despite the good agreement between the experimental and simulated data, the activation energies for the different physical phenomena providing the dependency with temperature in the cell are not completely accurate, and this deserved more research.

Due to the good match of the *i*-V curves under different operation modes, compositions, fuel flow-rates and temperatures for the H_2/H_2O feedstock, the developed 3D multiphysics model is trustworthy and a valuable tool for understanding and improving the solid oxide electrochemical cell technology. Besides, due to the physical phenomena included, the detailed potential and overpotential distribution through the cell, the use of microstructure data from FIB-SEM reconstruction as well as the use of impedance data, the model presented is the state-of-the-art for studying degradation phenomena. Navasa *et al.* have further used the described model for studying carbon deposition in SOEC
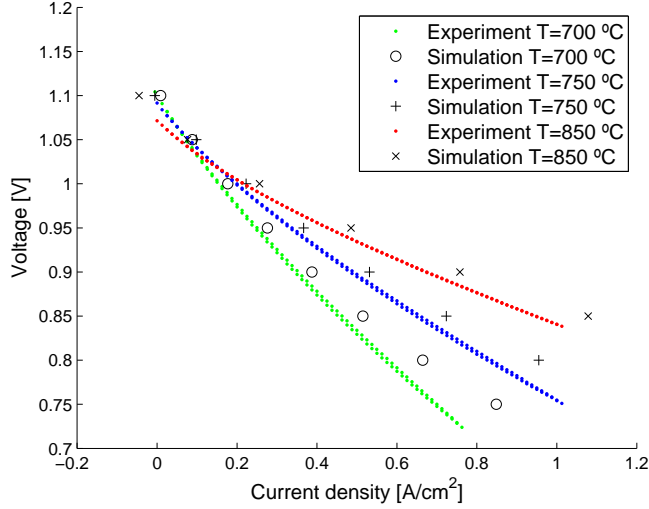
Figure 7: *i-V curves comparison for 24* $[\mathrm{L\,h}^{-1}]_{\mathrm{STP}}$ *H_2/H_2O at 96 % H_2 under fuel cell mode at different gas inlet temperatures.*

running with CO/CO_2 as feedstock [72].

4.2   Impact of including thermal effects

A sensitivity test is performed to validate the quality of the previously described model and the impact of including heat transfer. First, the distribution of certain operating parameters, i.e. partial pressure, temperature, current density and potentials, is analyzed at one specific cell voltage. Afterwards, the variation of these parameters as a function of the cell operating voltage is investigated. Moreover, the impact of considering thermal effects or not is evaluated by its effects on the *i*-V curve.

Figure 8 shows the distribution of the conditions in the cell at a cell operating voltage of 1.1 V at 750 °C and inlet $p_{\mathrm{H_2O}} = 0.5\ \mathrm{atm}$, corresponding to test 2 in Table 2, when thermal effects are included in the model. The operating cell voltage of 1.1 V, is onwards

referred to as the base case cell voltage. This corresponds to electrolysis operation mode (main focus of this study) in relatively mild conditions. Operating at high voltages, higher than the thermo-neutral cell voltage, can cause damage in the cell due to the high temperatures achieved.

At 750 °C, the thermo-neutral voltage $\left(V_{\mathrm{tn}} = \frac{\Delta H}{2F}\right)$ for the H_2/H_2O feedstock is 1.285 V. This is the cell voltage where the net heat flux of the cell is zero. In other words, the thermal needs of the endothermic electrochemical reaction are balanced by Joule heating from conduction. At voltage values lower than the thermo-neutral voltage, the heat requirement from the electrochemical reaction is dominant resulting in an endothermic cell behavior. On the contrary, at voltages above the thermo-neutral point, Joule heating dominates resulting in a positive net heat flux and an exothermic behavior of the electrolytic cell.

Figure 8a shows the temperature profiles at the fuel inlet (top figure) and outlet (bottom figure) for 1.1 V. As the base case voltage corresponds to a cell voltage below the thermo-neutral voltage, an endothermic behavior is expected. As it can be observed, the thermodynamics are obeyed as an endothermic profile is obtained by maximum of 8 °C decrease in temperature along the flow direction, difference between the inlet and outlet figures. The lowest temperature value achieved is at the lower right corner, corresponding to the fuel and air outlet, as this is the air outlet, where the air has been cooled over the entire cell (air flows from $x = 0$ cm to $x = 2$ cm). If the cell was thermally insulated, i.e., adiabatic conditions, a larger temperature gradient would be observed due to that the heat consumption by the electrochemical reactions would not be reduced by an external heat supply. This gradient is quantified and found to be about 22 °C in comparison to the 8 °C difference when the furnace supplies heat to the cell.

Figure 8b shows the current density distribution at the interface between the active and the diffusion layers of the fuel electrode in absolute values. The highest current density values are achieved at the right top corner, which corresponds to the fuel inlet ($y = 4$ cm) and air outlet ($x = 2$ cm). Current density values follow the same tendency as temperature as they decrease along the flow directions being lowest at the fuel and air outlet due to endothermic thermal conditions.

(a) *Temperature distribution*

(b) *Current density distribution*

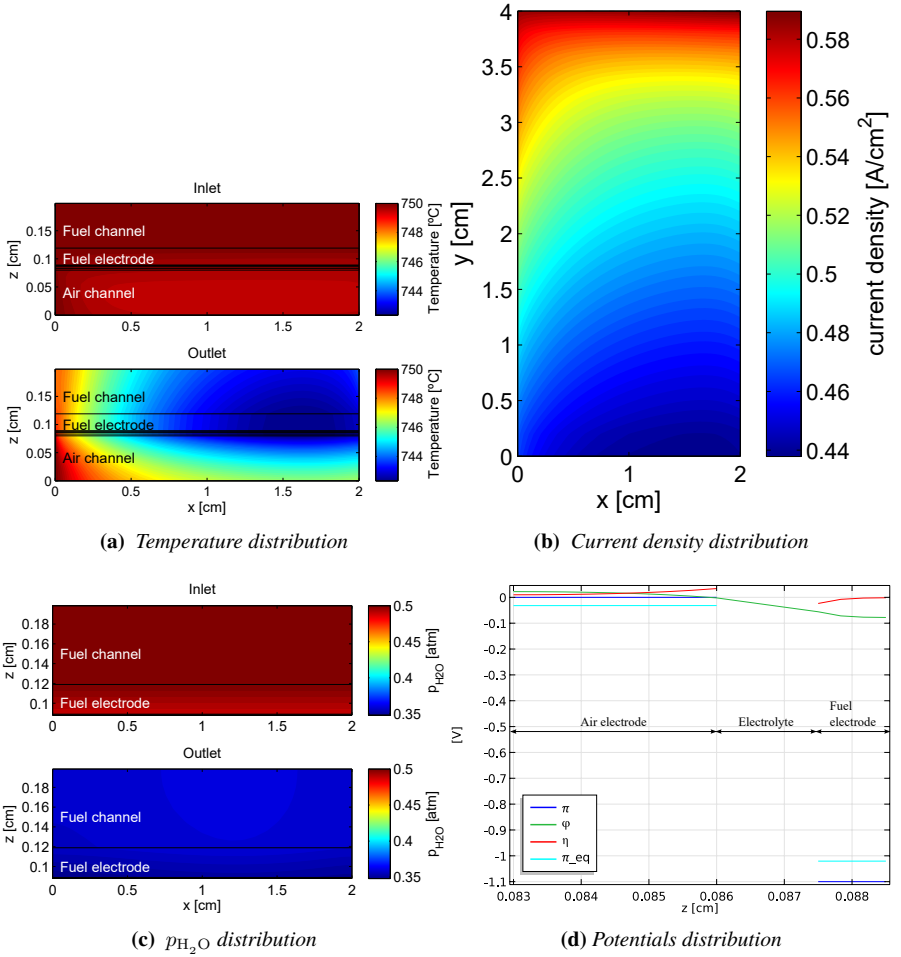**(c)** p_{H_2O} *distribution*

(d) *Potentials distribution*

Figure 8: p_{H_2O} *and temperature distribution at the fuel inlet and outlet, current density distribution at the active/diffusion layer fuel electrode interface and potentials distribution through the cell operating at 1.1 V, $p_{H_2O} = 0.5$ atm and 750 °C.*

30

The partial pressure distribution of H_2O at the fuel inlet (top figure) and at the fuel outlet (bottom figure) is shown in Figure 8c. At 1.1 V the fuel utilization achieved under the previously defined conditions is 24 %. Moreover, a homogeneous species distribution is observed in the x direction, while the effects of diffusion in porous media through the fuel electrode (z direction) can be slightly observed at the fuel outlet.

The different potentials distribution through the cell electrodes and electrolyte are shown in Figure 8d. Showing the same trend as the generic Figure 2 but for 1.1 V. The difference of the electromotive potentials gives the cell voltage and this can be read from the figure as the $\pi_{\text{air}} = 0$ V while $\pi_{\text{fuel}} = -1.1$ V. Following the same procedure, and as specified by Eq. (13), the cell open circuit voltage is a around 1 V. Moreover, the Galvani potential (ϕ) is also shown. The Galvani potential decreases along the cell thickness from left to right due to the contributions from the different ohmic resistances from the different cell components. Last, the overpotential (η) at both electrodes is presented. The overpotential presents higher values close to the electrolyte for both electrodes, at the electrode active layers, as it is the region where the electrochemical reactions take place.

4.2.1 Effect of the operating cell voltage

The effect of varying the operating cell voltage on the partial pressure of H_2O, the overpotential distribution as well as for the temperature has been studied for four different cell voltages when operating at $750\,^\circ\text{C}$ and $p_{H_2O} = 0.5\,\text{atm}$. One cell voltage corresponds to the cell operating in fuel cell mode (0.9 V) while the other three voltages correspond to the electrolysis operation mode. 1.1 V is below the thermo-neutral voltage, 1.3 V is close to the thermo-neutral voltage and 1.5 V, above the thermo-neutral voltage. This covers the different thermal behaviors under electrolysis operation mode.

Figure 9a shows the H_2O partial pressure distribution along the fuel flow direction for the four aforementioned cell voltages. Only the distribution along the flow direction is shown as the variation is more significant here as seen in Figure 8c. The fuel inlet is located at $y = 4$ cm, where the inlet partial pressure is set to $p_{H_2O} = 0.5$ atm and the

fuel outlet at $y = 0$ cm. In fuel cell mode (0.9 V), the partial pressure of H_2O increases as steam is produced apart from electricity. Yet, the fuel utilization at this voltage is very low, as it is very close to the equilibrium cell voltage, cell voltage where the current density is zero and thus, no electrochemical reaction takes place. In electrolysis mode, one can observe that lower H_2O partial pressures are achieved at the fuel outlet with increasing voltage. The higher the operating voltage, the higher the current density and consequently, the fuel utilization. Fuel starvation can be observed at 1.5 V as H_2O is totally consumed before the cell outlet is reached. A 86 % fuel utilization is attained at 1.5 V in comparison to 60 % at 1.3 V and 24 % at 1.1 V.

Figure 9b presents the overpotential distribution through the air electrode (left), electrolyte and fuel electrode (right) at the four different cell voltages at the fuel and air outlet. In general, higher cell voltages result in higher overpotentials as observed. Moreover, higher overpotential voltages are observed close to the electrolyte, at the active electrode regions, as it is where the electrochemical reactions take place due to higher current densities achieved. For 1.5 V, the overpotential does not follow the general trend as it tends to 0 V at the air side and is close to 0 V at the electrolyte/fuel electrode interface and increases through the electrode. This behavior is due to fuel starvation taking place at such high voltage. When fuel starvation occurs, no electrochemical reaction will occur in electrolysis mode, as there is no fuel left to react. As a result, the overpotential will be zero and no increase in current density will be observed. The behavior of the fuel electrode overpotential under starvation seen in Figure 9b is due to gas diffusion limitations as a result of fuel scarcity. Hence, most of the reaction will occur where there is a bit of reactant left, i.e., at the gas channels, and therefore, the increasing overpotential at the fuel electrode/diffusion layer interface.

Effect of temperature

As above-mentioned, an electrolysis cell shows different thermal behaviors as function of the operating cell voltage, as the cell can be run below, above or at the thermo-neutral voltage. Figure 9c shows the temperature profiles at the fuel outlet for the four specified voltages. From top to bottom, the different temperature profiles are shown

p_H2O [atm]

0.6
0.55
0.5
0.45
0.4
0.35
0.3
0.25
0.2
0.15
0.1
0.05
0

0   0.01   0.02   0.03   0.04
y [cm]

V = 0.9 V
V = 1.1 V
V = 1.3 V
V = 1.5 V

η[V]

0.07
0.06
0.05
0.04
0.03
0.02
0.01
0
-0.01
-0.02
-0.03
-0.04
-0.05
-0.06

Air electrode   Electrolyte   Fuel electrode

0.083   0.084   0.085   0.086   0.087   0.088
z [cm]

V = 0.9 V
V = 1.1 V
V = 1.3 V
V = 1.5 V

(a) $p_{\mathrm{H_2O}}$ *profile*

(b) *Overpotential profile*

V=0.9 V

z [cm]
0.15
0.1
0.05
0

Fuel channel

Air channel

0   0.2   0.4   0.6   0.8   1   1.2   1.4   1.6   1.8   2

V=1.1 V

z [cm]
0.15
0.1
0.05
0

Fuel channel

Air channel

0   0.2   0.4   0.6   0.8   1   1.2   1.4   1.6   1.8   2

V=1.3 V

z [cm]
0.15
0.1
0.05
0

Fuel channel

Air channel

0   0.2   0.4   0.6   0.8   1   1.2   1.4   1.6   1.8   2

V=1.5 V

z [cm]
0.15
0.1
0.05
0

Fuel channel

Air channel

0   0.2   0.4   0.6   0.8   1   1.2   1.4   1.6   1.8   2
x [cm]

744   746   748   750   752   754   756   T [°C]

(c) *Temperature at the fuel outlet*

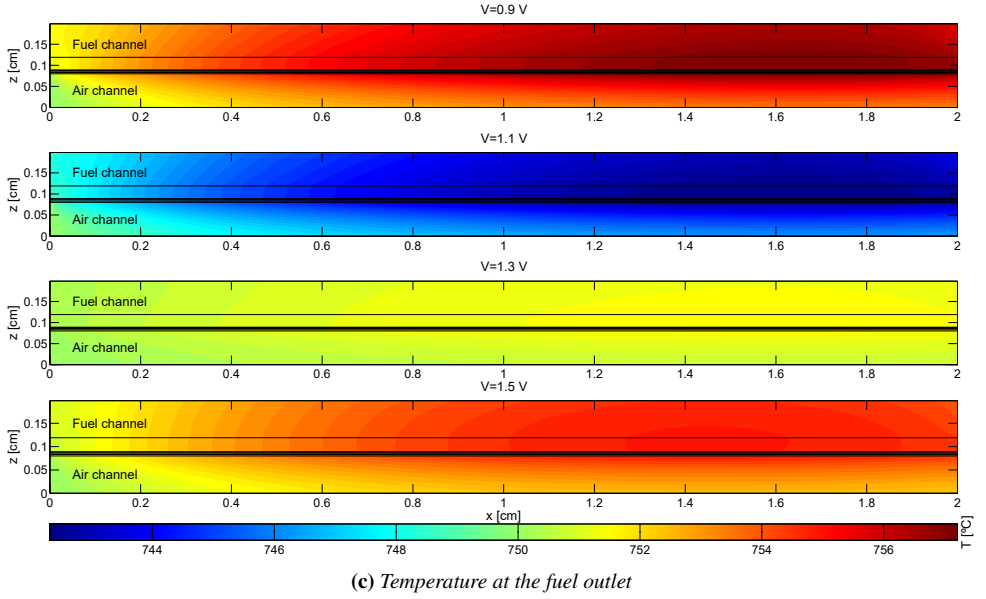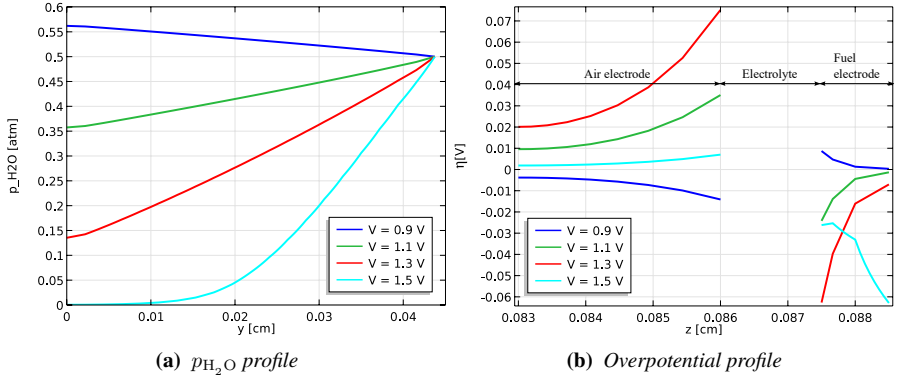**Figure 9:** $p_{\mathrm{H_2O}}$ *profile along the fuel direction, overpotential distribution through the cell and temperature distribution at the fuel outlet for four different cell voltages at* $p_{\mathrm{H_2O}} = 0.5$ atm *and* $750\,°C$.

for increasing cell voltage. At 0.9 V the cell operates in fuel cell mode, which should present an exothermic behavior as the general electrochemical reaction for hydrogen is exothermic plus the contribution from Joule heating always results in a positive net heat flux. This is confirmed by a temperature increase of about 8 °C along the flow direction. At 1.1 V, a cell voltage below the thermo-neutral point, the cell behaves as endothermic under electrolysis mode and a temperature decrease of 8 °C was observed as described previously in detail in Figure 8a despite the heat supplied from the furnace. The temperature profile at a cell voltage very close to the thermo-neutral voltage, 1.3 V, voltage where the net heat transfer should be zero if no extra heat is supplied to the cell, shows a 2 °C temperature increase along the flow direction. Last, the temperature profile at 1.5 V, an operating voltage above the thermo-neutral point at 750 °C. Here, a temperature increase along the flow direction demonstrates the positive net heat flux. Although at higher cell voltages, and consequently higher current densities, higher fuel utilization is achieved and thus, more hydrogen is produced, the temperature gradient should not be too large for not damaging the cell. Yet, due to fuel starvation close to the cell outlets at this voltage, the temperature gradient at the outlet of the cell channel is only 5 °C as there is no contribution from the electrochemical reactions.

From all the evaluated temperature profiles, it can be stated that the basic thermodynamics are not violated and the thermal behavior is as expected for a solid oxide electrochemical cell operating in both fuel cell and electrolysis mode for a H_2/H_2O feedstock.

Moreover, the effect of heat transfer on the i-V curve has been evaluated by comparing when thermal effects are included with when heat transport and generation are neglected, i.e., uniform temperature distribution. The i-V curves are displayed for the 50 %H_2/50% H_2O feedstock with an inlet temperature of 750 °C in Figure 10. Including thermal effects has its effects at high cell voltages before reaching the starvation regime. At high cell voltages, higher current densities are achieved when heat transfer is considered than with uniform temperature distribution, and this influences all other transport phenomena that take place in the cell, as an SOC is a complex device where all the transport phenomena are coupled.
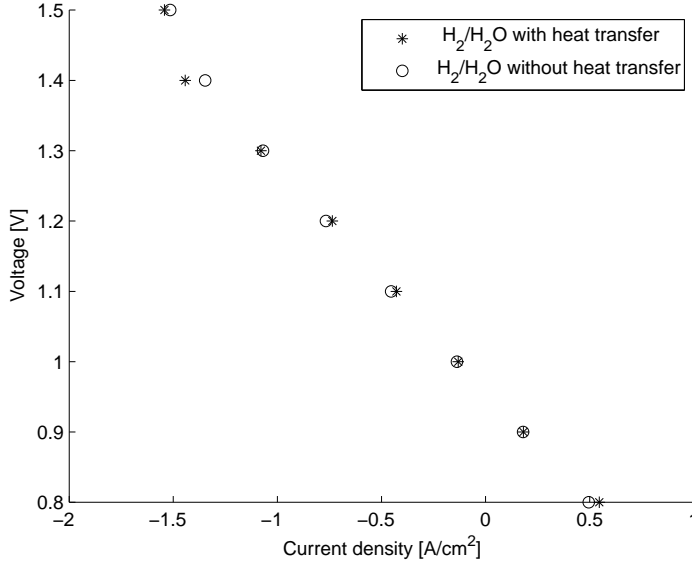
Figure 10: *Comparison of i-V curves with and without heat transfer at* $p_{H_2O} = 0.5$ atm *and 750 °C.*

5   Discussion

The 3D SOC multiphysics model developed presents very good agreement with the experimental data. Thus, one can expect reliable results when operating under the range of temperatures, compositions and flow rates tested. Although it should also be reliable at other operating conditions, further research is needed to investigate other experimental behaviors, especially conditions with starvation.

Yet, the purpose for developing this multiphysics model is for using it as a tool for studying degradation mechanisms in SOECs, main focus for the ongoing research. Having a computational model that can help understand and locate where certain degradation mechanisms take place in an SOC can be a great tool for improving cell performance and design and decreasing the experimental time and cost.

Despite having developed a useful multiphysics model, which has been extensively validated with success, there are still topics to be further investigated. Mass diffusion is one of the areas which deserve some attention. Especially the effect of Knudsen diffusion, which has been accounted by the Bosanquet formula in the SMM which provides some uncertainty. The influence of the DGM instead in this framework will be interesting as it would probably give better results in terms of species distribution and thus, overpotential distribution, etc.

6 Conclusions

In this work the mathematical equations needed for a three dimensional solid oxide electrochemical cell model including heat, mass, species and momentum transfer and transport of charged species together with a detailed model of the electrochemical reactions have been presented. The latter allows for a detailed description of the gas distributions, temperature and overpotential through the entire cell and in particular within the electrodes. This is highly relevant for studying various degradation phenomena.

The model has been thoroughly validated against cell tests experiments with cross-flows with H_2/H_2O mixtures as fuel for both fuel cell and electrolysis modes.

The experiment comprised variations in different temperature, flows and compositions was validated by comparison of i-V curves. The model presented very good agreement with the experimental data with a unifying set of model parameters, showing a correct interaction between physical phenomena in-spite of the complexity of the model.

Basic thermodynamics are also shown to be obeyed for the feedstock tested permitting the study of the different thermal modes solid oxide electrochemical cells undergo as a function of the operating cell voltage and the temperature distribution inside the cell. Moreover, the effect of the operating cell voltage on the different cell polarizations through the cell and the fuel partial pressure distribution have been studied.

The effect of considering heat transfer in the model in electrolysis mode is particularly

observed at high voltages, where the impact on the current density is noticeable, resulting in a higher hydrogen production due to higher current densities achieved.

With the current additions to the literature presented in this work, adds models which can onward be a strong tool for understanding and degradation and failure mechanisms of SOCs.

Acknowledgements

List of symbols

a_i	Chemical activity of species i, dimensionless
c	Molar density, $[\mathrm{mol\,m^{-3}}]$
c_p	Specific heat at constant pressure, $[\mathrm{J\,kg^{-1}\,K^{-1}}]$
D	Mass diffusion coefficient, $[\mathrm{m^2\,s^{-1}}]$
D_s	Fractal dimension scale of pore-solid interface, dimensionless
d_p	Mean pore diameter, $[\mathrm{m}]$
E_a	Activation energy, $[\mathrm{kJ\,mol^{-1}}]$
F	Faraday constant, $[\mathrm{C\,mol^{-1}}]$
G	Gibbs free energy, $[\mathrm{J\,mol^{-1}}]$
H	Enthalpy, $[\mathrm{J\,mol^{-1}}]$
i	Current density, $[\mathrm{A\,m^{-2}}]$
i_0	Exchange current density, $[\mathrm{A\,m^{-2}}]$
$\mathbf{J}$	Current density flux, $[\mathrm{A\,m^{-2}}]$
j	Volumetric current density, $[\mathrm{A\,m^{-3}}]$
K_0	Permeability of the porous medium, $[\mathrm{m^2}]$

k	Thermal conductivity, $[\mathrm{W\,m^{-1}\,K^{-1}}]$
M_i	Molar mass of species i, $[\mathrm{kg\,mol^{-1}}]$
$\mathbf{N}$	Molar flux of gas species, $[\mathrm{mol\,m^{-2}\,s^{-1}}]$
n	Number of species i in the gas mixture, dimensionless
n_e	Number of electrons transferred per reaction, dimensionless
P	Pressure, $[\mathrm{Pa}]$ or $[\mathrm{atm}]$
p_i	Partial pressure of species i, $[\mathrm{atm}]$
q	Heat source, $[\mathrm{W\,m^{-2}}]$
R	Ideal gas constant, $[\mathrm{J\,mol^{-1}\,K^{-1}}]$
R_0	Pre-exponential factor of the activation polarization resistance, $[\Omega\,\mathrm{cm^2}]$
S	Entropy, $[\mathrm{J\,mol^{-1}\,K^{-1}}]$
S_d	Source term for the momentum conservation equation, $[\mathrm{J\,m^{-3}\,s^{-1}}]$
S_m	Source term for the mass conservation equation, $[\mathrm{mol\,m^{-3}\,s^{-1}}]$
S_T	Source term for the energy conservation equation, $[\mathrm{J\,m^{-3}\,s^{-1}}]$
S_η	Source term for the charge transfer equation, $[\mathrm{A\,m^{-3}}]$
T	Temperature, $[\mathrm{K}]$
t	Thickness, $[\mathrm{\mu m}]$ or $[\mathrm{cm}]$
$\mathbf{U}$	Velocity vector, $[\mathrm{m\,s^{-1}}]$
V	Voltage, $[\mathrm{V}]$
v	Diffusion volume, $[\mathrm{m^3\,mol^{-1}}]$
$\mathbf{Y}_i$	Molar fraction of species i, dimensionless

Greek letters

α	Reduction/oxidation transfer coefficient, dimensionless
ε	Porosity of the electrodes, dimensionless
η	Electrochemical potential, $[\mathrm{J\,mol^{-1}}]$/ Overpotential, $[\mathrm{V}]$
μ	Chemical potential, $[\mathrm{J\,mol^{-1}}]$/ Dynamic viscosity, $[\mathrm{Pa\,s^{-1}}]$
π	Electromotive or Fermi potential, $[\mathrm{V}]$
ρ	Density, $[\mathrm{kg\,m^{-3}}]$
σ	Electric conductivity, $[\mathrm{S\,m^{-1}}]$
τ	Tortuosity, dimensionless

ϕ	Galvani potential, [V]
χ_i	Volume fraction of phase i in the electrode, dimensionless

Chemical species & compounds

Al_2O_3	Alumina or oxide (III)
CO	Carbon monoxide
CO_2	Carbon dioxide
e^-	Electron
H_2	Hydrogen
H_2O	Water
Ni	Nickel
N_2	Nitrogen
O_2	Oxygen
O^{2-}	Oxide ion

Abbreviations

1D/2D/3D	One, two or three dimensional
3PB	Triple-phase boundary
BFM	Binary friction model
CFD	Computational fluid dynamics
CGO	Gadolinium doped cerium oxide
CPIM	Cylindrical pore interpolation model
DGM	Dusty gas model
DTU	Technical University of Denmark
FEM	Finite element method
FIB	Focused ion beam
LSCF	Lanthanum strontium cobalt ferrite
SEM	Scanning electron microscope

SMM	Stefan-Maxwell model
SOC	Solid oxide electrochemical cell
SOEC	Solid oxide electrolysis cell
SOFC	Solid oxide fuel cell
STP	Standard temperature and pressure
YSZ	Yttria-stabilized zirconia

References

[1] S. Sohn, J. H. Nam, D. H. Jeon, and C.-J. Kim, "A micro/macroscale model for intermediate temperature solid oxide fuel cells with prescribed fully-developed axial velocity profiles in gas channels," *International Journal of Hydrogen Energy*, vol. 35, no. 21, pp. 11890–11907, 2010.

[2] J. H. Nam and D. H. Jeon, "A comprehensive micro-scale model for transport and reaction in intermediate temperature solid oxide fuel cells," *Electrochimica Acta*, vol. 51, no. 17, pp. 3446–3460, 2006.

[3] R. Suwanwarangkul, E. Croiset, M. W. Fowler, P. L. Douglas, E. Entchev, and M. A. Douglas, "Performance comparison of Fick's, dusty-gas and Stefan–Maxwell models to predict the concentration overpotential of a SOFC anode," *Journal of Power Sources*, vol. 122, no. 1, pp. 9–18, 2003.

[4] A. Kromp, H. Geisler, A. Weber, and E. Ivers-Tiffée, "Electrochemical impedance modeling of gas transport and reforming kinetics in reformate fueled solid oxide fuel cell anodes," *Electrochimica Acta*, vol. 106, pp. 418–424, 2013.

[5] E. Hernández-Pacheco, M. D. Mann, P. N. Hutton, D. Singh, and K. E. Martin, "A cell-level model for a solid oxide fuel cell operated with syngas from a gasification process," *International Journal of Hydrogen Energy*, vol. 30, no. 11, pp. 1221–1233, 2005.

[6] Q. Wang, L. Li, and C. Wang, "Numerical study of thermoelectric characteristics of a planar solid oxide fuel cell with direct internal reforming of methane," *Journal of Power Sources*, vol. 186, no. 2, pp. 399–407, 2009.

[7] F. N. Cayan, S. R. Pakalapati, F. Elizalde-Blancas, and I. Celik, "On modeling multi-component diffusion inside the porous anode of solid oxide fuel cells using Fick's model," *Journal of Power Sources*, vol. 192, no. 2, pp. 467–474, 2009.

[8] S. A. Hajimolana, M. A. Hussain, W. M. A. W. Daud, M. Soroush, and A. Shamiri, "Mathematical modeling of solid oxide fuel cells: A review," *Renewable & Sustainable Energy Reviews*, vol. 15, no. 4, pp. 1893–1917, 2011.

[9] H. Geisler, A. , A. Weber, and E. Ivers-Tiffée, "Stationary FEM Model for Performance Evaluation of Planar Solid Oxide Fuel Cells Connected by Metal Interconnectors: I. Model Framework and Validation," *Journal of Electrochemical Society*, vol. 161, no. 6, pp. F778–F788, 2014.

[10] W. Kong, H. Zhu, Z. Fei, and Z. Lin, "A modified dusty gas model in the form of a Fick's model for the prediction of multicomponent mass transport in a solid oxide fuel cell anode," *Journal of Power Sources*, vol. 206, no. 0, pp. 171–178, 2012.

[11] H. Yakabe, T. Ogiwara, M. Hishinuma, and I. Yasuda, "3D model calculation for planar SOFC," *Journal of Power Sources*, vol. 102, no. 1-2, pp. 144–154, 2001.

[12] V. M. Janardhanan and O. Deutschmann, "Numerical study of mass and heat transport in solid-oxide fuel cells running on humidified methane," *Chemical Engineering Science*, vol. 62, no. 18–20, pp. 5473–5486, 2007.

[13] E. Achenbach, "Three-dimensional and time-dependent simulation of a planar solid oxide fuel cell stack," *Journal of Power Sources*, vol. 49, no. 1-3, pp. 333–348, 1994.

[14] W. G. Bessler, S. Gewies, and M. Vogler, "A new framework for physically based modeling of solid oxide fuel cells," *Electrochimica Acta*, vol. 53, no. 4, pp. 1782–1800, 2007.

[15] W. Y. Lee, D. Wee, and A. F. Ghoniem, "An improved one-dimensional membrane-electrode assembly model to predict the performance of solid oxide fuel cell including the limiting current density," *Journal of Power Sources*, vol. 186, no. 2, pp. 417–427, 2009.

[16] K. Tseronis, I. S. Fragkopoulos, I. Bonis, and C. Theodoropoulos, "Detailed multi-dimensional modeling of direct internal reforming solid oxide fuel cells," *Fuel Cells*, vol. 16, no. 3, pp. 294–312, 2016.

[17] M. Ni, "Computational fluid dynamics modeling of a solid oxide electrolyzer cell for hydrogen production," *International Journal of Hydrogen Energy*, vol. 34, no. 18, pp. 7795–7806, 2009.

[18] M. Ni, "2D thermal modeling of a solid oxide electrolyzer cell (SOEC) for syngas production by H2O/CO2 co-electrolysis," *International Journal of Hydrogen Energy*, vol. 37, no. 8, pp. 6389–6399, 2012.

[19] M. Ni, M. K. H. Leung, and D. Y. C. Leung, "Mathematical modeling of the coupled transport and electrochemical reactions in solid oxide steam electrolyzer for hydrogen production," *Electrochimica Acta*, vol. 52, no. 24, pp. 6707–6718, 2007.

[20] J. Udagawa, P. Aguiar, and N. P. Brandon, "Hydrogen production through steam electrolysis: Model-based steady state performance of a cathode-supported intermediate temperature solid oxide electrolysis cell," *Journal of Power Sources*, vol. 166, no. 1, pp. 127–136, 2007.

[21] J. Udagawa, P. Aguiar, and N. P. Brandon, "Hydrogen production through steam electrolysis: Model-based dynamic behaviour of a cathode-supported intermediate temperature solid oxide electrolysis cell," *Journal of Power Sources*, vol. 180, no. 1, pp. 46–55, 2008.

[22] J. Udagawa, P. Aguiar, and N. P. Brandon, "Hydrogen production through steam electrolysis: Control strategies for a cathode-supported intermediate temperature solid oxide electrolysis cell," *Journal of Power Sources*, vol. 180, no. 1, pp. 354–364, 2008.

[23] Q. Cai, E. Luna-Ortiz, C. S. Adjiman, and N. P. Brandon, "The effects of operating conditions on the performance of a solid oxide steam electrolyser: A model-based study," *Fuel Cells*, vol. 10, no. 6, pp. 1114–1128, 2010.

[24] D. Grondin, J. Deseure, A. Brisse, M. Zahid, and P. Ozil, "Simulation of a high temperature electrolyzer," *Journal of Applied Electrochemistry*, vol. 40, no. 5, pp. 933–941, 2010.

[25] X. Jin and X. Xue, "Computational fluid dynamics analysis of solid oxide electrolysis cells with delaminations," *International Journal of Hydrogen Energy*, vol. 35, no. 14, pp. 7321–7328, 2010.

[26] J. Laurencin, D. Kane, G. Delette, J. Deseure, and F. Lefebvre-Joud, "Modelling of solid oxide steam electrolyser: Impact of the operating conditions on hydrogen production," *Journal of Power Sources*, vol. 196, no. 4, pp. 2080–2093, 2011.

[27] G. Hawkes, J. O'Brien, C. Stoots, and B. Hawkes, "3d CFD model of a multi-cell high-temperature electrolysis stack," *International Journal of Hydrogen Energy*, vol. 34, no. 9, pp. 4189–4197, 2009.

[28] J. S. Herring, J. E. O'Brien, C. M. Stoots, G. L. Hawkes, J. J. Hartvigsen, and M. Shahnam, "Progress in high-temperature electrolysis for hydrogen production using planar SOFC technology," *International Journal of Hydrogen Energy*, vol. 32, no. 4, pp. 440–450, 2007.

[29] J. E. O'Brien, M. G. McKellar, C. M. Stoots, J. S. Herring, and G. L. Hawkes, "Parametric study of large-scale production of syngas via high-temperature co-electrolysis," *International Journal of Hydrogen Energy*, vol. 34, no. 9, pp. 4216–4226, 2009.

[30] J. E. O'Brien, "Thermodynamics and Transport Phenomena in High Temperature Steam Electrolysis Cells," *Journal of Heat Transfer*, vol. 134, no. 3, pp. 031017–031017, 2012.

[31] T. Boëdec, M. Reytier, D. Lhachemi, D. Tschumperlé, P. Louat, S. Di Iorio, P. Baurens, and G. Delette, "A new stack to validate technical solutions and numerical simulations," *Fuel Cells*, vol. 12, no. 2, pp. 239–247, 2012.

[32] C. Chatzichristodoulou, M. Chen, P. V. Hendriksen, T. Jacobsen, and M. B. Mogensen, "Understanding degradation of solid oxide electrolysis cells through modeling of electrochemical potential profiles," *Electrochimica Acta*, vol. 189, pp. 265–282, 2016.

[33] D. A. Noren and M. A. Hoffman, "Clarifying the Butler–Volmer equation and related approximations for calculating activation losses in solid oxide fuel cell models," *Journal of Power Sources*, vol. 152, no. 0, pp. 175–181, 2005.

[34] P. Gellings and H. Bouwmeester, *The CRC Handbook of Solid State Electrochemistry*. Boca Raton, Fl: CRC press, 1997.

[35] M. Mogensen, H. Frandsen, J. Nielsen, W. Li, T. Jacobsen, and C. Graves, "Current density - overvoltage relations for solid oxide electrodes." Smart Energy Conversion and Storage Conference, Krynica, Poland, 2013.

[36] H. Chang and G. Jaffé, "Polarization in electrolytic solutions. part i. theory," *The Journal of Chemical Physics*, vol. 20, no. 7, pp. 1071–1077, 1952.

[37] A. Leonide, S. Hansmann, A. Weber, and E. Ivers-Tiffée, "Performance simulation of current/voltage-characteristics for sofc single cell by means of detailed impedance analysis," *Journal of Power Sources*, vol. 196, no. 17, pp. 7343–7346, 2011.

[38] H. Wendt and G. Kreysa, *Electrochemical Engineering*. Berlin: Springer, 1999.

[39] T. Jacobsen and M. Mogensen, "The course of oxygen partial pressure and electric potentials across an oxide electrolyte cell," *ECS Transactions*, vol. 13, no. 26, pp. 259–273, 2008.

[40] S. Kakaç, A. Pramuanjaroenkij, and X. Y. Zhou, "A review of numerical modeling of solid oxide fuel cells," *International Journal of Hydrogen Energy*, vol. 32, no. 7, pp. 761–786, 2007.

[41] K. N. Grew, A. S. Joshi, A. A. Peracchio, and W. K. S. Chiu, "Pore-scale investigation of mass transport and electrochemistry in a solid oxide fuel cell anode," *Journal of Power Sources*, vol. 195, no. 8, pp. 2331–2345, 2010.

[42] K. Kwok, P. S. Jørgensen, and H. L. Frandsen, "Computation of effective steady-state creep of porous ni–ysz composites with reconstructed microstructures," *Journal of the American Ceramic Society*, vol. 98, no. 9, pp. 2873–2880, 2015.

[43] G. Reiss, H. L. Frandsen, A. H. Persson, C. Weiß, and W. Brandstätter, "Numerical evaluation of oxide growth in metallic support microstructures of solid oxide fuel cells and its influence on mass transport," *Journal of Power Sources*, vol. 297, pp. 388–399, 2015.

[44] D. Young, B. Munson, T. Okiishi, and W. Huebesch, *Introduction to Fluid Mechanics*. John Wiley & Sons, 5 ed., 2012.

[45] B.E.Poling, J.M.Prausnitz, and J.P.O'Conell, *The Properties of Liquids & Gases*. New York: McGraw-Hill, 5 ed., 2000.

[46] B. Todd and J. B. Young, "Thermodynamic and transport properties of gases for use in solid oxide fuel cell modelling," *Journal of Power Sources*, vol. 110, no. 1, pp. 186–200, 2002.

[47] H. Merk, "The Macroscopic Equations for Simultaneous Heat and Mass Transfer in Isotropic, Continuous and Closed Systems," *Applied Sciences Research*, vol. A8, p. 26, 1959.

[48] J. Yuan and B. Sundén, "On mechanisms and models of multi-component gas diffusion in porous structures of fuel cell electrodes," *International Journal of Heat and Mass Transfer*, vol. 69, pp. 358–374, 2014.

[49] J. G. Liu and Y. F. Nie, "Fractal scaling of effective diffusion coefficient of solute in porous media," *Journal of Environmental Sciences*, vol. 13, no. 2, pp. 170–172, 2001.

[50] R. E. Cunningham and R. J. J. Williams, *Diffusion in Gases and Porous Media*. New York: Plenum Press, 1980.

[51] Y. Vural, L. Ma, D. B. Ingham, and M. Pourkashanian, "Comparison of the multi-component mass transfer models for the prediction of the concentration overpotential for solid oxide fuel cell anodes," *Journal of Power Sources*, vol. 195, no. 15, pp. 4893–4904, 2010.

[52] P. J. A. M. Kerkhof, "A modified Maxwell-Stefan model for transport through inert membranes: the binary friction model," *The Chemical Engineering Journal and the Biochemical Engineering Journal*, vol. 64, no. 3, pp. 319–343, 1996.

[53] S. Wang, W. M. Worek, and W. J. Minkowycz, "Performance comparison of the mass transfer models with internal reforming for solid oxide fuel cell anodes," *International Journal of Heat and Mass Transfer*, vol. 55, no. 15–16, pp. 3933–3945, 2012.

[54] J. B. Young and B. Todd, "Modelling of multi-component gas flows in capillaries and porous solids," *International Journal of Heat and Mass Transfer*, vol. 48, no. 25–26, pp. 5338–5353, 2005.

[55] D. Grondin, J. Deseure, P. Ozil, J. P. Chabriat, B. Grondin-Perez, and A. Brisse, "Solid oxide electrolysis cell 3D simulation using artificial neural network for cathodic process description," *Chemical Engineering Research and Design*, vol. 91, no. 1, pp. 134–140, 2013.

[56] M. Dumortier, O. Lacroix, and J. Sanchez-Marcano, "Modeling of mass and energy transfers in a high temperature membrane electrolyser," *International Journal of Hydrogen Energy*, no. 0, 2010.

[57] Y. Xie and X. Xue, "Modeling of solid oxide electrolysis cell for syngas generation with detailed surface chemistry," *Solid State Ionics*, vol. 224, no. 0, pp. 64–73, 2012.

[58] W. Li, Y. Shi, Y. Luo, and N. Cai, "Elementary reaction modeling of co2/h2o co-electrolysis cell considering effects of cathode thickness," *Journal of Power Sources*, vol. 243, no. 0, pp. 118–130, 2013.

[59] H. Zhang, J. Wang, S. Su, and J. Chen, "Electrochemical performance characteristics and optimum design strategies of a solid oxide electrolysis cell system for carbon dioxide reduction," *International Journal of Hydrogen Energy*, vol. 38, no. 23, pp. 9609–9618, 2013.

[60] M. Ni, "Modeling of a solid oxide electrolysis cell for carbon dioxide electrolysis," *Chemical Engineering Journal*, vol. 164, no. 1, pp. 246–254, 2010.

[61] A. Bertei and C. Nicolella, "Common inconsistencies in modeling gas transport in porous electrodes: The dusty-gas model and the Fick law," *Journal of Power Sources*, vol. 279, pp. 133–137, 2015.

[62] R. Krishna and J. A. Wesselingh, "The Maxwell-Stefan approach to mass transfer," *Chemical Engineering Science*, vol. 52, no. 6, pp. 861–911, 1997.

[63] D. L. Damm and A. G. Fedorov, "Radiation heat transfer in SOFC materials and components," *Journal of Power Sources*, vol. 143, no. 1-2, pp. 158–165, 2005.

[64] J. J. Hartvigsen, S. Elangovan, and A. Khandkar, *Modeling, Design and Performance of Solid Oxide Fuel Cells*, p. 631. Technomic Publishing company, 1993.

[65] R. C. Reid and T. K. Sherwood, *The Properties of Gases and Liquids*. McGraw-Hill, 2nd ed., 1966.

[66] C. C. Appel, N. Bonanos, A. Horsewell, and S. Linderoth, "Ageing behaviour of zirconia stabilised by yttria and manganese oxide," *Journal of Materials Science*, vol. 36, no. 18, pp. 4493–4501, 2001.

[67] A. Leonide, Y. Apel, and E. Ivers-Tiffee, "Sofc modeling and parameter identification by means of impedance spectroscopy," *ECS Transactions*, vol. 19, no. 20, pp. 81–109, 2009.

[68] J. Njodzefon, C. Graves, M. Mogensen, A. Weber, and J. Hjelm, "Kinetic studies on state of the art solid oxide cells - a comparison between hydrogen/steam and reformate fuels," *ECS Transactions*, vol. 64, pp. 51–65, 2015.

[69] A. J. Samson, P. Hjalmarsson, M. Søgaard, J. Hjelm, and N. Bonanos, "Highly durable anode supported solid oxide fuel cell with an infiltrated cathode," *Journal of Power Sources*, vol. 216, pp. 124–130, 2012.

[70] Y. S. Toulokian, R. K. Kirby, R. E. Taylor, and T. Y. R. Lee, *Thermal Expansion - Nonmetallic Solids. Thermophysical properties of Matter*, vol. 13. New York: IFI/Plenum, 1984.

[71] R. Morrell, *Handbook of Properties of Technical and Engineering Ceramics. Part 1. An Introduction for the Engineer and Designer*. London: Her Majesty's Stationery Office, 1985.

[72] M. Navasa, H. L. Frandsen, T. L. Skafte, B. Sundén, and C. Graves, "Localized carbon deposition in solid oxide electrolysis cells studied by mulitphyics modeling." Manuscript in preparation, 2016.

Paper IV

Localized Carbon Deposition in Solid Oxide Electrolysis Cells Studied by Multiphysics Modeling

Maria Navasa[1,2], Henrik Lund Frandsen[2], Theis Løye Skafte[2,3], Bengt Sundén[1] and Christopher Graves[2]

[1]Department of Energy Sciences, Lund University, Sweden
[2]Department of Energy Conversion and Storage, Technical University of Denmark, Denmark
[3]Haldor Topsoe A/S, Denmark

Abstract

Solid oxide electrochemical cells (SOCs) are devices which can convert chemical fuels directly into electrical power, and vice versa, with high efficiency. However, the commercial viability of SOCs is hindered by cell degradation which limits the operating lifetime. One degradation mechanism with severe consequences is carbon deposition, where in extreme conditions, the cell can become broken and inoperable. In electrolysis mode, carbon deposition is electrochemically driven and the conditions at which occurs can be estimated by the thermodynamic carbon deposition threshold. In this work, the local crossing of the thermodynamic carbon deposition threshold is observed both experimentally and via multiphysics simulations. A three dimensional multiphysics model was used to simulate the performance of solid oxide electrochemical cells and determine

when carbon deposition occurs in electrolysis operation mode. The main transport phenomena are included in the model and coupled to the electrochemical reactions. This enables the calculation of the local thermodynamic carbon deposition threshold and carbon activity distributions through the electrodes and across the cell as well as the temperature distribution as a function of the operating voltage. The model is validated by comparison to cell test experiments at different operating conditions with CO/CO_2 as feedstock. It is found that CO/CO_2 gas diffusion gradients and local cooling from the endothermic nature of the electrolysis reaction are the main reasons that carbon deposition occurs locally when it is not expected based on the inlet conditions. The effect of two different heat boundary conditions as well as the impact of the fuel electrode porosity, thickness and ionic conductivity on the carbon deposition phenomenon are studied.

Keywords: carbon deposition, SOEC, multiphysics modeling, Boudouard reaction, thermodynamic threshold, experimental data, fuel electrode, porosity, thickness, ionic conductivity, heat transfer.
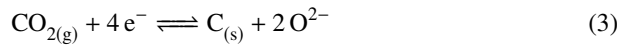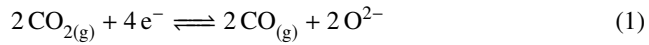
1   Introduction

Today, the energy demand is mainly met by fossil fuels and nuclear power as they can supply electricity on demand. A major drawback to the success of renewable energies is that they are nature dependent supplying electricity only when the wind blows, the sun shines, depending on the sea tides or the availability of biomass to just give a few examples. For renewable energy sources to be successful and meet a significant fraction of energy demand there is a need for large-scale economical energy storage devices to meet the supply-demand imbalance. Different energy storage alternatives are under development as current energy storage technologies are extremely expensive to scale up as a result of their dependency on limited resources or locations [1].

One of the promising devices that are under development is the solid oxide electrochemical cell (SOC). The interest in the development for this technology has increased considerably in the last ten years but most of the development has been focused on employing SOCs as fuel cells, known as solid oxide fuel cells (SOFCs), for power

2

generation. However, SOCs can be operated reversibly so that electrical energy is supplied into the cell to drive electrochemical reactions obtaining chemical energy stored as fuels. This is the electrolytic operation mode and SOCs are then known as solid oxide electrolysis cells (SOECs). In SOECs, hydrogen (H_2), carbon monoxide (CO) or syngas (H_2 and CO) can be obtained via high temperature electrolysis of steam (H_2O), carbon dioxide (CO_2) or co-electrolysis of H_2O and CO_2, respectively. An advantage of SOCs as energy storage devices is the easiness of scaling up systems by assembling individual cells into stacks to meet the desired output power. Although conventional batteries are more popular as energy storage devices, they store the electrical energy in expensive metals (Li, Pb, etc.) whereas SOECs store the electricity in the form of relatively economic fuels [1]. Withal, for SOECs to become commercially interesting, a long-term stability for a period of 5-10 years must be guaranteed which is currently not possible due to degradation mechanisms.

When performing co-electrolysis of CO_2 and H_2O at high current densities, which provides the highest syngas production rate, degradation at the interface between the nickel-yttria-stabilized zirconia (Ni-YSZ) electrode and the YSZ electrolyte has been reported due to the formation of small amounts of carbon. Duboviks *et al.* [2, 3] used Raman spectroscopy to show that carbon formation in electrolysis mode takes place at the mentioned interface, where CO is generated, whereas the more commonly known carbon formation is when supplying hydrocarbons in fuel cell mode, which occurs at the outside of the electrode first, by methane cracking, CO disproportion (Boudouard deposition) or other thermochemical reactions depending on the fuel gas composition. The formation of carbon at the active sites of the Ni-YSZ electrode may reduce the amount of active sites and, in the worst case, cause a delamination of the electrode/electrolyte interface. The Boudouard reaction, Eq. (2), describes how carbon is formed. Carbon deposition could also occur by electrolysis of carbon dioxide to solid carbon, Eq. (3), which is thermodynamically equivalent to the two-step reaction of electrolysis of CO_2 to CO, Eq. (1), followed by the Boudouard reaction. Another equivalent possibility to the two-step process described is the electrolysis of CO_2 to CO followed by the electrolysis of CO to C, Eq. (4). Although carbon deposition is thermodynamically favored only at higher reactant conversion than typically used in the operation of an SOEC, it has been observed at "safe" conversion conditions based on inlet conditions. Thus, understanding why the thermodynamic threshold is violated and where this happens locally in the cell

3

would be of great interest when choosing operating conditions and to avoid possible degradation of the cell [4].

$$2\,CO_{2(g)} + 4\,e^- \rightleftharpoons 2\,CO_{(g)} + 2\,O^{2-} \tag{1}$$

$$2\,CO_{(g)} \longrightarrow C_{(s)} + CO_{2(g)} \tag{2}$$

$$CO_{2(g)} + 4\,e^- \rightleftharpoons C_{(s)} + 2\,O^{2-} \tag{3}$$

$$CO_{(g)} + e^- \rightleftharpoons C_{(s)} + O^{2-} \tag{4}$$

Computational simulations are valuable tools for studying the performance of SOCs and optimizing their operation conditions. Despite the fact that numerical modeling can decrease the time cost and resources for cell testing, a small number of studies have been reported in comparison to experimental studies. SOFCs have attracted the major number of simulation investigations as the development of SOECs slowed down around the 1990s due to the low fossil fuel prices, but have increased in the last years due to the growing interest in green energy technologies [5]. In addition, steam electrolysis has been the main application for SOECs and consequently, it is reflected in the amount of research compared to CO_2 electrolysis or co-electrolysis of CO_2 and H_2O. Regarding modeling, very little work has been reported in literature about electrolysis of CO_2. Ni [6] developed a one dimensional (1D) electrochemical model where the overpotentials were considered and a two dimensional (2D) model where the electrochemical reactions were coupled with heat and mass transfer. Shi et al. [7] studied the current density distributions and the species concentration distributions within the anode using an elementary reaction based 1D model for a button cell. Narasimhaiah et al. [8] presented a modified Butler-Volmer equation by considering multi-step single-electron transfer reactions to model CO_2 electrolysis in a button cell. The model was evaluated when considering that the electrochemical reaction takes place at the electrode/electrolyte interface and through

the porous electrode. Other authors [9–11] have also developed 1D or 2D models for co-electrolysis, studying the effects of some geometry or operating parameters.

The aim of this study is to show where and under which operating conditions carbon deposition is locally induced by performing multiphysics simulations on a three dimensional (3D) model of an SOEC that considers the main physical phenomena that characterize these devices, i.e. electrochemical reactions, transport of charged species, momentum transfer, mass transfer and heat transfer. The model is validated with experimental data. Moreover, possible solutions to the problem will be studied by varying the thickness and porosity of the fuel electrode as well as its ionic conductivity. All three will influence the effective transport properties of the layer and carbon deposition may be avoided or minimized.

2 Experimental

A number of cell test experiments have been performed under different operating conditions to validate the multiphysics model and to study the carbon deposition phenomenon in SOECs.

Single-cell measurements have been performed on planar supported SOCs produced by Haldor Topsoe A/S. A cell sketch with the components considered in the multiphysics model is shown in Figure 1. The cell is comprised of a nickel-yttria-stabilized zirconia (Ni-YSZ) support (porous support in Figure 1), a Ni-YSZ active layer (fuel electrode in Figure 1), a YSZ electrolyte, and a lanthanum strontium cobalt ferrite (LSCF)-based oxygen electrode plus a contact layer. A gadolinia doped ceria (CGO) layer is present between the electrolyte and the LSCF-based electrode.

All cells were tested at DTU Energy (Technical University of Denmark, DTU Risø campus). A cell of 5.3 cm x 5.3 cm with an active area of 16 cm^2 is mounted into a cell test rig. The contacting of the cell is realized with corrugated Ni and Au meshes for the fuel and oxygen electrodes, respectively, which provide a uniform contacting and gas distribution. The flow configuration in the cell test rig is shown in Figure 2.
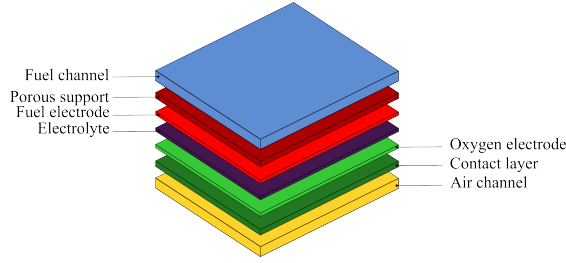
Figure 1: *Schematic drawing of the Haldor Topsoe A/S cell with its components.*
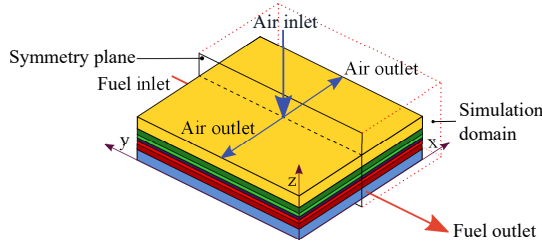

Figure 2: *Experimental setup arrangement with flow configuration and indication of the simulation domain.*

A number of current density-voltage (*i*-V) measurements were carried out with a 50 % CO/50 % CO_2 feedstock with air as oxidant gas at three different gas inlet temperatures ranging from 750 to 850 °C for validation of the model. This model has also been extensively validated for H_2/H_2O as feedstock in [12]. The inlet temperature, flows and compositions (CO partial pressure) used in the tests are specified in Table 1.

Table 1: *Inlet conditions for i-V curves comparison.*

Test	Temperature $\left[°C\right]$	Air flow rate $\left[L\,h^{-1}\right]_{STP}$	Fuel flow rate $\left[L\,h^{-1}\right]_{STP}$	p_{CO} [atm]
1	750	140	24	0.5
2	800	140	24	0.5
3	850	140	24	0.5

Furthermore, other *i*-V measurements were performed on the same type of cells for the detection of carbon formation. The inlet conditions for these measurements, where the

6

inlet temperature of the gases was set to 750 °C for all the tests, are specified in Table 2. The current of the cell when in electrolysis mode was gradually increased in steps until the voltage became unstable and started increasing due to coking in the cell. For more details about the measurements, refer to [4, 13].

Table 2: *Inlet conditions for carbon deposition validation.*

Test	CO flow rate $\left[L\,h^{-1}\right]_{STP}$	CO_2 flow rate $\left[L\,h^{-1}\right]_{STP}$	Air flow rate $\left[L\,h^{-1}\right]_{STP}$
1	10	10	140
2	12	8	140
3	2	13	140
4	5.15	12	140
5	3.2	3	140
6	9	18	140
7	2	3	140
8	2	17	140
9	9.5	5.3	140
10	5.3	9.5	140
11	5	4.8	140

3   Model description

A 3D multiphysics model of an SOC operating in electrolysis mode has been developed using the commercial software Comsol Multiphysics 5.2 using the Batteries and Fuel Cell module to study the degradation phenomenon of carbon deposition in SOECs.

The model developed for simulation of CO_2 electrolysis considers the following physical phenomena: electrochemical reactions, transport of charged species, momentum transfer, mass transfer and heat transfer. The main equations are summarized in Table 3. Besides, overall considerations such as steady state condition, gases treated as ideal gases and distributed reaction zone across the electrode are accounted for. For more details about all the physics, equations considered in the multiphysics model, parameters used

7

and other details, refer to [12].

Table 3: *Summary of the physical phenomena and the corresponding governing and supplementary equations as well as the cell components where they apply.*

Physical phenomenon	Governing equation	Suppl. equation	Component
Electrochemical reactions		Linear Chang-Jaffe kinetics	Fuel active layer + air electrode
Transport of charged species	Current conservation/Ohm's law		Electrodes + electrolyte
Momentum transfer	Momentum conservation		Everywhere except electrolyte
Mass transfer	Continuity and species balance	SMM + Bosanquet eq.	Everywhere except electrolyte
Heat transfer	Energy conservation	Joule heating + electrochemistry sources	Everywhere

The electrochemical reactions considered in the model are CO_2 reduction to CO at the fuel side, Eq. (1), and the oxidation of the oxide ion (O^{2-}) to O_2, Eq. (5), at the air side.

$$O^{2-} \rightleftharpoons \tfrac{1}{2} O_{2(g)} + 2\,e^-$$ (5)

Linear Chang-Jaffe kinetics [14] are used in this work to calculate the current density at the electrodes as specified in Table 3. At the fuel side, Eq. (6) is used while at the air side, Eq. (7) is valid [15, 16].

$$i_{\text{fuel}} = \frac{\eta}{R_{0,\text{red}} \exp\left(\frac{E_{a,\text{red}}}{RT}\right) a_{\text{CO}}^{0.058}\, a_{\text{CO}_2}^{-0.25}}$$ (6)

$$i_{\text{air}} = \frac{\eta}{R_{0,\text{ox}} \exp\left(\frac{E_{a,\text{ox}}}{RT}\right) a_{\text{O}_2}^{-0.25}}$$ (7)

8

where η is the overpotential, R is the ideal gas constant, T is the temperature, a_i is the activity of the component i in the correspondent gas mixture, E_a is the activation energy of the activation polarization resistance and R_0 is the pre-exponential factor of this resistance.

The Stefan-Maxwell model (SMM) is used to model gas diffusion as stated in Table 3 and in detail in [12]. To account for both molecular and Knudsen diffusion in the SMM, the Bosanquet formula, Eq. (8), has been used in the work despite its limitations as discussed by Bertei and Nicolella [17].

$$\frac{1}{D_{ij}^{\text{eff}}} = \frac{1}{D_{ij}^{B,\text{eff}}} + \frac{1}{D_i^{K,\text{eff}}} \tag{8}$$

where D_{ij}^{eff} is the effective diffusion coefficient, $D_{ij}^{B,\text{eff}}$ is the effective binary diffusion coefficient and $D_i^{K,\text{eff}}$ is the effective Knudsen diffusion coefficient.

The calculation of the effective properties as well as the diffusion coefficients implemented are defined in [12].

Boundary conditions

The main boundary conditions considered in the multiphysics model are shown in Figure 3. Unless specified, all other boundaries are electrically insulated. Moreover, a heat flux boundary condition is specified to these boundaries to take into the account the effect from the furnace at 750 °C where the cell is mounted surrounded by alumina (Al_2O_3) blocks, Eq. (9).

$$q_{\text{furnace}} = \frac{k_{Al_2O_3}}{t_{Al_2O_3}} (T_{\text{furnace}} - T) \tag{9}$$

where q_{furnace} is the heat from the furnace to the cell in $\left[\text{W m}^{-2}\right]$, $k_{Al_2O_3}$ the thermal
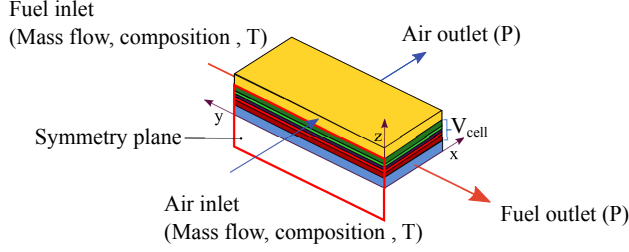
Figure 3: *Main boundary conditions.*

conductivity of alumina, t the thickness of the alumina blocks surrounding the cell, T_{furnace} is the furnace temperature and T, the cell temperature (at the boundary of the simulation domain).

The conductivity of alumina can be expressed as function of temperature, Eq. (10) [18, 19].

$$k_{\text{Al}_2\text{O}_3} = 5.5 + 34.5 \exp\left(-0.0033\left(T - 273\right)\right) \tag{10}$$

where $k_{\text{Al}_2\text{O}_3}$ is in $\left[\text{W}\,\text{m}^{-1}\,\text{K}^{-1}\right]$ and T is in [K]. Eq. (10) is valid for temperatures between 25 and 1300 °C.

Apart from having a strong tool available for simulation of CO_2 electrolysis, the model is used for detection of areas which are prone to carbon deposition due to local crossing of the thermodynamic threshold. This is a very important feature as carbon deposition is a degradation issue that in larger amounts can destroy the cell.

3.1 Carbon deposition

One way to evaluate if carbon deposition will occur is by calculating the thermodynamic carbon deposition threshold, $p_{\text{CO},B}$. If the partial pressure of CO (p_{CO}) in the cell exceeds the carbon deposition threshold, carbon will form and this will occur first at

the electrolyte/fuel electrode interface. This thermodynamic threshold, Eq. (13), can be calculated from the Boudouard reaction equilibrium constant, Eq. (11), and Dalton's law of partial pressures, Eq. (12), when $p_{total} = 1$ atm:

$$K_{eq,B} = \frac{p_{CO_2}}{p_{CO}^2} \tag{11}$$

$$p_{total} = p_{CO_2} + p_{CO} \tag{12}$$

$$p_{CO,B} = \frac{1}{2K_{eq,B}} \left(-1 + \sqrt{1 + 4K_{eq,B}}\right) \tag{13}$$

where $K_{eq,B}$ is the equilibrium constant for the Boudouard reaction and p_i is the partial pressure of species i in the fuel gas mixture. The Boudouard equilibrium constant is implemented as a temperature dependent function with data obtained from the FactSage 5.5 database, Eq. (14). The thermodynamic threshold calculated via the Boudouard reaction, $p_{CO,B}$, is equivalent to the thermodynamic threshold obtained via the direct electrolysis of CO_2 to C, Eq. (3), so the model cannot differentiate between the different carbon formation paths.

$$K_{eq,B} = \exp\left(-1 \cdot 10^{-8}T^3 + 5 \cdot 10^{-5}T^2 - 0.0907T + 50.216\right) \tag{14}$$

where T is the temperature in [K] and $K_{eq,B}$ in $\left[\text{atm}^{-1}\right]$. Equation (14) is only valid for temperatures between 500 and 1400 °C.

Another way of evaluating carbon formation is by calculating the carbon activity, α_C, in the cell, Eq. (15). The carbon activity takes into account the temperature-dependent thermodynamic threshold as well as the species concentrations. For α_C values larger than 1, there is a thermodynamic driving force for carbon deposition to occur, while for values below 1, no carbon deposition will be observed. This method gives the same

results as the p_{CO} threshold method described above; it just condenses the propensity for carbon deposition into a single parameter.

$$\alpha_C = K_{eq,B} \frac{p_{CO}^2}{p_{CO_2}} \tag{15}$$

The complexity of the multiphysics model developed allows the calculation of the local thermodynamic carbon deposition threshold throughout the cell allowing the identification and location of areas prone to carbon deposition. To do so, the cell voltage was gradually increased in steps until the local partial pressure of CO exceeded the local carbon deposition threshold, mimicking the experimental procedure used for detection of carbon deposition [4, 13].

4 Validation

In this section, two different validation studies are presented by using the model defined above to model the experimental setup described and the carbon formation phenomenon.

First, a current density-voltage (*i*-V) curves comparison between the simulated data and the experimental data at three different temperatures is shown. Then, a comparison of the carbon formation conditions at different fuel flow rates and fuel compositions between the experimental and simulated data is presented.

Furthermore, a detailed description of the partial pressure of CO and temperature for one specific set of inlet conditions, defined as base case, is shown, as reference for the following parameter study.

To model the setup in Section 2 the following considerations have been made:

- Due to the flows configuration, see Figure 2, a symmetry plane can be drawn for the air inlet, reducing the simulation domain to a half of the real cell. The flow

geometry can thus be considered to be cross-flow over a 20 mm x 40 mm area, see Figure 3.

- The current is collected by corrugated meshes on either side, as described in Section 2, and a reasonable assumption is therefore that the current collection occurs evenly across both electrode surfaces.

- To account for the CGO barrier layer, which has not been modeled, the electrolyte thickness modeled is the sum of both the electrolyte and the CGO barrier thicknesses. Furthermore, the conductivity is adjusted to match the ohmic resistance obtained from impedance measurements.

4.1   Validation against *i*-V curves

As this model was extensively validated for H_2/H_2O as feedstock, where a wide range of tests were performed to validate the model under different temperatures, fuel flows and compositions with success [12], only temperature variation was considered for comparing *i*-V curves in this work. To fit the computational model to the experimental data, only one fitting parameter is required but must be tested under different operation conditions to ensure its reliability. This single fitting parameter is the pre-exponential factor of the activation polarization resistance, R_0, for the fuel electrode contributing to the current density, defined via the linear Chang-Jaffe kinetics [14].

The inlet conditions are those specified in Table 1 while all the parameters required for the simulations are defined in Table 4 and in [12].

Figure 4 presents the different *i*-V curves, from experiments and simulations, for a 24 $L\,h^{-1}$ at standard conditions (STP) CO/CO_2 feedstock when operating under electrolysis and fuel cell mode at three different temperatures ranging from 750 to 850 °C at 50 % CO. Inlet flow rates and compositions are kept constant for all temperatures as specified in Table 1. Results show a maximum deviation of 1.2 % between the experimental and simulated cell voltage for all temperatures considered.

Table 4: *Cell parameters used in the multiphysics model.*

| Parameter	Value	Units
Operating pressure (p)	1	atm
YSZ ionic conductivity (σ_{YSZ})	$\frac{100}{10^{4.9\frac{1000}{T}-3.3}}$[20]	S m^{-1}
Ni volume fraction (χ_{Ni})	0.26	–
YSZ volume fraction (χ_{YSZ})	$1 - \varepsilon - \chi_{\text{Ni}}$	–
Fuel electrode porosity (ε)	0.3	–
Oxygen electrode porosity (ε)	0.20	–
CO diffusion volume (υ_{CO})	$1.8 \cdot 10^{-5}$[21]	$\text{m}^3\,\text{mol}^{-1}$
CO_2 diffusion volume $\left(\upsilon_{\text{CO}_2}\right)$	$2.67 \cdot 10^{-5}$ [21]	$\text{m}^3\,\text{mol}^{-1}$
Fuel electrode mean pore diameter $(d_{p,\text{fuel}})$	641[22]	μm
Air electrode mean pore diameter $(d_{p,\text{air}})$	306 [22]	μm
CO_2 reduction reaction activation energy $(E_{a,red})$	118.64 [15]	kJ mol^{-1}
Oxidation reaction activation energy $(E_{a,ox})$	123 [23]	kJ mol^{-1}
Polarization resistance factor reduction reaction $(R_{0,red})$	$2 \cdot 10^{-12}$	$\Omega\,\text{cm}^2$
Polarization resistance factor oxidation reaction $(R_{0,ox})$	$5 \cdot 10^{-13}$	$\Omega\,\text{cm}^2$
Alumina block thickness $\left(t_{\text{Al}_2\text{O}_3}\right)$	4	cm
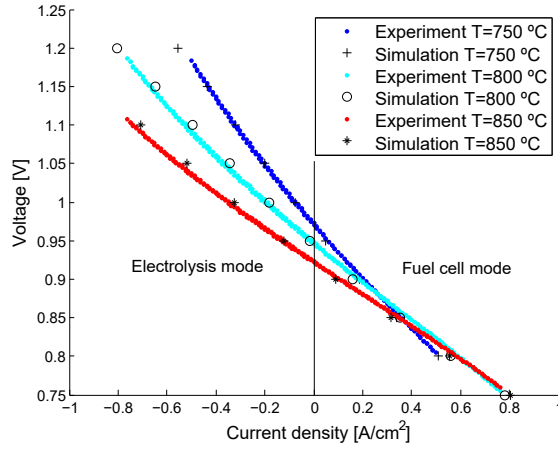
Figure 4: *i-V curves comparison for 24* $\mathrm{L\,h^{-1}}$ STP *CO/ CO$_2$ at 50 % CO under electrolysis and fuel cell mode at different gas inlet temperatures. Negative and positive current densities correspond to electrolysis mode and fuel cell mode operation, respectively.*

4.2   Validation against carbon deposition

The extensive validation realized with H_2/H_2O [12] and the *i*-V comparison for CO/CO_2 (Figure 4) show that the multiphysics model developed agrees well in terms of cell performance with the experimental data for the two feedstocks. Nonetheless, the model should also be able to predict degradation phenomena such as carbon formation.

To validate against carbon deposition, the current density and the CO partial pressure achieved at the cell outlet where carbon formation is first detected both experimentally and via simulations in the cell under the different flow rates and compositions listed in Table 2 are compared in Figure 5 at 750 °C. Simulation results provide an acceptable agreement with the experimental values obtained presenting similar trends. Deviations between experimental and simulated data can be due to among other factors, the magnitude of the step used for increasing the cell voltage (simulations) or current density (experiments). Moreover, results clearly indicate a violation of the thermodynamic threshold at the specified gas inlet temperature as almost all the cases considered showed

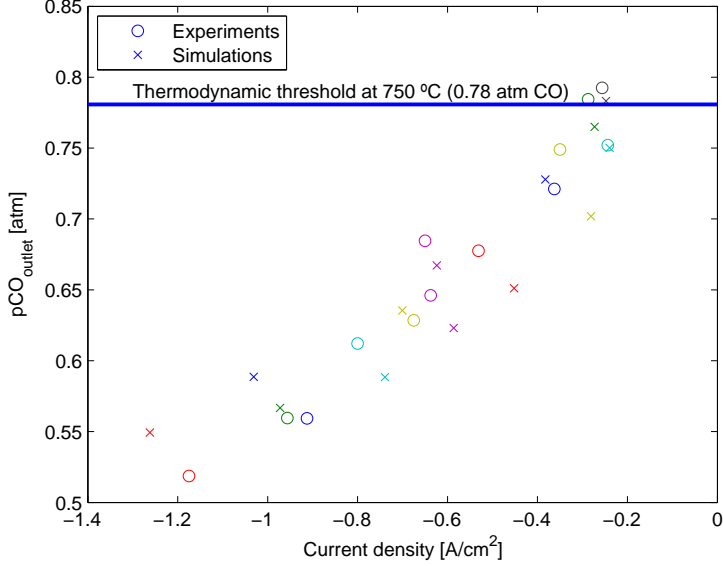carbon formation at lower p_{CO} values than the indicated threshold.

Figure 5: *Current density and p_{CO} at the cell outlet comparison when carbon formation is first detected in the cell for different inlet fuel flow rates and compositions at 750 °C.*

4.3 Base case

A base case is defined in order to study the effect of the fuel electrode's support layer thickness, fuel electrode porosity and ionic conductivity on the carbon deposition phenomenon. The inlet conditions for the base case are 750 °C , 2 L h^{-1} of CO and 13 L h^{-1} of CO$_2$ at standard conditions. The operating cell voltage is 1.31 V and corresponds to the operating cell voltage where carbon formation is first detected under the specified inlet conditions. The effect of two different heat boundary conditions is studied. The first condition is the heat flux specified previously reflecting the experimental setup, Eq. (9), while the other corresponds to thermal insulation (adiabatic, $q_{furnace}$ = 0). To further be

able to analyze the effect of such structural parameters, it is necessary to understand the partial pressure distribution of CO throughout the cell as well as the temperature distribution, as they are two factors that can impact on carbon formation, see Figures 7 and 8. Figures 7a, 7c, 8a and 8c show the CO partial pressure and temperature distribution, respectively, when considering the heat flux boundary condition while Figures 7b, 7d, 8b and 8d show the distribution of such parameters for the thermally insulated case. The distributions in Figures 7a, 7b, 8a and 8b correspond to the fuel active/fuel support layer interface while Figures 7c, 7d, 8c and 8d correspond to three different planes across the fuel channel. For more details about such planes locations, see Figure 6.


(a) *Active layer-diffusion interface plane*   (b) *Vertical planes in the fuel flow direction*
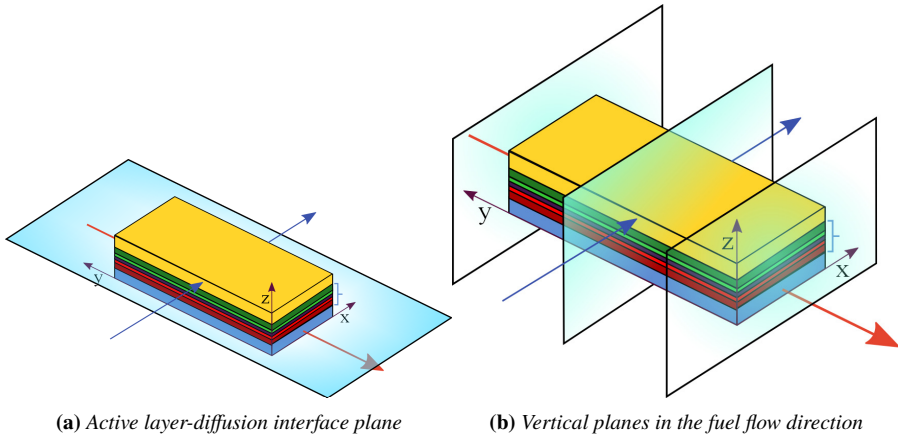
**Figure 6:** *Horizontal and vertical planes for data analysis*

It should be pointed out that the representation of the y-axis in Figures 7c and 7d is the whole cell thickness while in Figures 8c, 8d, 9c and 9d it is only from the fuel electrode/electrolyte interface (now y=0) and upwards.

The temperature distributions along the fuel flow, Figures 7c and 7d, and at the fuel active/diffusion layer interface, Figures 7a and 7b, indicate a temperature decrease along the fuel flow, $y = 40$ mm to $y = 0$ mm, and the air flow, $x = 0$ mm to $x = 20$ mm, for both heat boundary conditions. The temperature decrease along the fuel flow is due to that the operating cell voltage, 1.31 V, is below the thermoneutral voltage for CO_2 electrolysis (1.46 V) at 750 °C, and the corresponding endothermic electrochemical re-
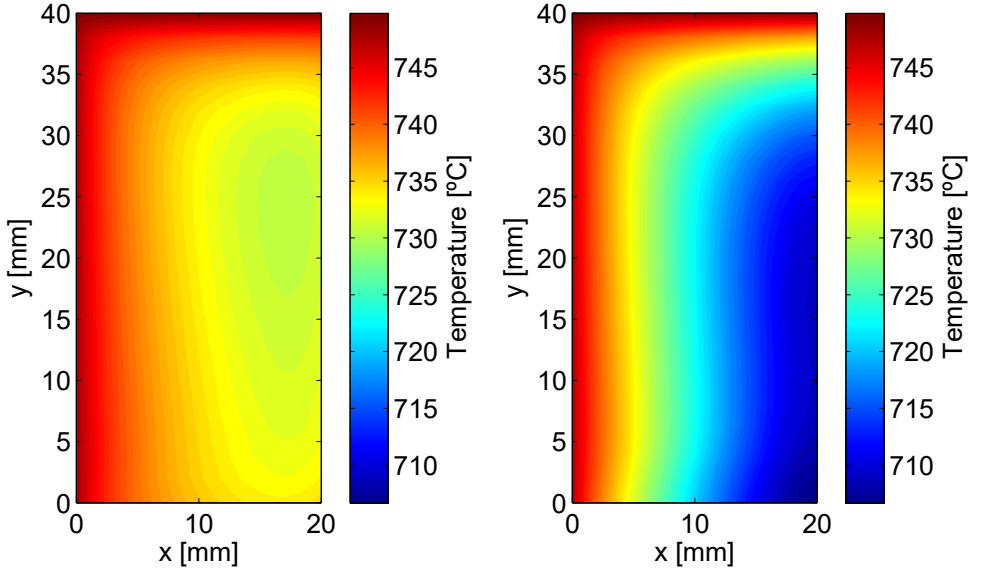
(a) *T with heat flux bounday condition*

(b) *T with thermal insulation*
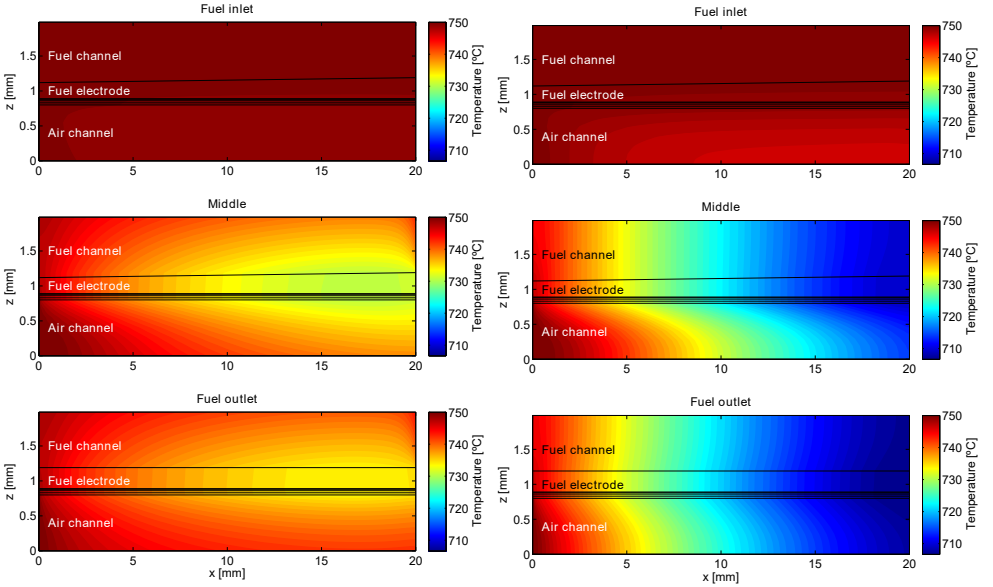
(c) *T with heat flux bounday condition*

(d) *T with thermal insulation*

18

Figure 7: *Temperature distribution: (a) and (b) at the fuel active/support layer interface, (c) and (d) at three different positions along the fuel flow for the base case. Heat flux boundary condition accounts for the furnace where the cell is placed in the experimental setup whereas for thermal insulation, adiabatic conditions apply.*

actions dominate over Joule heating leading to an endothermic cell behavior. The coldest region in the cell corresponds to the fuel and air outlets for the thermally insulated case. For the non-zero heat case, the coldest region is shifted a bit upstream due to the heat from the surrounding furnace. Temperature will also affect the formation of carbon as the equilibrium constant for the Boudouard reaction is temperature dependent, Eq. (14), and consequently, the thermodynamic carbon deposition threshold that indicates carbon deposition, Eq. (13). A temperature decrease lowers the thermodynamic carbon deposition threshold, $p_{CO,B}$, and as the temperature varies through the cell, so does the local threshold. The lowest temperature attained in the cell, and thus, the lowest local thermodynamic threshold is reached when thermal insulation is considered, Figures 7b and 7d, due to the heat consumption from the electrochemical reactions. However, when supplying external heat, i.e., when the heat flux boundary is accounted for, Figures 7a and 7c, the temperature gradient across the cell is decreased, shifting the local thermodynamic threshold. A temperature difference of 43.4 °C is registered for the thermal insulation boundary while this gradient is reduced to 20 °C for the heat flux boundary condition. Thus, by supplying heat to the system, the local thermodynamic threshold can be shifted towards the theoretical value at 750 °C, as the temperature gradient across the cell is decreased approaching isothermal conditions. At the same time, a higher overall temperature results in higher current density at the same cell voltage, yielding a higher overall CO_2 conversion to CO. This increase in generated p_{CO} may partly counter the decreased propensity of carbon deposition resulting from the increased in the carbon deposition thermodynamic threshold.

Figures 8b and 8d show not only how the partial pressure of CO increases along the fuel flow direction, from $y = 40$ mm to $y = 0$ mm, reaching its highest value at the fuel outlet, close to the air inlet ($x = 0$ mm) for the thermal insulation condition, but that the CO partial pressure is highest at the electrolyte/fuel active layer interface. Similar trend is observed when the heat flux condition is accounted for, only that a more even distribution of the species throughout the cell is achieved, see Figures 8a and 8c. That the pCO value is highest at this interface corroborates that carbon formation in SOEC is electrochemically driven as Duboviks et al. [2, 3] pointed out, as it is where the electrochemical conversion of CO_2 to CO (or C) occurs. Higher partial pressure of CO will favor carbon formation as specified by the Boudouard reaction, Eq. (2) or the CO product might be bypassed entirely if direct electrochemical carbon deposition is
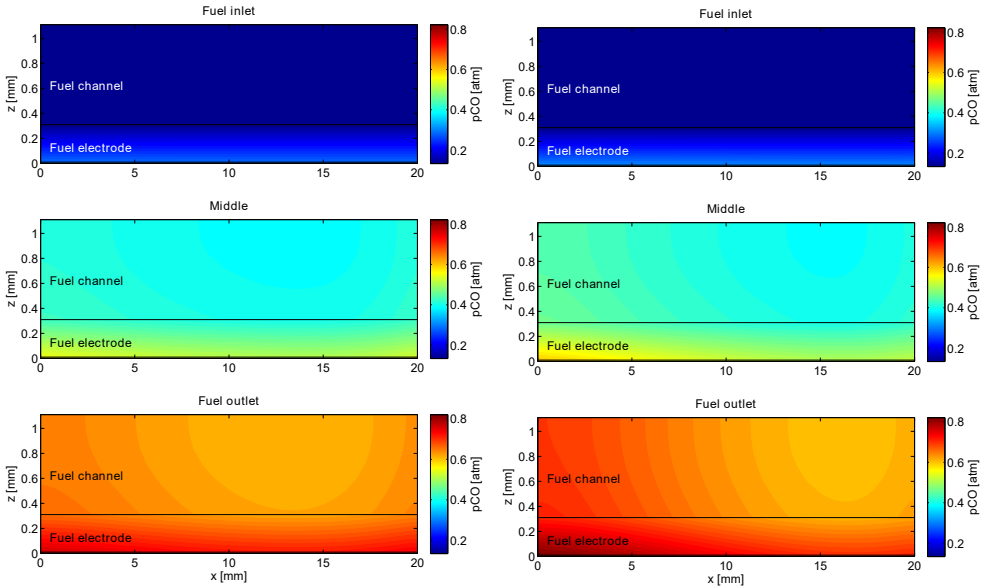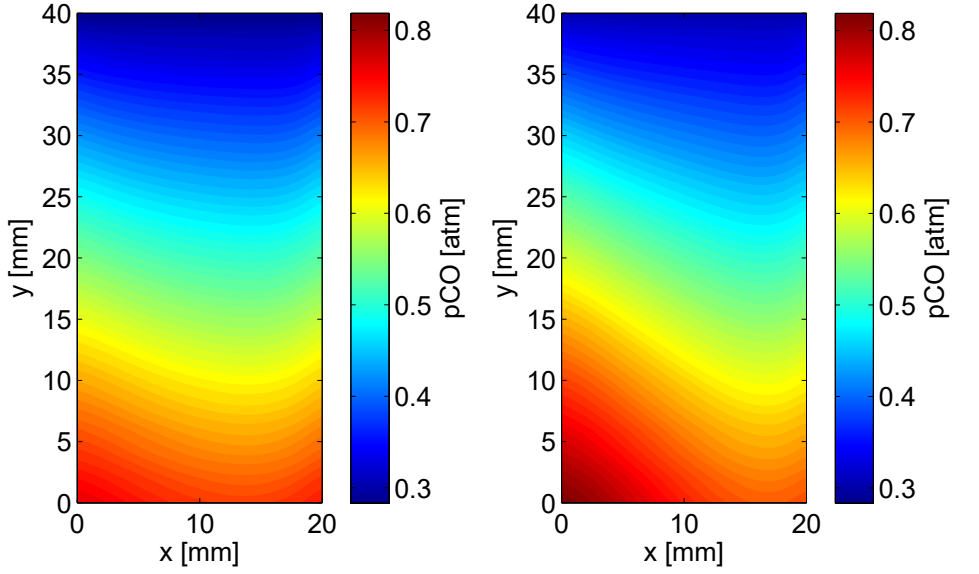
(a) p_{CO} *with heat flux boundary condition*

(b) p_{CO} *with thermal insulation*

(c) p_{CO} *with heat flux boundary condition*

(d) p_{CO} *with thermal insulation*

Figure 8: *Partial pressure distribution of CO: (a) and (b) at the fuel active/support layer interface, (c) and (d) at three different positions along the fuel flow for the base case.*

occurring, Eq. (3).

A parameter that takes into account both the effects of temperature and concentration of CO and that gives a quantification of the probability that carbon will be formed is the carbon activity, Eq. (15). The carbon activity for the base case is shown in Figure 9 for the two heat boundary conditions and at the different interfaces/planes previously defined. For the same operating cell voltage, a higher carbon activity is registered for the thermally insulated case. A significantly larger temperature gradient across the cell for the non-heat flux case, double of that for the heat flux case, can be explain the higher carbon activity as the thermodynamic carbon deposition threshold is decreased substantially, and therefore, larger amounts of carbon are formed when thermal insulation is considered as the p_{CO} values registered for both cases do not differ as much as temperatures do.

Moreover, it can be clearly observed that the region most prone to carbon formation is the at the fuel and air outlets, at the fuel electrode active layer close to the electrolyte interface, Figures 9c and 9d.

5   Results and discussion

Carbon deposition can be caused due to a high enough local concentration of carbon monoxide. This may be due to gas diffusion limitations away from the reaction sites at the electrode/electrolyte interface, where the reactant (CO_2) has to diffuse a longer distance, increasing the concentration of CO at the interface. Since CO is produced at the Ni-YSZ 3PBs, those should be the locations with the highest concentration of CO and thus prone to carbon deposition. In fact, carbon might be formed right there without any release of CO, Eq. (3). Another factor that may incite carbon formation is temperature. Due to the temperature dependency of the thermodynamic threshold, when operating under the thermo-neutral voltage, a temperature decrease through the cell is expected, lowering the local threshold. So since temperature decreases along the flow direction during endothermic electrolysis, at certain locations the concentration of CO might not be high enough to deposit carbon but as the flow continues down the channel, the temperature lowers and then carbon deposits. Therefore, there are multiple scenarios
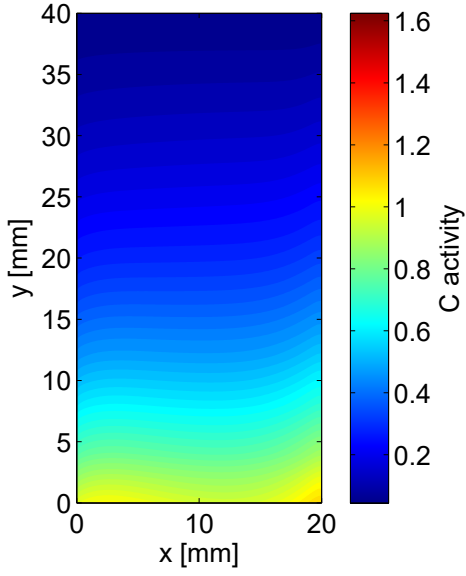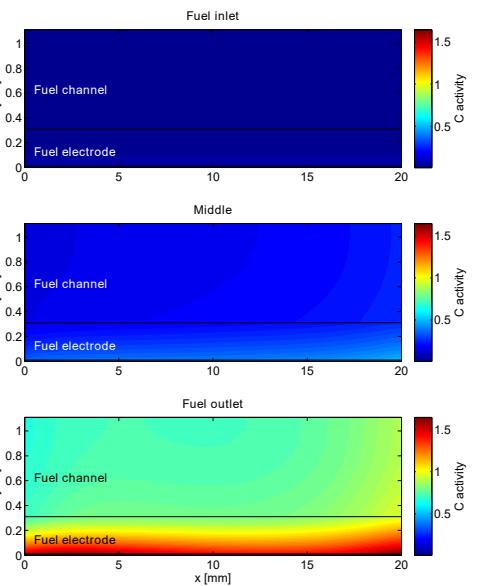
(a) α_C *with heat flux boundary condition*
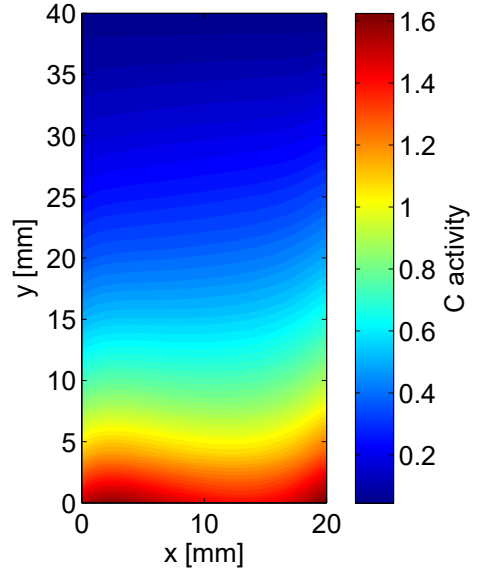
(b) α_C *with thermal insulation*

(c) α_C *with heat flux boundary condition*

(d) α_C *with thermal insulation*

22
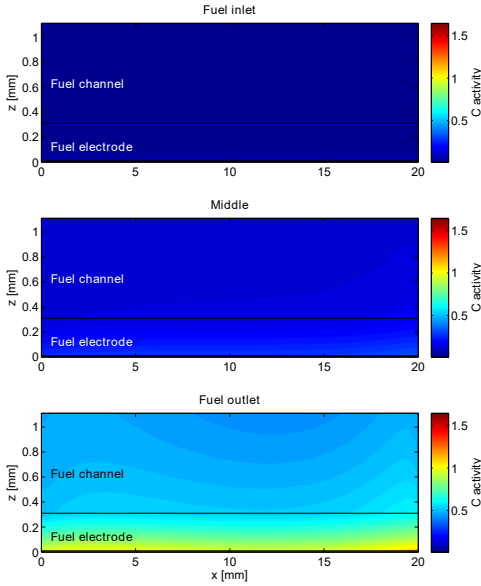
Figure 9: *Carbon activity distribution: (a) and (b) at the fuel active/support layer interface, (c) and (d) at three different positions along the fuel flow for the base case.*

which can cause carbon deposition.

To study the effect of such factors on carbon formation, a parameter study is performed. The structural parameters considered for the study are the porosity, the thickness and the ionic conductivity of the the fuel electrode. All the results presented in this section are performed with the heat flux boundary condition.
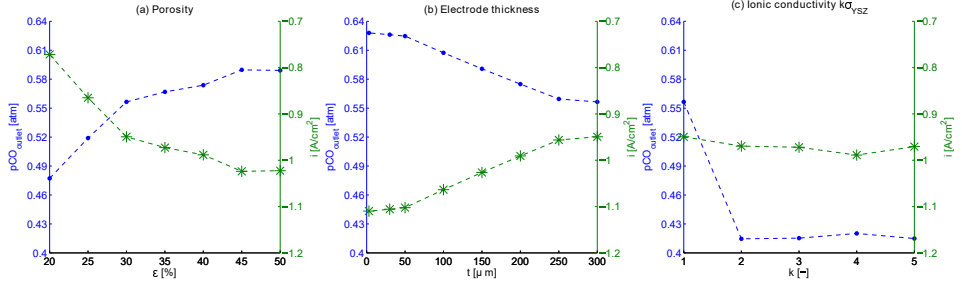

Figure 10: *Maximum p_{CO} values obtained before carbon deposition is detected in the cell for different fuel electrode porosity values, thicknesses and ionic conductivities and their corresponding current densities.*

Figure 10 presents the highest carbon monoxide partial pressure one can obtain before carbon deposition is first detected in the cell in the primary y-axis as well as the corresponding current density in the secondary y-axis when varying the fuel electrode porosity, thickness and ionic conductivity.

At low porosity values, larger gas diffusion limitations exist which hinder the transport of both CO_2 and CO, resulting in higher p_{CO} values at the reaction site favoring carbon formation. Due to this, carbon is detected at lower current densities than for higher porosity values. With increasing porosity, diffusion limitations are decreased reducing the probabilities for carbon formation although after 30 % porosity, the maximum p_{CO} tends to a plateau.

The fuel electrode thickness has been modified by changing the thickness of the diffusion layer. The thickness of the active layer has remained fixed. The thickness values shown in Figure 10 correspond to the thickness of the diffusion layer. By decreasing the electrode thickness, diffusion limitations are decreased as the diffusion path is shortened,

facilitating the transport of species so the amount of carbon monoxide at the reaction sites is decreased and larger p_{CO} values can be obtained before carbon formation is detected. In other words, higher current densities are required to detect carbon formation in thinner electrodes.

The last parameter analyzed is the ionic conductivity of the fuel electrode. As the ionic conductivity, conductivity of YSZ, is implemented as a temperature dependent function as specified in Table 4, a factor is taken into account for variation of this parameter. By increasing the ionic conductivity, higher current densities are achieved favoring the electrochemical reactions and in theory, that should result in an improvement of the cell performance. However, a constant current density is observed in Figure 10c. As the inlet flow rates are kept constant, when increasing the ionic conductivity, higher current densities are achieved and so the p_{CO} values, indicating coking for that cell voltage.

Moreover, the distribution of the local partial pressure of CO, the local thermodynamic threshold ($p_{CO,B}$) and the temperature at the fuel outlet/air outlet, see Figure 11, through the cell thickness are shown for different fuel electrode porosities, thicknesses and ionic conductivities to better understand the effects of these parameter variations. The fuel/air outlets corner is chosen as it is the region in the cell with highest carbon activity as shown in Figure 9. Results are presented for one chosen operating cell voltage, which corresponds to the voltage for the base case, which is the first voltage where carbon deposition is first detected.
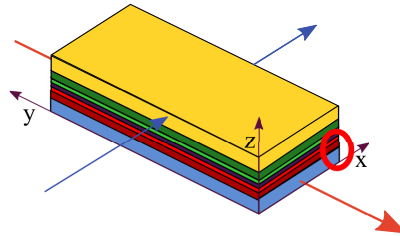

Figure 11: *Indication of the fuel electrode region where the focus is set for the parametric study corresponding to the fuel and air outlets.*

5.1 Effect of porosity

Three different porosity values have been chosen to study the local partial pressure of CO, the thermodynamic threshold and temperature profiles at the most carbon active region of the cell when operating in electrolysis mode below the thermo-neutral voltage. These profiles are shown in Figure 12 where the chosen porosity values are 20 %, 30 % and 50 %.
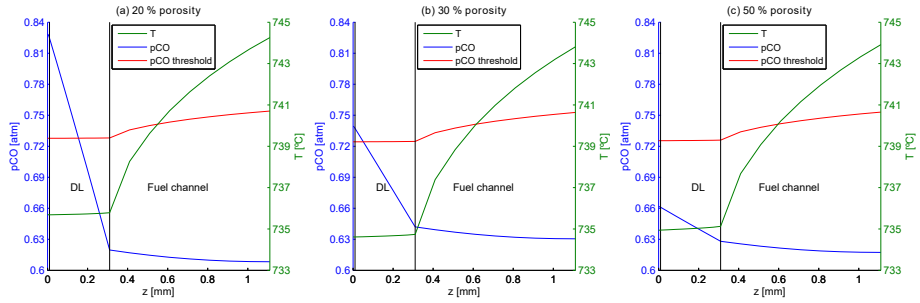

Figure 12: *Local p_{CO}, p_{CO} threshold and temperature at the fuel outlet/ air outlet at 1.31 V for three different fuel electrode porosity values: 20 %, 30 % and 50 %.*

Figure 12 indicates that gas diffusion affects carbon formation. A porosity increase decreases gas diffusion limitations considerably as the p_{CO} gradient is reduced and the maximum value at the electrolyte/electrode interface is lowered. A slight decrease in temperature turns into a slight decrease in the thermodynamic threshold although being almost insignificant. This trend has been confirmed experimentally [13].

5.2 Effect of electrode thickness

The distribution of the aforementioned variables are shown for three different fuel electrode thicknesses in Figure 13. As the active layer is fixed to 10 µm as specfied in [12], the thickness of the diffusion layer, indicated with DL in the figure, has been set to 300, 30 and 3 µm giving the total fuel electrode thickness values specified in Figure 13.
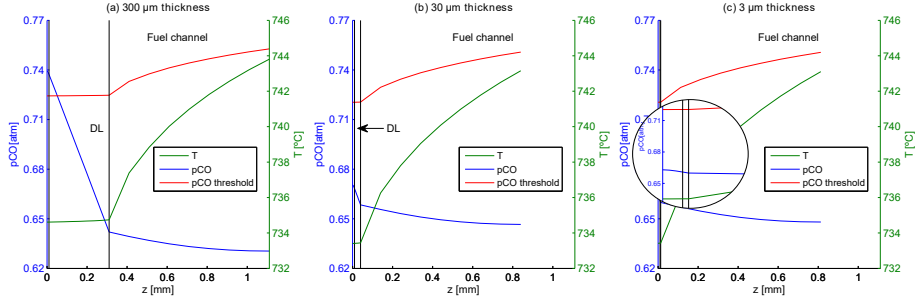
Figure 13: *Local p_{CO}, p_{CO} threshold and temperature at the fuel outlet/ air outlet at 1.31 V for three different fuel electrode thicknesses: 310 μm, 40 μm and 13 μm.*

The local distribution of the variables show that gas diffusion limitations (gradient of the p_{CO}) decrease when decreasing the fuel electrode thickness. Moreover, lower temperatures are reached at lower thicknesses, which turn into a lower thermodynamic threshold. As the effect from gas diffusion is higher than the temperature effect, by decreasing the thickness, carbon deposition can be avoided.

5.3 Effect of ionic conductivity

As above, the distribution of the local p_{CO}, p_{CO} threshold and temperature are shown in Figure 14 for three different fuel electrode ionic conductivity values. The values chosen are σ_{YSZ}, $3\sigma_{YSZ}$ and $5\sigma_{YSZ}$, where σ_{YSZ}.

Almost no significant difference is observed regarding temperature distribution and the p_{CO} gradient through the fuel electrode and channel. Distinction resides in the absolute values of the p_{CO}. At higher ionic conductivity values, higher p_{CO} values are registered at the electrolyte/electrode interface due to the electrochemical reaction being favored by higher current densities at the same cell voltage and flow inlet conditions. Higher concentration of CO favors carbon formation due to the Boudouard reaction. In this case, neither gas diffusion limitations nor temperature have an impact on the carbon
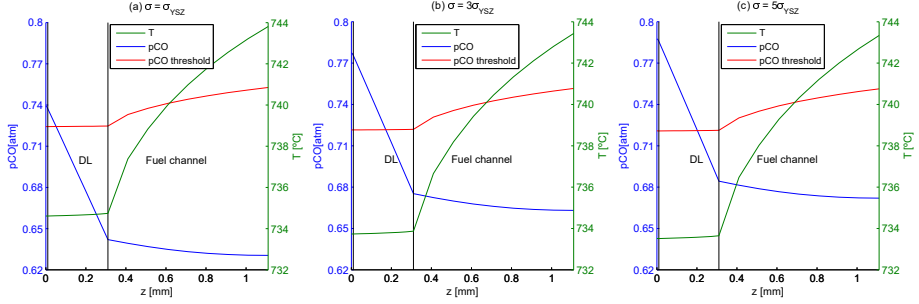
Figure 14: *Local p_{CO}, p_{CO} threshold and temperature at the fuel outlet/ air outlet at 1.31 V for three different fuel electrode ionic conductivities: σ_{YSZ}, $3\sigma_{YSZ}$ and $5\sigma_{YSZ}$*

.

formation.

6 Conclusions

In this work the mathematical equations needed for modeling carbon deposition in a three dimensional solid oxide electrochemical cell model including heat, mass, species and momentum transfer and transport of charged species together with a detailed model of the electrochemical reactions have been briefly documented.

The model has been validated against cell test experiments with cross-flow geometry for CO/CO_2 feedstocks when operating in electrolysis mode. The experiment comprised variations in temperature and was validated by comparison of *i*-V curves. The model presented very good agreement with the experimental data with a unifying set of model parameters, showing a correct interaction between physical phenomena in-spite of the complexity of the model.

A detailed analysis of this degradation phenomenon has been performed showing a good agreement between the experimental data and the modeling approach of the local

crossing of the thermodynamic carbon deposition threshold.

The effects of considering the heat from the surrounding furnace where the cell is mounted and from a thermally insulated boundary condition on the carbon activity were evaluated showing that thermal insulation favors carbon deposition due to lowering the thermodynamic carbon deposition threshold.

The influence of temperature and gas diffusion limitations on the local thermodynamic carbon deposition threshold was demonstrated by variation of the fuel electrode porosity, thickness and ionic conductivity. Finding an optimal configuration so that carbon deposition is minimized or avoided is not straightforward due to the high degree of complexity and coupling between all the physics involved in solid oxide electrolysis cells.

7   Acknowledgments

List of symbols

a_i	Chemical activity of species i, dimensionless
D	Mass diffusion coefficient, $[\mathrm{m^2\,s^{-1}}]$
d_p	Mean pore diameter, $[\mathrm{m}]$
E_a	Activation energy, $[\mathrm{kJ\,mol^{-1}}]$
i	Current density, $[\mathrm{A\,m^{-2}}]$
$K_{eq,B}$	Boudouard reaction equilibrium constant, $[\mathrm{atm^{-1}}]$
k	Thermal conductivity, $[\mathrm{W\,m^{-1}\,K^{-1}}]$

p	Pressure, [Pa] or [atm]
p_i	Partial pressure of species i, [atm]
q	Heat source, $[\mathrm{W\,m^{-2}}]$
R	Ideal gas constant, $[\mathrm{J\,mol^{-1}\,K^{-1}}]$
R_0	Pre-exponential factor of the activation polarization resistance, $[\Omega\,\mathrm{cm}^2]$
T	Temperature, [K]
t	Thickness, [cm]
V	Voltage, [V]
v	Diffusion volume, $[\mathrm{m^3\,mol^{-1}}]$

Greek letters

α_C	Carbon activity, dimensionless
ε	Porosity of the electrodes, dimensionless
η	Overpotential, [V]
σ	Electric conductivity, $[\mathrm{S\,m^{-1}}]$
χ_i	Volume fraction of phase i in the electrode, dimensionless

Chemical species & compounds

Al_2O_3	Alumina or Aluminium Oxide (III)
Au	Gold
C	Carbon
CO	Carbon monoxide
CO_2	Carbon dioxide
e^-	Electron
H_2	Hydrogen
H_2O	Water
Li	Lithium

Ni	Nickel
O_2	Oxygen
O^{2-}	Oxide ion
Pb	Lead

Abbreviations

1D/2D/3D	One, two or three dimensional
3PB	Triple-phase boundary
CGO	Gadolinia doped ceria
DTU	Technical University of Denmark
LSCF	Lanthanum strontium cobalt ferrite
SMM	Stefan-Maxwell model
SOC	Solid oxide electrochemical cell
SOEC	Solid oxide electrolysis cell
SOFC	Solid oxide fuel cell
STP	Standard temperature and pressure
YSZ	Yttria-stabilized zirconia

References

[1] C. Graves, S. D. Ebbesen, S. H. Jensen, S. B. Simonsen, and M. B. Mogensen, "Eliminating degradation in solid oxide electrochemical cells by reversible operation," *Nature Materials*, vol. 14, no. 2, pp. 239–244, 2015.

[2] V. Duboviks, R. Maher, M. Kishimoto, L. Cohen, N. Brandon, and G. Offer, "A raman spectroscopic study of the carbon deposition mechanism on Ni/CGO electrodes during CO/CO_2 electrolysis," *Physical Chemistry Chemical Physics*, vol. 16, no. 26, pp. 13063–13068, 2014.

[3] V. Duboviks, M. Lomberg, R. C. Maher, L. F. Cohen, N. P. Brandon, and G. J. Offer, "Carbon deposition behaviour in metal-infiltrated gadolinia doped ceria electrodes

for simulated biogas upgrading in solid oxide electrolysis cells," *Journal of Power Sources*, vol. 293, pp. 912–921, 2015.

[4] T. Skafte, C. Graves, P. Blennow, and J. Hjelm, "Carbon Deposition during CO_2 Electrolysis in Ni-based Solid Oxide Cell Electrodes," *ECS Transactions*, vol. 68, no. 1, pp. 3429–3437, 2015.

[5] S. D. Ebbesen and M. Mogensen, "Electrolysis of carbon dioxide in solid oxide electrolysis cells," *Journal of Power Sources*, vol. 193, no. 1, pp. 349–358, 2009.

[6] M. Ni, "Modeling of a solid oxide electrolysis cell for carbon dioxide electrolysis," *Chemical Engineering Journal*, vol. 164, no. 1, pp. 246–254, 2010.

[7] Y. Shi, Y. Luo, N. Cai, J. Qian, S. Wang, W. Li, and H. Wang, "Experimental characterization and modeling of the electrochemical reduction of CO_2 in solid oxide electrolysis cells," *Electrochimica Acta*, vol. 88, no. 0, pp. 644–653, 2013.

[8] G. Narasimhaiah and V. M. Janardhanan, "Modeling CO_2 electrolysis in solid oxide electrolysis cell," *Journal of Solid State Electrochemistry*, vol. 17, no. 8, pp. 2361–2370, 2013.

[9] M. Ni, "2D thermal modeling of a solid oxide electrolyzer cell (SOEC) for syngas production by H_2O/CO_2 co-electrolysis," *International Journal of Hydrogen Energy*, vol. 37, no. 8, pp. 6389–6399, 2012.

[10] Y. Xie and X. Xue, "Modeling of solid oxide electrolysis cell for syngas generation with detailed surface chemistry," *Solid State Ionics*, vol. 224, no. 0, pp. 64–73, 2012.

[11] W. Li, Y. Shi, Y. Luo, and N. Cai, "Elementary reaction modeling of CO_2/H_2O co-electrolysis cell considering effects of cathode thickness," *Journal of Power Sources*, vol. 243, no. 0, pp. 118–130, 2013.

[12] M. Navasa, C. Graves, C. Chatzichristodoulou, T. L. Skafte, B. Sundén, and H. L. Frandsen, "A three dimensional multiphysics model of a solid oxide electrochemical cell for degradation studies." Manuscript in preparation, 2016.

[13] T. L. Skafte, C. Graves, P. Blennow, and J. Hjelm, "Carbon deposition and sulfur poisoning during CO_2 electrolysis in ni-based solid-oxide-cell electrodes." Submitted, 2016.

[14] H. Chang and G. Jaffé, "Polarization in electrolytic solutions. part i. theory," *The Journal of Chemical Physics*, vol. 20, no. 7, pp. 1071–1077, 1952.

[15] A. Leonide, S. Hansmann, A. Weber, and E. Ivers-Tiffée, "Performance simulation of current/voltage-characteristics for sofc single cell by means of detailed impedance analysis," *Journal of Power Sources*, vol. 196, no. 17, pp. 7343–7346, 2011.

[16] H. Wendt and G. Kreysa, *Electrochemical Engineering*. Berlin: Springer, 1999.

[17] A. Bertei and C. Nicolella, "Common inconsistencies in modeling gas transport in porous electrodes: The dusty-gas model and the Fick law," *Journal of Power Sources*, vol. 279, pp. 133–137, 2015.

[18] Y. S. Toulokian, R. K. Kirby, R. E. Taylor, and T. Y. R. Lee, *Thermal Expansion - Nonmetallic Solids. Thermophysical properties of Matter*, vol. 13. New York: IFI/Plenum, 1984.

[19] R. Morrell, *Handbook of Properties of Technical and Engineering Ceramics. Part 1. An Introduction for the Engineer and Designer*. London: Her Majesty's Stationery Office, 1985.

[20] C. C. Appel, N. Bonanos, A. Horsewell, and S. Linderoth, "Ageing behaviour of zirconia stabilised by yttria and manganese oxide," *Journal of Materials Science*, vol. 36, no. 18, pp. 4493–4501, 2001.

[21] W. Kong, H. Zhu, Z. Fei, and Z. Lin, "A modified dusty gas model in the form of a Fick's model for the prediction of multicomponent mass transport in a solid oxide fuel cell anode," *Journal of Power Sources*, vol. 206, no. 0, pp. 171–178, 2012.

[22] H. Geisler, A. , A. Weber, and E. Ivers-Tiffée, "Stationary FEM Model for Performance Evaluation of Planar Solid Oxide Fuel Cells Connected by Metal Interconnectors: I. Model Framework and Validation," *Journal of Electrochemical Society*, vol. 161, no. 6, pp. F778–F788, 2014.

[23] A. J. Samson, P. Hjalmarsson, M. Søgaard, J. Hjelm, and N. Bonanos, "Highly durable anode supported solid oxide fuel cell with an infiltrated cathode," *Journal of Power Sources*, vol. 216, pp. 124–130, 2012.